Patrick Mayrhofer, BSc

Photophysical Properties of Rubicene

MASTER THESIS

For obtaining the academic degree
Diplom-Ingenieur

Master Programme of
Technical Physics

Graz University of Technology

Supervisor:

Ao.Univ.-Prof. Dipl.-Ing. Dr. Günther Leising

Institute of Solid State Physics

Graz, March 2012

Abstract

Organic semiconductors offer promising properties for opto-electronic applications that are already commercially employed, for example in organic light emitting diodes (OLED) for small scale displays. However, yet an even more challenging task remains for research in organic semiconductors - the realization of the organic laser diode.

In order to further advance research on organic lasers developing new laser-active materials is important. Rubicene is a luminescent organic semiconductor that emits red light upon optical and electrical excitation. This thesis focuses on the investigation of Photophysical properties of Rubicene with the prospect of application as the optical active medium in an organic semiconductor laser.

Properties of the emission and absorption spectra of Rubicene in solution, thin film and as single crystals are studied, and the luminescence quantum yield of Rubicene in solution is determined by an indirect method. Additionally, the luminescence lifetime is measured in the phase domain for Rubicene in solution and as single crystals. Photoluminescence emission and absorbance spectra of Rubicene crystals under high pressure conditions are recorded in a diamond anvil cell up to 40kbar and a significant luminescence red-shift is observed.

Within this thesis, we attempt to build an optically pumped organic laser. A novel method is employed to transfer dielectric mirrors onto Rubicene single crystals in order to build a single crystal resonator. Upon cw-excitation of the plane-parallel microcavity resonance features are detected and are discussed within this thesis.

Kurzfassung

Organische Halbleiter weisen vielversprechende Eigenschaften für den Einsatz in opto-elektronischen Geräten auf. Beispielsweise werden organische Leuchtdioden (OLED) bereits kommerziell in kleineren Displays eingesetzt. Im Gegensatz dazu ist die Entwicklung einer organischen Laserdiode bisher nicht erfolgreich gewesen und bleibt somit Gegenstand intensiver Forschung.

Um die Entwicklung von Lasern basierend auf organischen Systemen weiter voran zu treiben ist die Forschung an neuen laser-aktiven Materialien wichtig. Rubicene ist ein organischer Halbleiter, der unter optischer und elektrischer Anregung Licht im rötlichen Spektralbereich emittiert. Gegenstand dieser Masterarbeit ist die Untersuchung der photo-physikalischen Eigenschaften von Rubicene in drei Zuständen: gelöst in Toluol, als dünner Film und in seiner einkristallinen Form.

Spektren der Emission und Absorption von Rubicene in allen drei Erscheinungsformen werden in der Arbeit näher untersucht, während die Quantenausbeute von Rubicene in gelöster Form bestimmt wird. Die Lebensdauer der Photolumineszenz von Rubicene in Lösung und als Einkristall wird im phase-domain gemessen. Zusätzlich zeigt sich eine rot-Verschiebung der Emission und der Absorption von Rubicene Kristallen unter Hochdruckbedingungen bis zu 40kbar, in einer Diamantdruckzelle.

Des Weiteren beschäftigt sich die Arbeit mit dem Bau eines Resonators für einen optisch gepumpten organischen Laser. Mittels einer neuen Methode werden dielektrische Spiegel auf Rubicene Kristalle aufgebracht um einen Einkristallresonator zu konstruieren. Unter kontinuierlicher optischer Anregung des plan-parallelen Resonators werden Resonanzerscheinungen beobachtet, die ausführlich diskutiert werden.

Acknowledgement

First and foremost, I am grateful for the invaluable advice and support my supervisor Prof. Dr. Günther Leising provided throughout the entire period this thesis was written. Additionally, I thank all members of the Institute of Solid State Physics at TU Graz for their kind support. In particular, I am thankful to:

- Prof. Dr. Roland Resel for providing the diamond anvil cell and supporting material
- Andreas Hirzer for previous measurements on Rubicene
- Hannes Brandner for the preparation of thin films
- Levent Tumbek for carrying out AFM measurements
- Reinhold Hetzel for our fruitful discussions
- Elisabeth Stern, Harald Kerschbaumer and Birgit Kunert for their support

I would like to thank Y.Y. Holovach; Institute of Analytical Technique, Uzhhorod National University, Ukraine for the fabrication of the DBR structures on Sodium Chloride.

Additionally, I would like to thank my beloved family and my friends for their continuous support, especially Evelyn Hartinger for proofreading and distraction.

Deutsche Fassung:
Beschluss der Curricula-Kommission für Bachelor-, Master- und Diplomstudien vom 10.11.2008
Genehmigung des Senates am 1.12.2008

EIDESSTATTLICHE ERKLÄRUNG

Ich erkläre an Eides statt, dass ich die vorliegende Arbeit selbstständig verfasst, andere als die angegebenen Quellen/Hilfsmittel nicht benutzt, und die den benutzten Quellen wörtlich und inhaltlich entnommene Stellen als solche kenntlich gemacht habe.

Graz, am …………………………… ………………………………………………..
(Unterschrift)

Englische Fassung:

STATUTORY DECLARATION

I declare that I have authored this thesis independently, that I have not used other than the declared sources / resources, and that I have explicitly marked all material which has been quoted either literally or by content from the used sources.

…………………………… ………………………………………………..
date (signature)

Contents

1 Introduction

1.1 Motivation

Organic semiconductors are subject to extensive research, as they offer promising properties for opto-electronic applications. Such properties are simpler and lower in costs of fabrication compared to inorganic semiconductors and potential applications in flexible devices. Organic light emitting diodes (OLED) based on small molecules are already commercially employed and used, in particular, in small scale displays for mobile phones or tabloid PCs, which achieve an impressive resolution by using the active matrix technology together with RGB color. Organic field effect transistors (OFET) also reached consumer applications, used for example together with OLEDs in displays. Polymer based organic solar cell development progresses and has reached efficiencies of 9% in 2011 [1] but at this point can not compete with inorganic solar cells except for niche applications, such as flexible solar cells on backbags. Another challenging task for research in organic semiconductors remains: the realization of the organic laser diode. Research on the electrical carrier injection is still in progress and although scientists have improved optically pumped organic lasers, electrical injection has not yet been achieved. Novel properties an organic laser may have, are an extremely compact structure, tunable accessible wavelengths throughout the visible spectrum and cheap fabrication processes.

Research on organic semiconductors with the prospect of building an organic semiconductor laser has been carried out for a long period of time from 1996 on, where the first optically-pumped organic laser has been observed. High quality reviews on this topic have been published that illustrate the large range of research topics within the field of organic laser physics [2, 3, 4, 5, 6, 7].

In order to further advance research on organic lasers developing new laser-active materials is important. This thesis investigates photophysical properties of the organic semiconductor Rubicene with prospect of applications as the optical active medium in an organic semiconductor laser.

Two different groups of organic materials are commonly distinguished, small molecules and conjugated polymers. Thin films of small molecules for optical active layers can be deposited by means of thermal evaporation while polymers are commonly processed from solution. One advantage of processing the materials from solution is that films can be realized by printing techniques, which is a cost efficient way to build devices. Organic semiconductors have wide emission and absorption bands and large separations between emission and absorption spectra are observed, as required for high gain to avoid self-absorption of the SE-transition. Additionally in polymers the wavelength ranges can be chosen by selecting the compounds of the polymers [8].

Already in 1996 Tessler et al. [9] demonstrated lasing output from a high-Q microcavity device based on the polymer Poly(p-phenylene vinylene) (PPV) and mentioned that the structure of their microcavity has potential for electrical pumping. [9]. Reduction of the threshold power (excitation intensity) is one research target being pursuit by means of finding new laser-active organic materials and by improving designs for laser resonators. Still remaining are two of the major concerns in research on the organic injection laser, the appearance of polarons and triplet states. Photons may be absorbed by polarons but more importantly exciton-polaron quenching reduces the excited state population. Upon electrical excitation Triplet states appear in a 3:1 ratio compared to Singlets. Triplet states absorb photons with similar wavelengths compared to the fluorescence emission.

Electron and Polaron issues are both directly related to the low mobility of organic semiconductors compared to their inorganic counterparts. A common material employed in inorganic laser diodes is GaAs with a mobility of $\mu = 10^4\,\mathrm{cm^2V^{-1}s^{-1}}$ [10]. Mobilities in amorphous organic semiconductor μ=(10^{-5}-10^{-2})$\mathrm{cm^2V^{-1}s^{-1}}$ are much lower [7]. The electron mobilities in oligomer single crystals is higher due to an increased ordering of the molecules as for example in Tetracene a value of $\mu = (0.5\text{-}0.8)\,\mathrm{cm^2V^{-1}s^{-1}}$ is observed [11].

Predictions about the development of organic semiconductor laser diodes are hard to achieve. A few years ago the general believe was, that current densities of $1\,\mathrm{kA\,cm^{-2}}$, which are needed to drive an inorganic injection lasers, exceed the limit reachable with organic semiconductors. However, already in 1999 Tessler demonstrated current densities close to $600\,\mathrm{A\,cm^{-2}}$ for PPV based LEDs driven by short pulse excitations, thus showing that conjugated polymers can survive those high current densities [2]. However, sufficiently high current densities are possible only in pure and high-quality organic films or in single-crystals. This was also a motivation for us to use small molecule single crystals for lasing experiments.

Since the organic laser diode seems to be a long-term goal, research also focuses on the development of indirect electrical pumping. Highly integrated lasers may be realized that can be operated in the entire range of visible wavelengths by using an inorganic laser diode on top of an organic laser. Sakata et al. used an InGaN laser diode to pump a film doped with a polymeric die within a microcavity. Under pulsed excitation they observed lasing with a minimum threshold value of 16 mW/pulse [12].

1.2 Outline

In Chapter 2 of this thesis fundamentals of photophysical properties in organic semiconductors and measurements of this properties are discussed. Resonance in the plane parallel resonator is described in Section 2.7 and the transmission of such a cavity is illustrated in Section 2.8 with prospects of further application with Rubicene single-crystals. Additionally fundamentals of lasing with organic semiconductors are described in this chapter, where in Section 2.9 we give an overview of currently employed cavity designs and describe their working principles.

Chapter 3 offers a description of the organic semiconductor Rubicene. Particularly, structural properties of Rubicene in solid form, ie. powder, thin film or single-crystal are presented.

Subsequently Chapter 4 focuses on experimental investigations of photophysical properties of Rubicene. Results of emission and absorption of Rubicene in solid from and in solutions are shown in Section 4.1 . Luminescence lifetime measurements in the phase domain are conducted with the solution and we modified the setup to measure the luminescence decay of single-crystals, depicted in Section 4.2. The quantum yield of Rubicene in solution was determined by means of an indirect measurement method compared to two fluorescence standards, as shown in Section 4.3. Additional insights into the electronic structure of Rubicene single-crystals are gained in Section 4.4, where application of high-pressure on the crystals in a diamond anvil cell yielded a large red-shift of absorption and emission.

A new method was employed to transfer dielectric layers onto Rubicene single crystals in order to build a single crystal resonator, shown in Section 5. The plane-parallel microcavity was pumped by means of an cw-diode laser and resonance features were observed.

2 Fundamentals

2.1 Energy Transitions in Organic Semiconductors

In order to understand the transitions between electronic states in organic semiconductors we first distinguish between systems of individual molecules, e.g. organic semiconducting molecules in solution, and solid state systems, i.e. single crystals or thin films. In systems of individual molecules natural electronic states exist, molecular orbitals, each with vibrational sublevels. The energetic distance between the highest occupied molecular orbital (HOMO) and lowest unoccupied molecular orbital (LUMO) is determined by the overlap of the π orbitals. In conjugated systems, p_z orbitals of carbon atoms overlap and form π- bonds. The resulting delocalization of π electrons is an important parameter, determining the location of electronic levels. Increasing the conjugation length, i.e. more pi- orbitals are overlapping, yields a higher delocalization of the electrons and in turn the energy distance between HOMO and LUMO, the bandgap decreases. In some conjugated oligomers like sexiphenyl, theoretical calculations done by Zojer et al show that a "quasi-bandstructure evolves, which is characterized by discrete electronic states in momentum space aligned along the bands of the parent polymer" [13]. Figure 2.1 illustrates the bandgap-decrease, corresponding to an emission-wavelength increase of oligomers with increasing length of oligothiophene molecules (α-NT). We note a clear redshift of the emission with increasing conjugation length, ie. going from α-Terthiophene (α-3T) to α-Octithiophene (α-8T) by attaching an additional thiophene ring in each step.

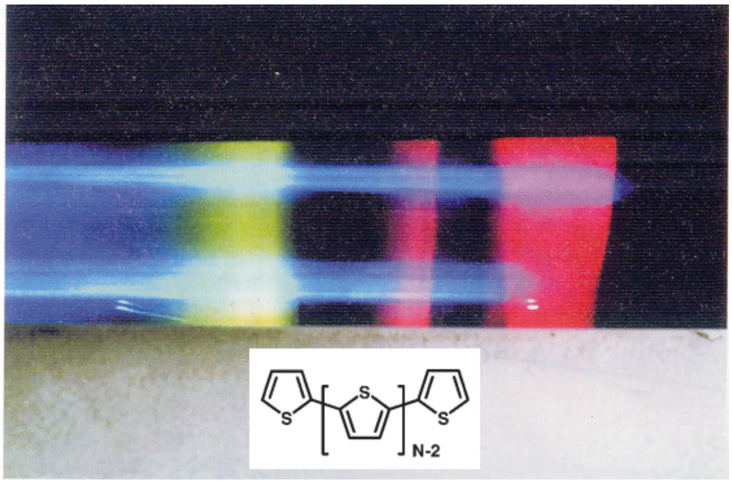

Figure 2.1: Fluorescence emission of α-NT microcystals, obtained from Vacuum Sublimation of α-8T oligomer powder mixture and excited by UV radiation. Red: α-8T, Orange: α-6T, yellow: α-4T, blue: α-3T [14]. The inset on the bottom shows the structure of α-NT [15].

Examples for the behavior of the energy difference between HOMO and LUMO are acenes. Starting from benzene the conjugation length L increases up to pentacene, resulting in a decrease of the bandgap approximately proportional to 1/L, as is illustrated in Figure 2.2.

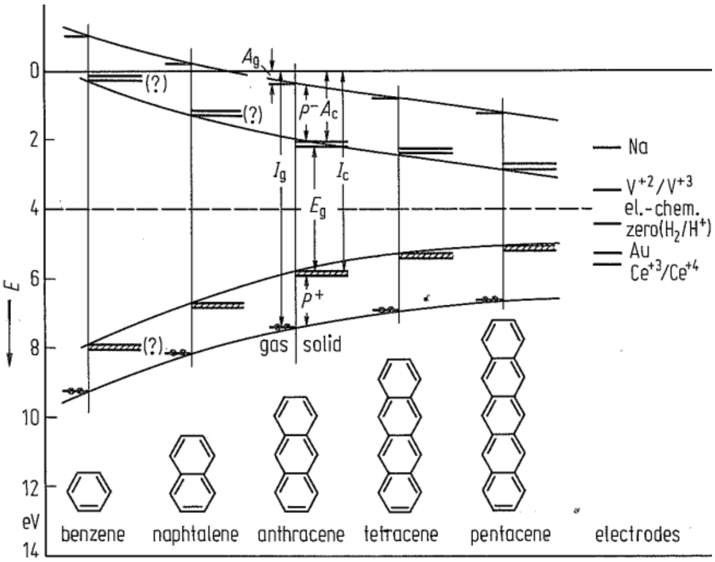

Figure 2.2: Energy of the HOMO and LUMO for acenes, to illustrate the decreasing bandgap E_g from benzene to pentacene. [16]

It is worthwhile to note the analogy of intrinsic monodisperse organic molecules to monodisperse nanocrystals. Norris et al. report on size-dependent absorption and emission of CdSe nanocrystals [17]. Increasing the size of these quantum dots from 20 Å to 80 Å shifts the emission from blue towards red, thus the bandgap decreases. Hence, for small systems the number of single-atoms is important for the electronic properties and as the system size increases the electronic structure of the bulk is reached. Figure 2.3 shows the luminescence-emission of CdSe-nanocrystal suspension, demonstrating the size-effect on the bandgap, ie. enlargement of the quantum dots is accompanied by a decrease of E_g.

A material can be described as containing a high quantity of clusters, consisting of the same number of molecules with identical structures. The number n of atoms per cluster is important for the resulting electronic structure. Increasing n leads to a longer characteristic length, i.e. a larger size, and the bandgap decreases until it converges to the electronic structure of the bulk. In solid state materials the electrons occupy bands, rather than separated electronic levels.

While the intramolecular bonds are strong covalent bonds, the intermolecular forces are weak Van der Waals bonds. In organic crystals up to now, only a small overlap between π-orbitals of individual molecules in the crystal was found, thus charge transport is based on carrier jumps across energy barriers, separating the molecules. In order to increase the π-overlap, distances between adjacent molecules must be roughly the same length range as C-C bonds, 1.2Å-1.5Å. For example in Rubicene single crystals the distance is small (3Å), but still not sufficiently small [19]. Increase of the packing density, e.g. by applying high pressure increases the intermolecular electronic delocalization. In an organic solid, the apparent periodicity changes dependent on the direction of observation of the π-electron system. Therefore pronounced

Figure 2.3: Fluorescence emission of CdSe-nanocrystal solutions, with increasing crystallite size from 20 Åto 80 Å[18].

anisotropy of the electronic structure and of the transition properties is observed. Considering electronic transitions in organic semiconductors we focus on excitations by electro-magnetic radiation in the optical region and the resulting processes. After excitation, an electron is promoted to the excited state and a hole is left behind in in the groundstate. However, electron and hole attract each other, thus they relax to a bond excitonic state. In contrast to inorganic semiconductor with weak excitonic binding energies (eg. Si: EBE=15 meV [20]), excitons in organic semiconductors exhibit higher binding energies (eg. Anthracene: EBE$\approx$1eV [21]). The EBE further depends on the degree of electronic delocalization. For example, Puschnig et al. conducted theoretical calculations and cite experimental values from acenes [22, 23], that show a reduction of the EBE with increasing conjugation length from benzene (EBE$= 1.0 - 1.5$ eV) to pentacene (EBE$= 0.0 - 0.5$ eV) [21]. Processes of absorption and radiative or non-radiative decay of excited excitonic states are visualized in the Jablonski diagram.

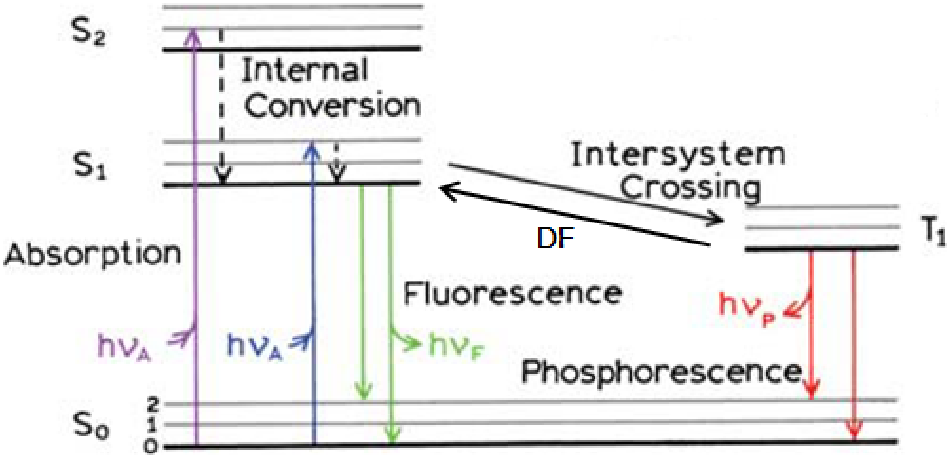

Figure 2.4: Jablonski Diagramm [24].

Figure 2.4 is a simple form of the Jablonski diagram. An incident photon is absorbed on a timescale of 10^{-15} s and excites the fluorophore from the singlet groundstate S_0 to some higher vibrational excited singlet state S_1 or S_2. Relaxation occurs non radiatively to the vibrational groundstate of S_1 and is called internal conversion (IC). Fluorescence is the emissive relaxation of S_1 to the ground state. Another possibility is a transition to a triplet state (T_1) by spin conversion called Intersystem Crossing (ISC). Direct emissive transition from Singlet to Triplet state is dipole-forbidden and the radiative transition $T_1 \rightarrow S_0$, called the phosphorescence case, has therefore a much longer lifetime than in fluorescence. Light emission in phosphorescence can occur on timescales larger than μs while fluorescence decays within ns. Another transition $T_1 + T_1 \rightarrow S_0 + S_1$ results in delayed fluorescence DF, occurring on a timescale in between fluorescence and phosphorescence and with spectral characteristics identical to fluorescence. The Jablonski diagram shown in Figure 2.4 is a simplified version since a display of more complicated processes would exceed the scope of this introduction. Other transitions are, for example, singlet quenching, energy transfer or solvent interaction.

2.2 Laser

A LASER (Light Amplification by Stimulated Emission of Radiation) is an optical device emitting coherent light. The light is spatially coherent and phase coherent as well. There are several types of lasers, gas-discharge, dye, solid state, electron beam and x-ray beam lasers [25]. By far the highest number of lasers produced today are diode-lasers, made of semiconductors, because of their small size and high efficiency (application amongst others: DVD-, CD-, blue ray- drives or LED lighting).

Three basic processes are important to describe interaction between light and matter, i.e. absorption, spontaneous emission and stimulated emission (SE). In absorption a photon with energy $E = h\nu_{12}$ promotes an electron from some state E_1 into a higher excited state E_2, the energy difference $E_2 - E_1$ matching the photon energy. In reality the photon energy may be larger than E_{12} and the additional energy dissipates as heat - molecule vibrations or phonons. In emission a photon is emitted when an electron falls back into an energetically lower state which takes place either spontaneously or stimulated by another photon. In spontaneous emission the exact moment when the state relaxes can not be predicted. Therefore the emitted photons exhibit random phases relative to each other in contrast to stimulated emission, where a photon meets the excited electron, which, in turn, falls down into the lower state and another photon is emitted, exactly matching the phase of the first photon. In this case light gets amplified, one basic requirement for lasing.

A crucial condition for SE is population inversion, that is to overcome the thermodynamic equilibrium populations of excited states and elevate a sufficiently high number of electrons into the upper laser transition state to exceed the population of the lower laser transition state [3]. This can only take place if the emitted photon is not re-absorbed in the material, which is the case if it has lower energy than the minimum absorption energy. Therefore, at least three levels are required- a ground state, one excited state with a low lifetime and a lower excited state with a long lifetime to make population inversion possible. An additional lower level with a short lifetime increases the efficiency of the laser system because inversion can be achieved more easily. In real lasers active media are often much more complex and have a multiplicity of levels taking part in the SE process. Due to the stokes-shift of their emission, organic luminescent materials are natural four-niveau systems making them ideal candidates for laser materials.

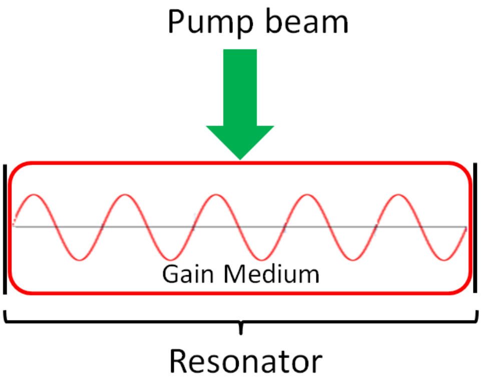

Figure 2.5: Schematic View of the principle design of a Laser.

The principle design of a laser device is shown in Figure 2.5. The gain medium is excited by a pump beam, or by charge carrier injection, resulting in population inversion. First light is emitted by means of spontaneous emission and due to feedback within the resonator the light passes the gain medium several times, resulting in the emission of coherent light by means of SE. Under the condition of sufficiently high excitation intensity SE emission becomes the dominate process and gain narrowing starts, ie. spectral narrowing of the emission. The excitation intensity increases and a laser beam is emitted out of the resonator. The linewidh narrowing is accompanied by a dramatic increase of the coherence length of the emitted EM-wave, thus making the laser ideal for spectroscopic applications, as described in Section 2.4.

2.3 Absorption

The absorption coefficient α is used to describe the absorption of radiation in matter. We assume a change of the light intensity I after travelling a distance x through a material is proportional to the initial Intensity I: $\frac{dI}{dx} \propto -\alpha * I$. Solving the differential equation with an initial intensity I_0 yields:

$$I = I_0 \cdot exp(-\alpha x) \tag{2.1}$$

Another measure for the absorption is the absorptivity A or optical density OD. It gives a convenient measure for a particular specimen since it can be directly calculated from the Transmission T via

$$A = log(\frac{I_0}{I}) = -log(T) \tag{2.2}$$

2.4 Transition Lineshape

The emission from a radiative transition of a fluorophore is not strictly monochromatic but exhibits spectral broadening. The spectral width of emitted light is fundamentally limited, i.e.

it can not be infinitely narrow. We consider the impossible case of an infinitely extended wave, infinitely in space and time. Supposing a simple wave oscillating at the circular frequency ω_0, described by:

$$x(t) = e^{-i\omega_0 t}$$

A fourier transformation is used to describe this wave in the frequency space:

$$x(\omega) = \frac{1}{\sqrt{2\pi}} \int_{-\infty}^{\infty} x(t)\, e^{i\omega t}\, dt = \sqrt{2\pi}\, \delta(\omega - \omega_0)$$

A simple single frequency ω_0 is sufficient to describe this wave, hence, the ”linewidth” is a δ-function.

Light, emitted from real light sources is coherent only for a certain length, defined by the coherence length, ie. the unperturbed length of a wave without a phase jump. In order to consider a finite coherence length we limit the integration time $-\frac{\tau_0}{2} < t < \frac{\tau_0}{2}$. Performing the integration yields:

$$x(\omega) = \sqrt{\frac{2}{\pi}} \frac{sin[(\omega - \omega_0)\tau/2]}{\omega - \omega_0}$$

Therefore a spectrum of frequencies is needed to describe the wave instead of just a single frequency, as for an infinite coherence length. The contribution to the emission from each frequency is given by the power spectrum, ie. $|x(\omega)|^2$:

$$|x(\omega)|^2 = \frac{2}{\pi} \frac{sin^2[(\omega - \omega_0)\tau/2]}{(\omega - \omega_0)^2} \tag{2.3}$$

The power spectrum is shown in Figure 2.6. Most important are contributions between $\omega_0 - \frac{\pi}{\tau_0}$ and $\omega_0 + \frac{\pi}{\tau_0}$ yielding a spectral width of $\Delta\omega = \frac{2\pi}{\tau_0}$. The coherence length l_c is therefore [26]:

$$l_c = \tau_0\, c = \frac{2\pi}{\Delta\omega_0}\, c$$

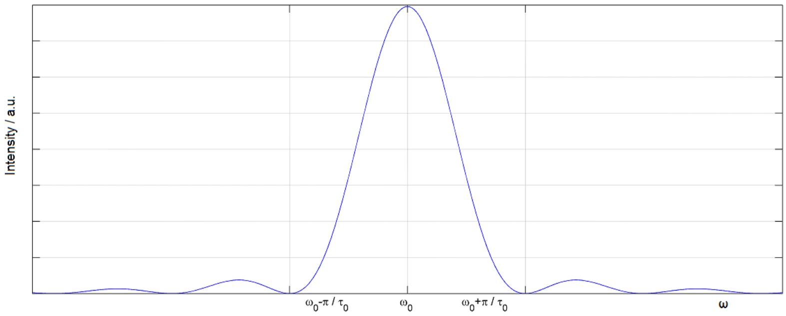

Figure 2.6: Power spectrum of spatially limited wave according to Equation 2.3

Light emitted from white light sources exhibit very short coherence lengths of just a few wavelengths and broad spectral distributions. However, lasers can display much longer coherence lengths because of the way light is emitted, ie. by simulated emission. Gas discharge lasers can exhibit coherence lengths of about 50 km, making their emission very narrow and thus ideal for spectroscopic applications. Table 2.1 give values for coherences properties of some representative lightsources.

Table 2.1: "Longitudinal coherence properties of light from some representative sources."[26]. Wavelength λ, frequency ν, frequency range $\Delta\nu$, coherence time τ_c, coherence length l_c

source	λ /nm	ν /10^4 Hz	$\Delta\nu$	τ_c/s	l_c
white light	400-600	5-7.5	2.5 * 10^4 Hz	4 x 10^{-15}	1.2 μm
Hg lamp with single isotope	546.1	5.49	300 MHz	3 x 10^{-9}	1 m
orinary He-Ne Laser	632.8	4.74	1 GHz	10^{-9}	0.3 m
elaborator stabilized He-Ne laser	632.8	4.74	10 GHz	10^{-4}	30 km

The wings of the power spectrum in Figure 2.6 are disturbing for spectroscopic applications; For example, in fourier-transform infrared spectroscopy (FT-IR) the finite pathlength of the mirror in a Michelson Interferometer has the same effect on the frequency spectrum as the coherence length. In order to remove the tails, the measured spectrum is multiplied by an Apodization function, ie. a rectangular, triangular or another function which goes to zero when the pathlenght-limit is reached. This function is multiplied with the recorded spectrum I(x), prior to fourier transforming the signal into frequency space to get I(ν).

The shape of an emissive transition is further broadened by means of two processes. A Gaussian shape appears due to thermal motion of particles, ie. Doppler broadening. A Lorentzian gets superimposed because of collisions of emitting atoms with their neighboring particles [27]. The resulting lineshape is a convolution of a Lorentzian and a Gaussian. However, for simplicity we used a sum of Gaussian distributions as depicted below to fit the fluorescence.

$$g(\lambda) = \frac{A}{2\pi\sigma^2} \cdot e^{\frac{(\lambda-\lambda_0)^2}{2\sigma^2}} \tag{2.4}$$

A depicts a scaling factor, λ_0 is the peak position and σ is a measure for the peak- width. The full width at half maximum (FWHM) is FWHM= $2\sqrt{2ln(2)}\sigma$

2.5 Fluorescence Lifetime

Fluorescence lifetime is an important intrinsic parameter of light emitting systems. Light emission with short lifetime is called fluorescence while longer lifetimes occur in phosphorescence, as mentioned in Section 2.1.

2.5.1 Meaning

The meaning of the fluorescence lifetime is explained in this section following the book by Lakowicz [24]. An excitation with a δ- function pulse of light and subsequent decay of the excited state population n(t) can be described mathematically by the following rate equation; where Γ and k_{nr} are the assumed radiative and non- radiative decay rates.

$$\frac{dn}{dt} = -(\Gamma + k_{nr})n(t) \tag{2.5}$$

Solution by separation of variables yields with the initial population after excitation $n(t = 0) = n_0$

$$n(t) = n_0 \cdot \exp(-\frac{t}{\tau}) \tag{2.6}$$

Intensity of light emission is proportional to the excited state population. The intensity decay can thus be written with I(t=0)=I_0

$$I(t) = I_0 \cdot \exp(-\frac{t}{\tau})$$

Next, the average time a fluorophore spends in the excited state is being calculated by:

$$< t >= \frac{\int_0^\infty t \cdot n(t)dt}{\int_0^\infty n(t)dt} \tag{2.7}$$

For n(t) we can use eq. 2.6. Straight forward integration of the denominator yields $n_0\tau$ while the numerator results in $n_0\tau^2$. Overall yielding:

$$< t >= \tau$$

Hence, the average time a fluorophore spends in the excited state is corresponding to the lifetime τ. However, molecules also show multi- or non-exponential decays. In this cases $< t >$ can become a complicated function of the decay parameters. Considering a bi-exponential decay, described by two fractions α_1, α_2 and two different decay times τ_1, τ_2:

$$I(t) = I_0 \cdot (\alpha_1 \ \exp(-\frac{t}{\tau_1}) + \alpha_2 \ \exp(-\frac{t}{\tau_2}))$$

Using this relation in Equation 2.7 yields:

$$< t >= \frac{\alpha_1\tau_1^2 + \alpha_2\tau_2^2}{\alpha_1\tau_1 + \alpha_2\tau_2}$$

Therefore, in the bi-exponential case the average excitation time becomes a weighted average of the two decay constants.

2.5.2 Measuring Lifetimes

Two common methods are used to measure the fluorescence lifetime of a fluorophore, i.e. measurements in time and frequency domain. In the time domain the sample is excited with a very narrow pulse of light, e.g. from a fs-pulsed laser and a fast detector records the emission as indicated in Figure 2.7. Frequency domain measurements make use of amplitude- modulated excitation with a modulation period in the same order of magnitude as the luminescence lifetime. Two parameters, the phaseshift (ϕ) and the change of the emission amplitude (modulation m) are measured, and their variation with respect to different modulation frequencies is used to calculate the lifetime, described in section 2.5.4. In Figure 2.7 to the right the definitions of both quantities are given. Only a fraction of the excitation is modulated which is the reason for the presence of a cw-amplitude in the definition of the modulation m.

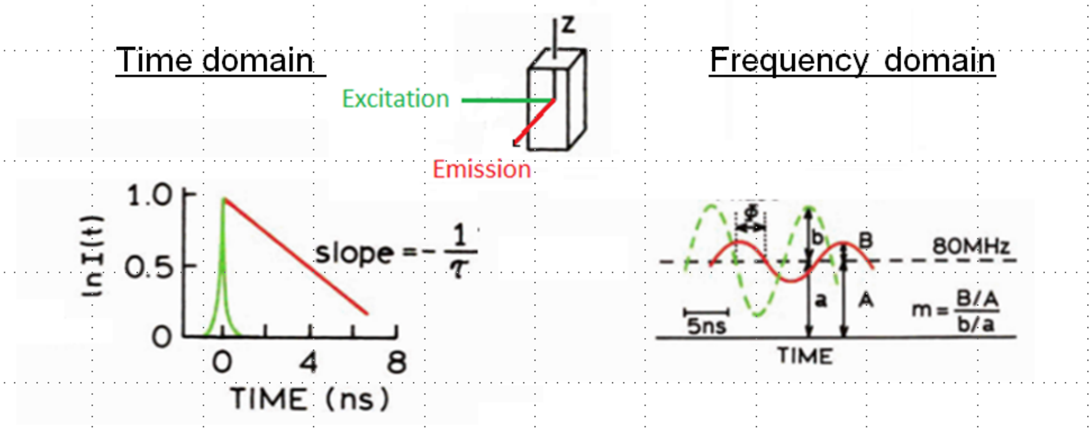

Figure 2.7: Principle of time and frequency- domain lifetime measurements, green indicates the excitation beam, while red is the sample's emission.[24]

2.5.3 Cross Correlation Detection

The fluorescence of many organic semiconductors decays on a ns-timescale thus making high frequencies (hf) of 100 MHz and more for the modulation of the excitation beam necessary. The detection of phase ϕ and modulation m of hf-signals is done by shifting them to a signal, orders of magnitude lower in frequency. This method is called Cross Correlation Detection and the following formulas are based on Dicker's diploma thesis [28].

The excitation consists of a modulated part and a cw- fraction due to limitations of the electro-optic light modulation. The sample's emission $f(t)$ is therefore an oscillation with amplitude β on top of a cw-part α:

$$f(t) = \alpha + \beta sin((\omega_0 + \Delta\omega_0)t)$$

Periodical modulation of the excitation takes place with circular frequency ω_0 while $\Delta\omega_0$ is the cross correlation frequency. The output signal of the detector (photomultiplier-tube PMT) is also modulated on top of a DC part with frequency ω_0.

$$ref_0(t) = A + Bsin(\omega_0 t + \phi)$$

By varying the high voltage of the PMTs in this manner, the emission is multiplied by $ref_0(t)$. The signal passes a cut-off filter with cut-off frequency ω_c and $0 < \Delta\omega_0 < \omega_c << \omega_0$ yielding:

$$g(t) = A\alpha + \frac{1}{2}B\beta cos(\Delta\omega_0 t - \phi)$$

The final output signal g(t) oscillates with the cross correlation frequency $\Delta\omega_0$; 80 Hz in our setup. By using this technique information about amplitudes and about the phaseshift is preserved.

2.5.4 Fit Formulae

A mathematical description of the fluorescence during excitation with modulated light is necessary to obtain a connection between phase/ modulation and lifetime. The following procedure and formulae to obtain model functions are taken from [28]. We assume an excited state (n) decay with a rate constant k, which can be a sum of a non-radiative and a radiative decay:

$$\frac{dn}{dt} = -kn$$

In our measurement also the excitation $ref(t) = a + be^{-i\omega_0 t}$ is present:

$$\frac{dn}{dt} = -kn + a + be^{-i\omega_0 t} \tag{2.8}$$

Solving this differential equation yields for the phase ϕ and modulation m:

$$m = A \cdot \frac{1}{\sqrt{1 + \omega_0^2 \tau^2}} \tag{2.9}$$

$$\phi = arctan(-\omega_0 t) \tag{2.10}$$

By measuring m and ϕ with respect to modulation frequency ω_0, the data is fitted according to these formulae. Lifetime τ as well as a scaling factor A, correcting the modulation m, are used as fit parameters in a least square fit algorithm implemented in MATLAB. In the analytical solution to Equation 2.8 A is equal to one.

If the accuracy of the fit, using Equation 2.9 and Equation 2.10, is insufficient to describe a particular measurement result a double- or multi-exponential decay can be used. For example, in a double exponential (bi-exponential) decay two different lifetimes appear. A derivation of phase and modulation for the multi- exponential decay can be found elsewhere [28], yielding (e.g. with n=2 for the double exponential decay):

$$m = A \cdot \sqrt{[\sum_{i=1}^{n} f_i \, (1 + \frac{\omega_0^2}{k_i^2})^{-\frac{1}{2}} \, cos(\phi_i)]^2 + [\sum_{i=1}^{n} f_i \, (1 + \frac{\omega_0^2}{k_i^2})^{-\frac{1}{2}} \, sin(\phi_i)]^2} \tag{2.11}$$

$$\phi = arctan \frac{\sum_{i=1}^{n} f_i \, (1 + \frac{\omega_0^2}{k_i^2})^{-\frac{1}{2}} \, sin(\phi_i)}{\sum_{i=1}^{n} f_i \, (1 + \frac{\omega_0^2}{k_i^2})^{-\frac{1}{2}} \, cos(\phi_i)} \tag{2.12}$$

where:

$$\phi_i = arctan(-\omega_0 \, \tau_i)$$

The fractions f_i of the corresponding lifetime τ_i appearing in phase and modulation are normed to $\sum_{i=1}^{n} f_i = 1$.

Fit-parameters are the fractions f_i and τ_i as well as a prefactor A for the modulation m. The setup for phase-sensitive detection produces accurate values for ϕ. However, the modulation m can be stretched by some factor A, ie. in the low frequency limit: $m = 1$ is not true. To measure m (and ϕ) a reference-scattering solution is necessary that defines a zero-point for the phase. In order to get m-values between one and zero a measured value of m is divided by m of the reference. Therefore differences in homogeneity and differences of spatial dimensions between sample and reference are reasons for a measured modulation different than 1 in the low frequency limit and for the prefactor A.

2.6 Quantum Yield

The fluorescence quantum yield (ϕ_f) is a measure for the efficiency of light emission from a luminophore. Demas and Crosby [29] give a definition: ”The luminescence quantum yield of a compound is defined as the fraction of molecules that emit a photon after direct excitation by the source.” This is not the same as the number of photons absorbed by the sample divided by the number of photons that escape the sample, but nearly equal to this value and for our purpose a sufficiently accurate definition.

The procedure for measuring the quantum yield of a sample $\phi_{f,S}$ is described in detail in a review by Wuerth et al [30] using the formula by Demas and Crosby [29]:

$$\phi_{f,S} = \phi_{f,Ref} \frac{F_S(\lambda_{Ex})}{F_{Ref}(\lambda_{Ex})} \frac{f_{Ref}}{f_S} \frac{n_S^2}{n_{Ref}^2} \frac{q_{Ref}(\lambda_{Ex})}{q_S(\lambda_{Ex})} \tag{2.13}$$

In Equation 2.13, $\phi_{f,Ref}$ is the quantum yield of a reference-standard solution. F is the integrated spectral fluorescence photon flux, calculated from blank-corrected emission intensity $I(\lambda_{Em})$, as well as corrected for photon-energy and detector responsitivity (s(λ_{Em})), ie. multiplied by $(\frac{hc_0}{\lambda_{Em}})^{-1}\frac{1}{s(\lambda_{Em})}$ prior to the integration in order to convert from an appropriate energy-scale to a photon-scale:

$$F = (hc_0)^{-1} \int \frac{I(\lambda_{Em})}{s(\lambda_{Em})} \lambda_{Em} d\lambda_{Em}$$

The integration is performed over the emission range of the fluorophore and f(λ_{Ex}) denotes the absorption factor, ie. the fraction of absorbed light. f(λ_{Ex}) is approximately the absorbance, however, we used the more exact calculation from Wuerth et al [30], that follows from the definition of the absorptivity in Section 2.3:

$$f(\lambda_{Ex}) = 1 - 10^{-A(\lambda_{Ex})} \tag{2.14}$$

In case of different excitation- wavelengths, used for sample and reference, q_{Ref} and q_S denote the excitation-photon flux integrated over the illuminated area. The increased pathlength of light in the sample-solution due to a higher refractive index (n_S / n_{Ref}) of one solvent compared to another is taken into account by the fractions of n^2.

To enhance the accuracy of the measurements, various concentrations were measured and ϕ_f was calculated, using the slopes (grad(S)/grad(Ref)) of the integrated emission intensity with respect to $f(\lambda_{Ex})$, thus deviating from the description by Wuerth et al.:

$$\phi_{f,S} = \phi_{f,Ref} \frac{grad(S)}{grad(Ref)} \frac{n_S^2}{n_{Ref}^2} \frac{q_{Ref}(\lambda_{Ex})}{q_S(\lambda_{Ex})} \tag{2.15}$$

with

$$grad(x) = \frac{dF_x(\lambda_{Ex})}{df_x(\lambda_{Ex})}$$

2.7 Optical Cavity

A crucial element of a laser is the optical feedback structure since it gives rise to high light intensities for restricted wavelengths of the EM-field (or photon energies) only. Once a sufficiently high excitation density is reached SE emission starts to dominate over spontaneous emission, outlined in Section 2.2. In the conventional approach the laser-active medium is placed in between two mirrors, which form an optical resonator.

Determination of the electric field in a resonator allows us to design it individually for the emission properties of a specific laser-active medium. We start by considering a closed cuboidal resonator, following Hooker and Webb [31], with the assumption of no charge within the cavity. The electric field vector $\boldsymbol{E}$ will obey the wave equation with the speed of light c:

$$\Delta \boldsymbol{E}(\boldsymbol{r},t) = \frac{1}{c^2}\frac{\partial^2 \boldsymbol{E}(\boldsymbol{r},t)}{\partial t^2} \tag{2.16}$$

Assuming the field is harmonic with angular frequency ω yields the Helmholtz equation for the spatial variation of the electric field $\mathbf{E(r)}$:

$$\Delta \boldsymbol{E(r)} = -\frac{\omega^2}{c^2}\boldsymbol{E(r)}$$

This equation can be solved by a Product Ansatz, individually done for each component of the electric field vector in dependence of functions of the three spatial coordinates. During the solution the constants k_i (i=x,y,z) are introduced, that obey the dispersion relation:

$$k_x^2 + k_y^2 + k_z^2 = \frac{\omega^2}{c^2}$$

We assume that the cavity is a completely closed cuboid with side lengths L_x, L_y, L_z as depicted in Figure 2.8. Application of the boundary conditions for the tangential field component and normal field component yields a restriction of the allowed frequencies ω_{lmp}:

$$k_x^2 + k_y^2 + k_z^2 = (\frac{\pi}{L_x}lx)^2 + (\frac{\pi}{L_x}my)^2 + (\frac{\pi}{L_z}pz)^2 = \frac{\omega_{lmp}^2}{c^2} \tag{2.17}$$

The set of **integers** (l,m,p) defines a mode in the cavity that restricts the allowed wavelengths $\lambda_{lmp} = \frac{2\pi c}{\omega_{lmp}}$ within the cavity as well. The solution to Equation 2.16 can be written as a sum of plane and travelling waves: $\alpha e^{i(\boldsymbol{rk}-\omega t)}$ and the wavevector $\boldsymbol{k}$ is defined by Eigenvectors of the E field $\boldsymbol{i},\boldsymbol{j},\boldsymbol{k}$: $\boldsymbol{k} = \pm k_x\boldsymbol{i} \pm k_y\boldsymbol{j} \pm k_z\boldsymbol{k}$.

Now we consider an open cavity by removing all walls except those at z=0 and z= L_z hence, we form a plane parallel resonator. A part of the radiation can escape the cavity now, but some low-loss modes still remain in case of a small mirror distance compared to width and height of the resonator, thus $k_x, k_y << k_z$. The mode-frequency depends then to zero order just on one of the integers, p, and the dispersion relation: Equation 2.17, reduces to:

$$\omega_{lmp} = \frac{2\pi c}{2L_z}p$$

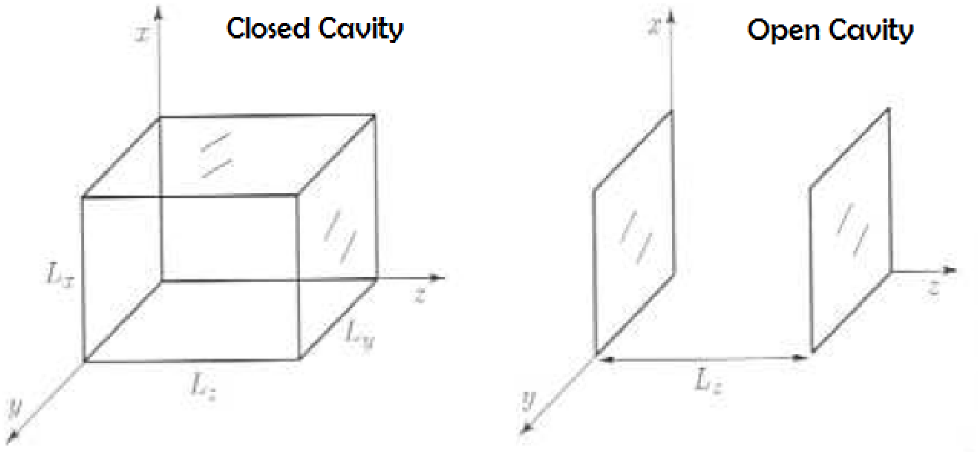

Figure 2.8: Schematic Views of a closed cavity and an open cavity design [31].

Equivalent to:

$$L_z = \frac{\lambda_{lmp}}{2} p$$

Therefore, allowed are only waves that fit into the cavity, ie. an integer times half of their wavelengths correspond to the cavity length. However, due to the finite mirror areas diffraction losses will always appear. They can be reduced by confining the modes close to the axis, eg. by using spherical mirrors instead of plane ones.

2.8 Airy Formula

The standing-wave condition for an EM-wave within a plane-parallel resonator, was described in Section 2.7. In order to evaluate the quality of a plane-parallel resonator for laser applications, the transmission is calculated following Brooker [26], except for the representation of transmission in Figure 2.10 and the evaluation of the Quality factor.

In Figure 2.9 a beam of light is incident on a Fabry Perot resonator, ie. a plane parallel resonator. The mirrors are partially reflective with coefficients r_1 and r_2 at the outer surface and at the inner surfaces of the mirrors respectively. The wave incident on the first mirror has an amplitude of U_0, and a fraction of t_1U_0 of this beam is transmitted while r_1U_0 is reflected. At the second mirror a fraction $r_2(r_1U_0)$ is reflected while $t_2(r_2U_0)$ is transmitted through the resonator. The phase difference, due to the extended path-length after each round trip is $\delta = k2dcos(\theta)$.

In case of phase shifts occurring at the mirror surfaces, complex r_1,t_1,r_2,t_2 are possible. Therefore, the reflexion coefficient (R $= |r_2|^2$ and $r_2^2 = Re^{-i\alpha}$) is introduced and the phase difference between two adjacent beams becomes: δ=k 2d cos(θ)-α. The transmitted part U_T of the incident amplitude U_0 is the sum of the amplitudes of all transmitted rays:

$$U_T = U_0 t_1 t_2 \sum_{n=0}^{\infty} (Re^{-i\delta})^n$$

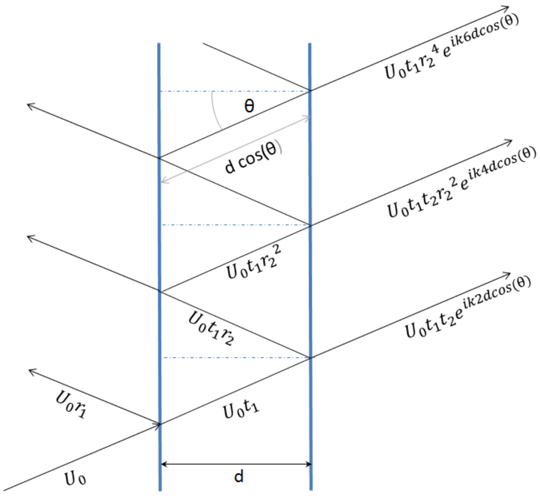

Figure 2.9: Illustration of the path of a light ray going through a Fabry Perot resonator consisting of two plane-parallel plates. Upon reflexion the amplitude (U_0) is partly reflected on the outer surface (U_0r_1) and partly transmitted (U_0t_1). Within the plates the amplitude decrease by a factor of r_2 each time the ray is reflected and two adjacent transmitted rays exhibit a path difference of $\delta = 2dcos(\theta)$

This is a geometric series and yields:

$$U_T = \frac{U_0t_1t_2}{1 - Re^{-i\delta}}$$

Intensities are the square of absolute values of amplitudes, therefore the overall transmitted fraction of intensity T, by using Euler's theorem is [26]:

$$T = \frac{|U_T|^2}{|U_0|^2} = \left(\frac{|t_1t_2|}{1-R}\right)^2 \frac{1}{1 + \frac{4R}{(1-R)^2} sin^2(\delta/2)} \tag{2.18}$$

In order to obtain the simple form of the Airy formula we assume no phase shift at the mirrors and neglect the Prefactor. Additionally we introduce the Finesse, a quantity used to specify the quality of the resonance peaks and also we rewrite k in terms of wavelength by using the dispersion relation ($k^2 = \frac{\omega^2}{c^2}$):

$$T = \frac{1}{1 + \frac{4F^2}{\pi^2} sin^2(\frac{2\pi}{\lambda} cos(\theta))} \tag{2.19}$$

$$F = \frac{\pi\sqrt{R}}{1-R}$$

Figure 2.10 shows the transmission of perpendicular light in dependence of wavelength for two different resonator thicknesses. The wavelength range and the cavity thicknesses are chosen to demonstrate the influence of mirror reflectivity on the quality of the laser resonator, later used in Section 5. As the reflectivity increases the resonance gets more distinct and above R=90% hardly any radiation is transmitted in the region between the peaks. Additionally, an increase of

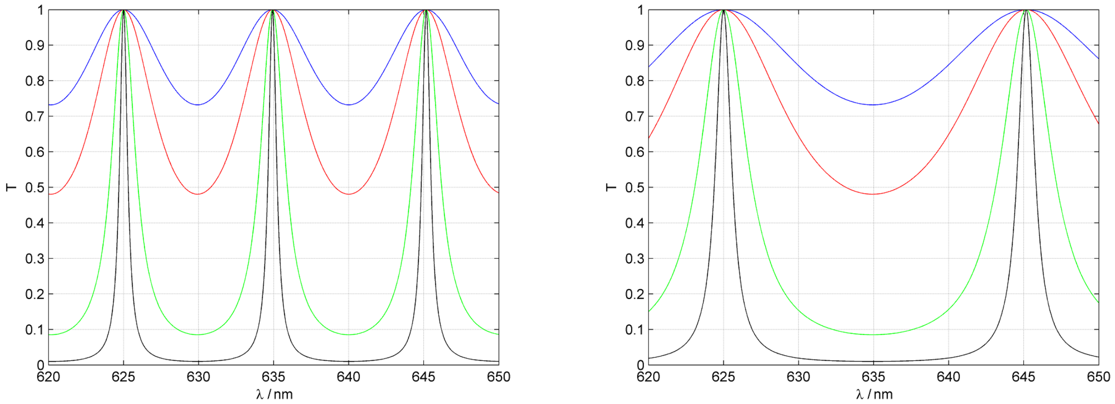

Figure 2.10: Transmittance through a loss-free plane-parallel resonator, for various reflectivities, obtained from evaluation of the Airy formula. Left figure: cavity thickness d= 20μm; right figure: d= 10μm. Reflectivities: R = 9%, R = 24%, R = 70%, R = 90%.

the resonator-thickness d yields a higher number of resonance modes but also a smaller FWHM of the peaks.

The Fabry Perot exhibits maxium transmission, according to Equation 2.18, when:

$$\delta/2 = \frac{2\pi}{\lambda_p} cos(\theta) = p\pi \tag{2.20}$$

Hence, with the resonance order p, and speed of light c the resonance frequencies are:

$$\omega_p = \frac{\pi p c}{d cos(\theta)}$$

The quality factor Q of a resonator is defined as the ratio of the peak frequencies ω_p to the width of the resonance peaks:

$$Q = \frac{\omega_p}{\Delta\omega_c}$$

The ratio of the distance $\Delta\omega_p$ between the peaks and the FWHM $\Delta\omega_c$ is the Finesse: $F = \frac{\Delta\omega_p}{\omega_c}$. Evaluating ω_p and using the Finesse yields:

$$Q = F \cdot p \tag{2.21}$$

2.9 Resonators

Besides the plane-parallel resonator, there is a number of cavity types which can be used to provide sufficient feedback for lasing. Figure 2.11 from Samuel et al. shows a summary of resonator designs, currently used for organic semiconductor lasers by means of optical excitation.

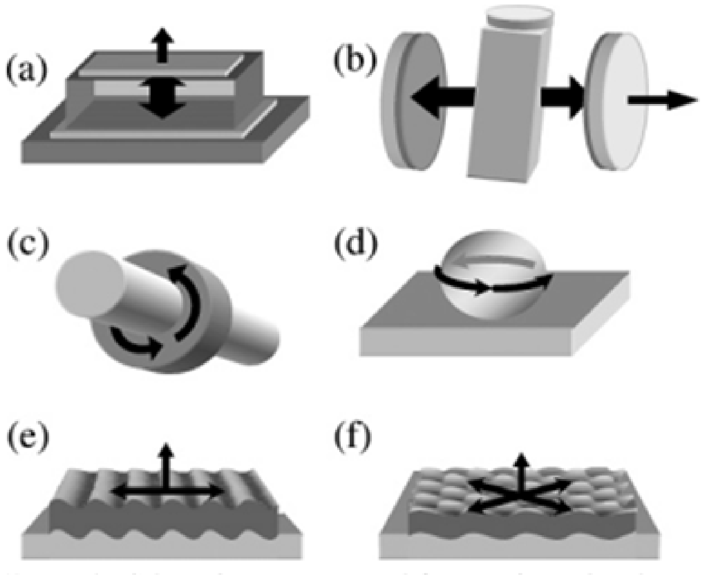

Figure 2.11: Resonator designs for organic semiconductor lasers. Arrows denote propagation directions of the resonant laser field: (a) planar microcavity, (b) Fabry-Perot dye laser, (c) microring resonator coated around an optical fiber, (d) spherical microcavity, (e) distributed feedback cavity 1D, (f) distributed feedback cavity 2D [32].

Typically used for dye lasers is the Fabry Perot Cavity, where a laser-active medium in solution is placed in between two high reflective mirrors. The condition for resonance is: A multiple of $\frac{\lambda}{2}$ should fit into the cavity width d times the refractive index n, as described in Section 2.8. The thickness is large compared to the emission wavelength λ_{Em}, which yields a smaller FWHM and very narrow located peaks. Additionally, a wavelength selective element, such as a prism or a grating is used to select a particular wavelength. For example, Kumar et al. used a "concave grating which acted as an end mirror and a 50% transmitting dichroic plane mirror as the output coupler. The grating was aligned in such a manner as to reflect the first order back into the gain medium". [33] They obtained gain narrowing as shown in Figure 2.12 with this setup by using a derivative of the organic polymer poly(para-phenylene vinylene) (BMPPV) in solution and in a blend with poly(9-vinylcarbazole).

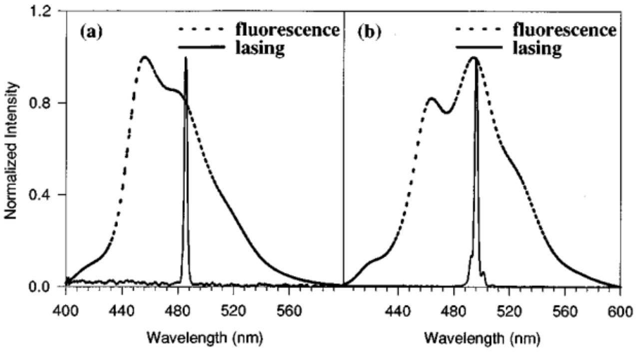

Figure 2.12: Fluorescence emission and lasing spectra of BMPPV (a) in solution and (b) in solid blend. Both solution and polymer-film were placed in an external cavity and excited by means of a pulsed, frequency doubled tunable broadband optical parametric oscillator.[33]

A microcavity design is essentially equal to a Fabry-Perot but with a micrometer scaled cavity. Xie et al. demonstrated the easiest approach for such a design, ie. lasing by means of using the naturally reflecting surfaces of an organic single crystal to provide feedback and the crystal itself acted as the laser-active medium [35]. They pumped distyrylbenzene derivative crystals with a pulsed Ar:Ion laser in a setup, similar to Figure 2.13. Important for a high quality cavity is sufficiently high reflectivity of the crystal surfaces, which is essentially determined by the refractive index of the material. The reflectivity for normally incident light on the crystal's surface can be calculated, using the refractive index n_2 of the crystal and $n_1 \approx 1$ of the surrounding air:

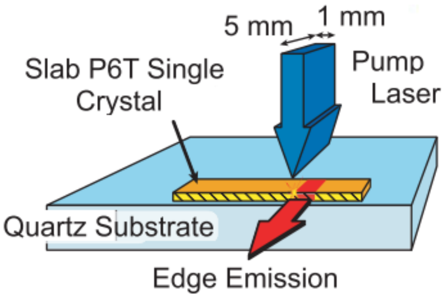

Figure 2.13: Setup for the detection of SE from an optically excited single crystal (P6T) resonator used by Ichikawa [34]. Excitation by a pulsed Ar:Ion Laser, focused through a cylindrical lens on the flat crystal surface. Feedback is provided by means of reflection from the vertical surfaces, along the width of the crystal.

$$R = \frac{(n_2 - n_1)^2}{(n_2 + n_1)^2} \tag{2.22}$$

A problem encountered in crystal resonators is insufficient surface reflectivity and thus a low resonator quality-factor. However, the reflectivity of the crystal's facettes can be improved by building a microcavity with two mirrors and with the optically active medium sandwiched in between them. This can be done, for example by means of thermally evaporating dielectric layers on top of a thin film or a crystal.

A distributed Bragg reflector (DBR) is made of a sequence of two repeating dielectric layers (refractive indices n_H, n_L). The two dielectrics preferable exhibit a large difference of their refractive indices, giving rise to high reflectivities at their interfaces, according to Equation 2.22. The sequence is $(n_H, n_L)_N n_H$, which means the first and the last layer have a high n, with N pairs of layers in between. Light with wavelength λ in vacuum, shined perpendicular onto the surface is partially reflected at each layer interface. The layers should have a thickness of

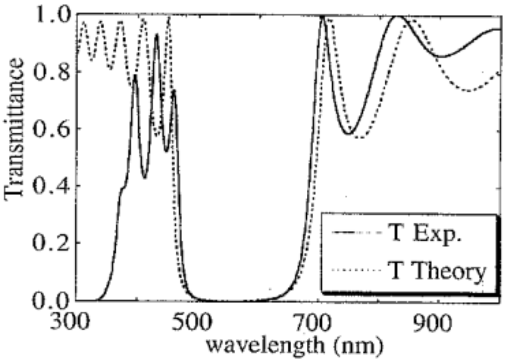

Figure 2.14: "The transmittance of a 14 layer MgF_2/ZnS DBR mirror (experiment and model). The peak of the reflectivity of this mirror is chosen as 550 nm." [37].

$d_{L/H} = \frac{\lambda}{4n_{L/H}}$. Reflections from each interface n_L/n_H exhibit a path difference of an integer times λ and light-rays reflected from n_H/n_L interfaces have path differences of multiples of $\lambda/2$ to rays reflected from n_L/n_H interfaces but with an additional phaseshift of π. Hence, reflections of the design-wavelength λ in a DBR interfere constructively. DBRs used for organic microcavities consist usually of ten or more layers and exhibit high reflectivity values of more than 95% . An example for a DBR, made of 14 layers of ZnS/MgF_2, with a thin film of PPV that was the active medium, is shown in Figure 2.14. Alltough the mirror was designed for reflecting light at 550 nm there is a broad spectral region of high-reflectance. In order to calculate the reflectance spectrum of a DBR, transfer matrices are used, first introduced by Abelès [36]. The transfer-matrix method is based on boundary conditions for the electric field at each interface between two layers. Starting from the incident E-field a matrix multiplication transfers to the E-field within the next layer thus, the transmission and reflexion spectrum of the overall layer-stack can be calculated.

Carro et al. used a tetracene single crystal, and built two dielectric mirrors by means of reactive electron-beam deposition. A tetracene crystal is placed on top of one mirror and the other DBR is directly deposited on top of the crystal. Depicted in Figure 2.15 is the structure of the microcavity, the transmission through a DBR (peak-reflexion > 99%, 21 layers: TiO_x, SiO_x) and emission from the crystal. The SE spectrum was detected by means of excitation with a cw-laser diode (405 nm) through the bottom DBR and shows significant gain narrowing to a FWHM of 3 nm [38].

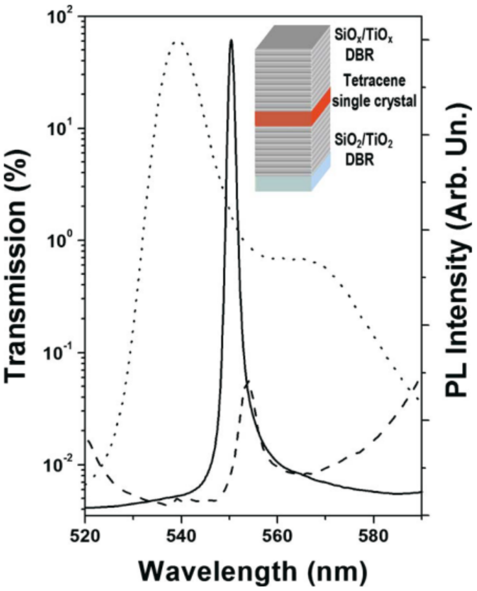

Figure 2.15: "Microcavity transmission at normal incidence: dashed line, normal PL spectra from a microcavity, continuous line and from a tetracene crystal on a bottom DBR: dotted line. Inset: scheme of the tetracene microcavity structure" [38].

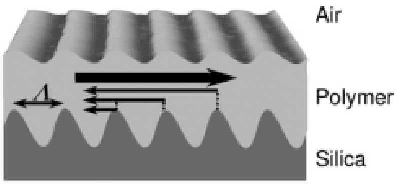

Figure 2.16: Schematic structure of a DFB laser resonator with corrugations of period Λ. Light with the resonance frequency propagating from left to right is scattered by the grating and gives rise to a diffracted part propagating in the counter direction [32].

Resonance in Distributed Feedback (DFB) cavities, such as shown in Figure 2.16, is based on a periodical variation of the optical properties of light within the gain medium. This can be achieved by structuring the material, yielding a periodical variation of the refractive index. The resonance wavelengths λ_R of such a grating fulfill the Bragg Condition:

$$m\lambda_R = \Lambda n_{eff} \tag{2.23}$$

Λ is the grating period, m the order of resonance and n_{eff} is the effective index of refraction of the material.

The first order-feedback in 1D gratings is provided along the grated surface while for higher orders a contribution appears perpendicular to the surface as well. In Figure 2.11 two different DFB designs are shown with a 1D and 2D grating respectively. Due to the structure of the periodicity in a 2D grating, the feedback can take place in various directions along the grating surface. Samuel et al conclude ”For while the 2D lasers also combine excellent spectral selection with a reasonably long cavity length, they can exhibit improved output beam quality, lower threshold, and higher output efficiencies than their 1D counterparts.” [32]

Common ways to realize DFB lasers are by deposition of a polymer thin film directly on a grating, or by pressing a patterned stamp into a polymer film. The laser-emission wavelength of a DFB structure can be varied by changing the grating period but also by changing the layer thickness, thus the effective refractive index of the waveguide is altered as well. For example Karnutsch et al fabricated Polymer 1D and 2D DFB lasers by spin-coating a polyfluorene derivative polymer onto SiO_2 substrates. They demonstrated laser operation in the wavelength range of 438 nm to 459 nm under pulsed excitation by varying the grating period and the film thickness. [39]

It should be noted that instead of periodical variation of the refractive index of a material, a spatially periodic variation of the excitation in a DFB scheme is sufficient to obtain feedback. A simple way to achieve this is interference exposure using a setup for two-beam interference, as was done by Yamao et al. [40]. They exposed an oligomer crystal slab to the interference pattern of pulsed laser light, directly and reflected from an aluminum mirror (Loyd -configuration), and observed gain narrowing.

Other resonator designs like Microring or Microspheres, shown in Figure 2.11, emphasize the simple processability of organic semiconductor materials. For example, the Microring laser, can be realized by dipping a fiber into a concentrated polymer and upon withdrawal a thin polymer film stays on the surface. Due to the length of the circumference and total internal reflection of light within the thin film, distinct resonance frequencies (whispering gallery modes) can build a standing wave around the fiber-core. Because of the rather long distances of several hundred μm around the core, SE can build up more easy than in microcavities. However, due to the longer path-length more longitudinal modes are supported and the distance between resonance frequencies is smaller. Also, the emission from these structures is not a well-defined beam because of the resonator-shape. Applications may be in sensor technology rather than in conventional optics.

3 Organic Semiconductor Rubicene

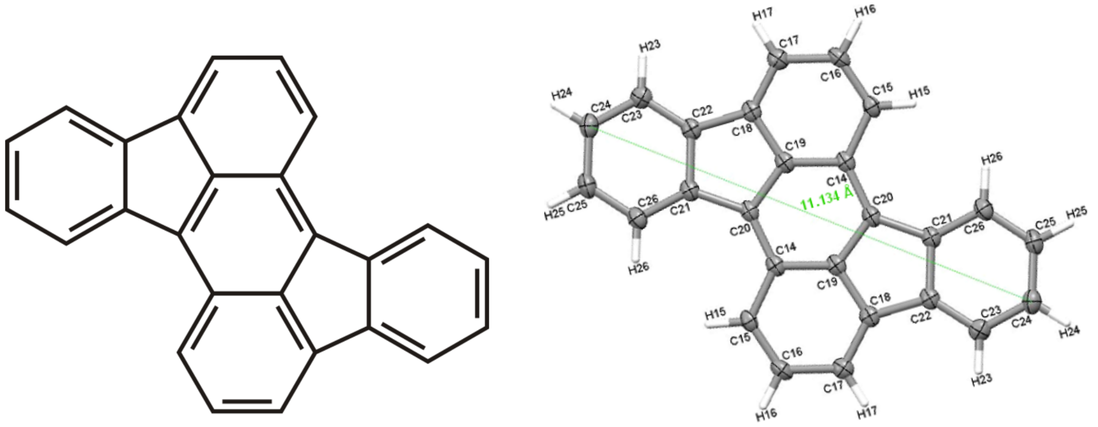

(a) (b)

Figure 3.1: (a) Chemical structure of Rubicene $C_{26}H_{14}$ and (b) Visualization of geometric structure of Rubicene [19].

Rubicene belongs to the group of aromatic polycyclic hydrocarbons and consists of five phenyl-rings, where three phenyls share two carbon atoms each and two are attached on the side, as shown in Figure 3.1 (a). Its molecular weight is 326.4 g/mol and the melting point, listed by the supplier (Acros Organics) is 305 °C. Rubicene is an organic semiconductor, exhibiting fluorescence, and which posses promising properties for optoelectronic applications. Figure 3.1 (b) visualizes the geometric structure of a Rubicene molecule within a Rubicene-single crystal, obtained from XRD measurement data. The molecule is planar and the longest distance between two atoms is indicated in Figure 3.1 (b).

3.1 TG and DSC

Thermogravitmetry (TG) and Differential Scanning Calorimentric (DSC) measurements were performed on Rubicene powder. TG measures the mass change of a sample as the temperature increases due to heating of the sample. In DSC the difference in heat flow rate between a sample and a reference sample upon heating of the sample is monitored.

A change in the heat flow, used to rise the temperature of a sample, indicates a thermodynamic event. The Gibbs free energy plays a significant role:

$$G = U + pV - TS$$

With the internal energy U, pressure p, sample volume V, temperature T, and entropy S. We calculate the change of G:

$$\mathrm{dG = dU + Vdp + pdV - Sdt - TdS}$$

Substitution of U by: $\mathrm{dU = SdT- pdV}$ and neglecting a possible change of the number of particles yields:

$$\mathrm{dG = Vdp - TdS}$$

At constant pressure a thermodynamic process is supposed to minimize the Gibbs free energy since the entropy is maximized [41]. Also, the aggregate state of a material at a specific temperature and pressure corresponds to a minimum of G. At the point of a phase transition G is the same for both aggregate phases involved. However, the first derivative of G, ie. $S = -(dG/dT)_p$, jumps at a first-order phase transition because the slopes differ from each other when the transition from the Gibbs free energy of one aggregate state to the other takes place. A consequence of the entropy-jump at a first-order phase transition is the latent heat, ie. the supply or removal of additional energy. The latent heat is measured, e.g. when a sample starts to melt in DSC, since additional energy needs to be supplied for raising the temperature compared to the reference.

Shown in Figure 3.2 are results of DSC and TG measurements for Rubicene powder. The displayed TG-curve indicates a sublimation process of Rubicene starting at 361°C. At the end of this procedure nearly all of the Rubicene powder has vanished, indicating that the sample is completely evaporated. The DSC-peak at 316.8°C suggests a phase transition. The Rubicene powder starts to melt and the second peak at 448.1°C is again due to the sublimation process.

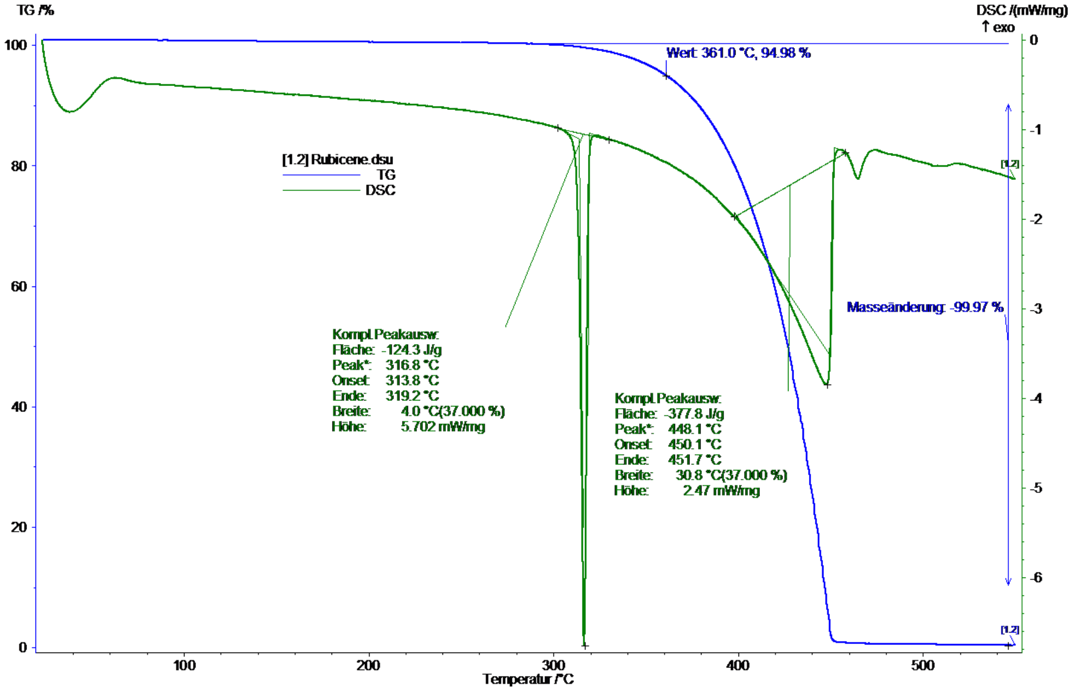

Figure 3.2: TG and DSC measurements performed on Rubicene powder.

3.2 Solution & Crystal

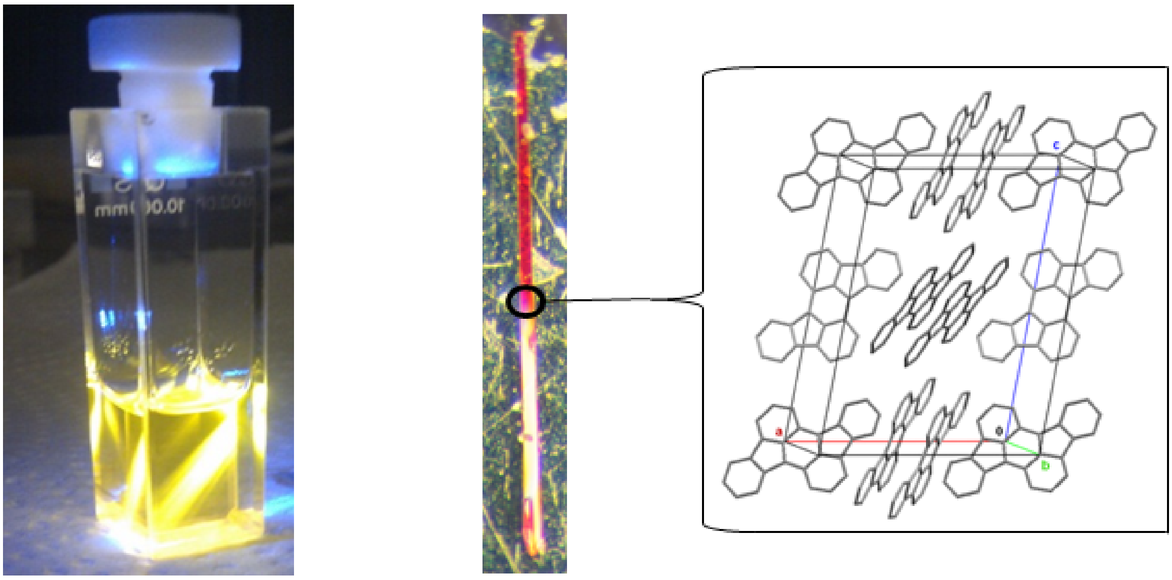

(a)

(b)

Figure 3.3: (a) Rubicene in Toluene, c = 0.002 g/l , illuminated by a 457 nm Ar:Ion Laser beam at 15 mW and, (b) Rubicene crystal observed in optical microscope and monoclinic crystal structure from [19].

Rubicene was dissolved in Toluene and crystallized by means of slow solvent evaporation. Figure 3.3 a) shows the solution, illuminated by an Ar:Ion Laser beam and strong orange fluorescence intensity is observed. Figure 3.3 b) depicts a Rubicene single crystal illumined by white LEDs in a microscope. The growth process by means of solvent evaporation as well as the structural characterization of the Rubicene single crystals are described in [19]. X-ray diffraction (XRD) measurements revealed a monoclinic unit cell with the following dimensions:

$$a = 15.98\,\text{Å},\;\; \alpha = 90\,^{\circ},\;\; b = 5.11\,\text{Å},\;\; \beta = 97.26\,^{\circ},\;\; c = 19.06\,\text{Å},\;\; \gamma = 90\,^{\circ}$$

The Rubicene crystals are up to a few millimeters long and needle-like. Their thickness is between 10 μm and 25 μm while their width is generally larger than the thickness, up to 100 μm. Previous investigations, done by Hirzer, revealed a bandgap of 2.25 eV for Rubicene dissolved in Toluene and 2.07 eV of solid Rubicene in its single crystalline allotrope [19].

Further improvement of crystal quality and of the growth process may be realized by means of crystallization from the vapor phase in a furnace tube. Rubicene powder is placed in a sealed glass tube and filled with an inert gas such as Argon. The glass tube is heated on a hot plate which induces a temperature gradient. Evaporated material starts to condense on areas with a lower temperature hence crystals start to grow there. A similar furnace was used by Kim et. al. to grow high-quality needle-like Rubrene crystals [42].

3.3 Thin Film

Besides Rubicene in solution and as a single crystal, also photophysical properties of a Rubicene thin film were investigated during our measurement series. The thin film was prepared by thermal evaporation of Rubicene powder on a glass substrate and on a silicon substrate. Figure 3.4 shows two microscope pictures (magnification: 500 times) of a Rubicene thin film on a Silicon substrate. Figure 3.4 a) displays the film illuminated by an halogen lamp in a reflexion setup while in Figure 3.4 b) the beam of a laserpointer (λ_{Em}=405 nm) was directed on the film from the side. One notices a distribution of small crystalline islands rather than a homogeneous film, especially when illuminated by the laser beam.

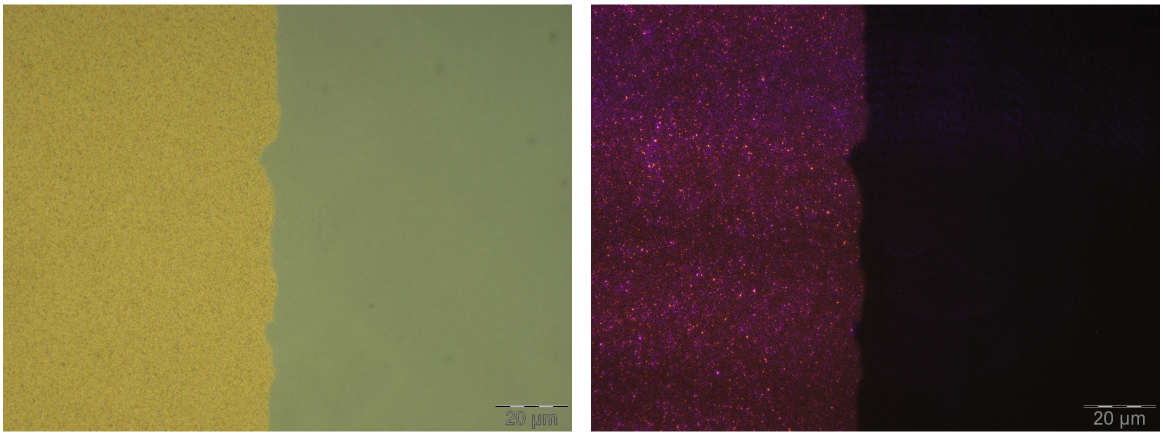

(a) (b)

Figure 3.4: Rubicene thin film on Si substrate, thickness $d \approx 22\,\mathrm{nm}$. Illumination in a) from top by halogen light source and in b) from the side by 405 nm laser (power$< 50\,mW$).

The fabrication of the thin film included the following steps:

- Plasma etching of Si-Substrate for 30 s
- Cleaning with a CO_2 spray
- Heating of Si-Substrate at about 120 °C for 1.5 hours
- Conditions prior to the evaporation: Substrate-Temperature T = 25 °C; pressure p= $1.6 \cdot 10^{-6}$ mbar
- Thermal evaporation for 2.5 min to a film thickness of 22 nm.

The film thickness was measured in-situ using a quartz-microbalance, that is placed close to the sample during the deposition process. Upon deposition of molecules on the microbalance its Eigenfrequencies change and the thickness can be calculated by this frequency drift. Since sample and microbalance are on different places a tooling factor is usually introduced to calculate the film-thickness from the thickness of the layer, that was deposited directly on the microbalance. Therefore, one has to measure the thickness of a specific sample after a deposition process to get the tooling factor, which was not possible in our case. Additionally, a frequency drift of the microbalance at the beginning of the deposition process also contributes an additional uncertainty of the film-thickness that may be higher than 22 μm.

Figure 3.5 shows an atomic force microscopy (AFM) image of the Rubicene thin film on Si-substrate. In contrast to electron microscopy, where in general a conducting sample surface is required, in AFM also insulating samples can be observed at high resolutions, beyond limits of optical microscopy. In an AFM setup a fine tip scans the surface with a very small distance between tip and surface, or by means of making contact to the sample surface. The tip is on top of a cantilever that changes its location because of the forces between tip and surface. Detection can be done by means of optical deflection of a laser beam from the cantilever. Also, the change of the cantilever's resonance frequency can be detected with phase sensitive detection, resulting from a change of forces between tip and surface thus implying a different surface chemistry.

The AFM image shows a distribution of micro-crystals rather than a homogeneous polycrystalline film with small grain boundaries between crystallites. Polycrystalline films consist typically of crystallites surrounded by small volumes without material, due to dislocations or imperfections at the crystallite boundaries. Instead, in the AFM image large micro-crystals up to 1 μm are observed with empty regions of similar volume between them, yielding a jagged structure. A linescan was conducted along the line, indicated in Figure 3.5 and is shown on the bottom of the figure. The fragmented nature of the film can be seen as well as the height difference of up to 90 nm.

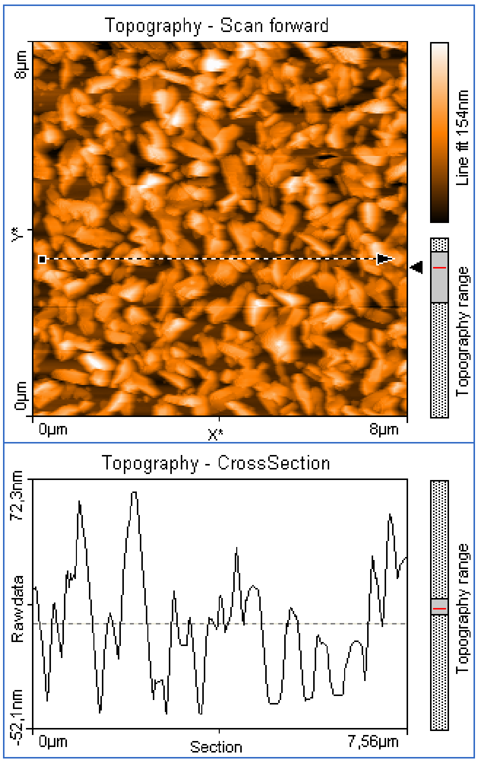

Figure 3.5: Atomic Force Microscopy image of Rubicene thin film on Si-substrate, on top and linescan, indicating the height distribution along the line, shown on the bottom.

In order to measure photophysical properties of a Rubicene thin-film, Rubicene was thermally evaporated on a glass substrate, following the fabrication steps:

- Cleaning of glass-substrate in ultrasonic bath
- Cleaning with a CO_2 spray
- Heating of Substrate to about 120 °C for 1.5 hours
- Conditions prior to the evaporation: Substrate-Temperature $T = 25\,°C$; pressure $p = 1.5 \cdot 10^{-6}$ mbar
- Thermal evaporation for 1.6 min to a film thickness of 29 nm, measured by the microbalance

For applications in opto-electronics, the thin film-topography needs to be well-controlled and, in general, more homogeneous than our current Rubicene thin films. However, a promising approach yielding an even Rubicene thin film may be melting and recrystallization. Especially promising could be the approach to melt-recrystallize Rubicene by heating powder on a substrate. This technique was demonstrated by Hibino et al. for some oligomers, eg. anthracene and p-nP (para-phenylene, n=4-6) crystals [43]. They also observed emission-gain narrowing after recrystallizing the oligomers between quartz substrates and by optical pumping with a pulsed N_2 laser.

4 Photophysical Measurements

4.1 Fluorescence and Absorption

Essential for the usage of organic semiconductors in optoelectronic applications are the characteristics of the photoluminescence and absorption. In this section we give an overview of properties of the photoluminescence emission such as the luminescence lifetime, and properties of absorption. Rubicene in solution and as a crystal was examined. However, we performed some experiments only with the solution, eg. quantum yield determination or exclusively on the crystal, such as high pressure experiments.

4.1.1 Solution

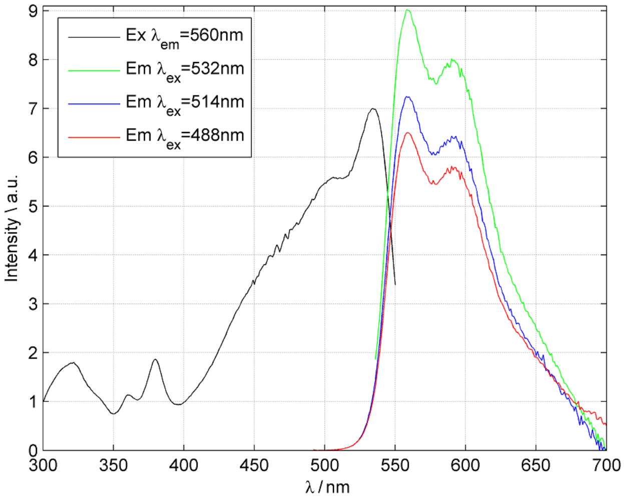

Figure 4.1: Emission and excitation spectra of a Rubicene-Toluene solution, concentration: 0.01 mg/ml.

Emission spectra and excitation spectra of Rubicene dissolved in Toluene were measured. The solutions were prepared as part of a Master's thesis at the Solid State Physics institute by Andreas Hirzer. "The Rubicene powder was refined twice via gas transport sublimation to increase the purity to $> 99\%$ and the solution was filtered through a $0.22\,\mu$m syringe filter to prevent aggregations and impurities." [19]. In order to perform fluorescence measurements part of the Rubicene solution was poured into a quartz cuvette with an optical path length of 10 mm. The measurements of excitation and emission spectra were performed with a Shimadzu photofluorometer RF-5301 equipped with monochromator-gratings of 1300 lines/mm for emission and excitation. Figure 4.1 shows the emission and excitation spectra of Rubicene in solution taken at medium scan velocity. The excitation spectrum (black line) was taken at a constant emission wavelength of 560nm. The fluorescence emission was measured at three different excitation wavelengths according to three of the lines emitted from an Ar:Ion Laser, 532 nm, 514 nm and 488 nm. All measurements were also carried out at three different scan velocities in order to exclude a time constant of the same order as the scan velocity. The emission wavelength for the excitation spectrum was specified at 560 nm thus giving maximum emission intensity. The spectra show strong fluorescence when illuminated at the three different wavelengths in a spectral region between approximately 550 nm and 675 nm. Emission spectra were recorded at different concentrations and two excitation wavelengths.

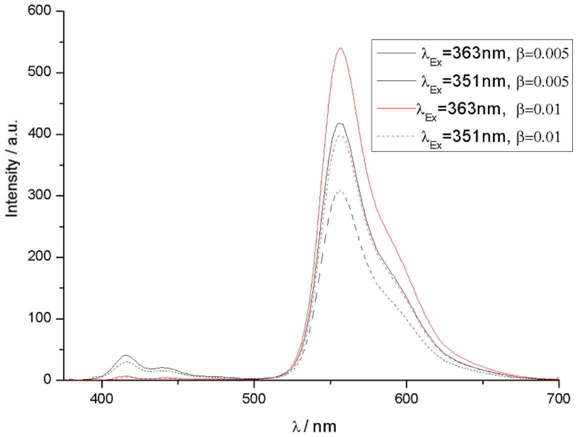

Figure 4.2: Emission spectra of a Rubicene-Toluene solution for two concentrations β in g/l and emission wavelengths in nm.

Emission of Rubicene in solution at two concentrations and at higher excitation energy is shown in Figure 4.2. The excitation wavelength of λ_{Ex}=350 nm corresponds to an Ar-Ion laser-line and is used in Figure 4.2. One notices other transitions appearing at higher excitation energies. However, the new features of the fluorescence spectrum are concentration dependent. As the concentration increases, the emission intensity of the transitions decreases with respect to the energetically lower transitions. We suppose the reason for this is a higher absorptivity when the concentration increases and since the excitation spectrum shows finite excitation intensity at the new transitions these are absorbed stronger and less radiation intensity escapes the solution.

Figure 4.3 shows results of a fit to the emission, performed with MATLAB using a non-linear least square fit algorithm in order to determine the transition positions. The best fit was obtained for a sum of three Gaussians, centered at 554 nm, 578 nm and 615 nm, respectively. These are three vibronic progressions of $S_0 \rightarrow S_1$.

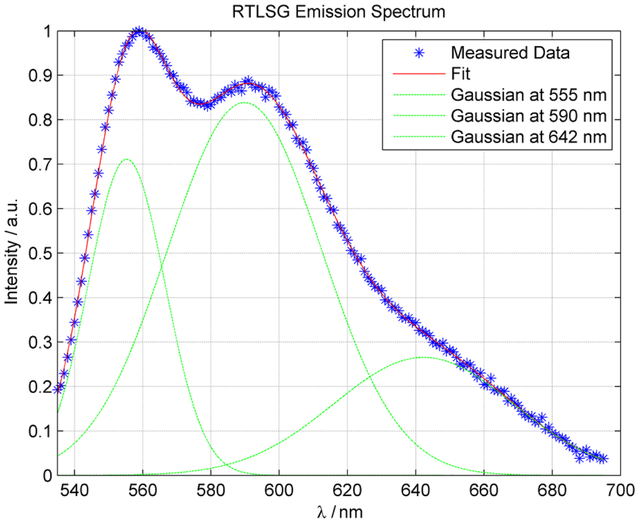

Figure 4.3: Emission of a Rubicene-Toluene solution at $\lambda_{Ex} = 532\,nm$; concentration: 0.01 mg/ml, fitted as a sum of three Gaussians.

Absorbance and excitation of Rubicene in Toluene are compared to each other in Figure 4.4. Excitation was determined on the Shimadzu RF-5301 and the absorbance was measured with a Perkin-Elmer λ9 transmission-spectrometer. Excitation and absorbance have nearly the same shape. From the position of the absorption edge at about 550 nm the bandgap between Homo and Lumo is calculated to be 2.25 eV, as previously noted in [19].

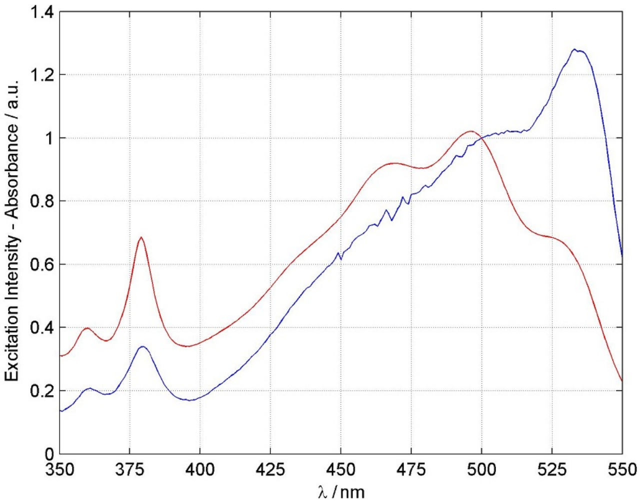

Figure 4.4: Excitation compared to absorbance of a Rubicene-Toluene solution. Absorbance and emission scaled for better visualization of absorption edge.

4.1.2 Single Crystal

Similarly to the procedure applied to the Rubicene solution, emission and excitation spectra of Rubicene in its crystalline form were measured. Rubicene crystals are birefringent and have refractive indices of n=1.84 for parallel and n=2.95 for vertical polarized light. Parallel polarization is considered to be parallel to the long crystal axis. The fluorescence intensity of a crystal is stronger for the polarization direction perpendicular to the long crystal axis. This could be observed by illuminating the crystal with a diode laser at 532 nm and 4.75mW in an optical microscope and observing the fluorescence through a polarization filter. Figure 4.5 shows a Rubicene crystal illuminated from the side. The picture was taken for perpendicular and parallel orientation of the emission polarization filter. The fluorescence emission spectrum of a Rubicene crystal was recorded by putting a crystal directly on the optical fiber of a MS125 CCD spectrometer and illuminating it with a laser diode emitting at 532nm and 4.75 mW, as mentioned in [19]. However, the fluorescence of the crystals is surprisingly strong thus providing the possibility to record emission as well as excitation spectra by means of excitation with an incoherent light source. The spectrometer Shimadzu RF3501 is built for usage with cuvettes, therefore, a special sample holder was constructed to keep the crystal in place during the measurements. A glass capillary with an inner diameter of approximately 2 mm is inset in an aluminum cube and for enhanced stability capillary and cube are inserted into a plastic cuvette. To maximize light transmission, holes were cut into two side panels of the cuvette as shown in Figure 4.6 with a crystal already placed in a cuvette and illuminated for illustration.

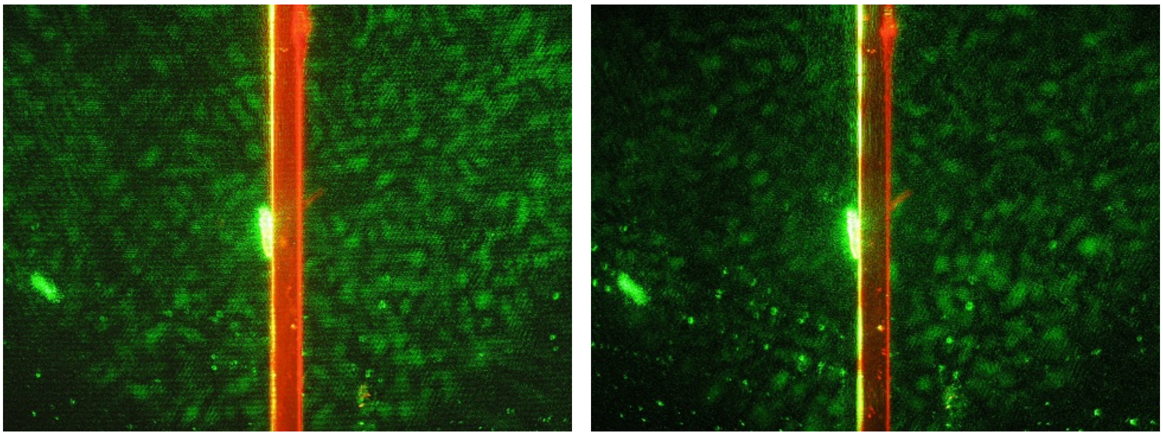
(a) ⊥ (b) ∥

Figure 4.5: Emission of a RCN single crystal observed in an optical microscope through polarization filters. Perpendicular Polarization: ⊥, parallel polarization: ∥

In Figure 4.7 a normalized excitation spectrum of the Rubicene crystal is compared to a normalized emission spectrum. Three emission spectra are taken at constant excitation wavelengths but at different positions of the crystal in the capillary. Red spectrum: crystal parallel and next to excitation aperture, horizontally oriented. Black spectrum: parallel and next to the emission aperture, vertically oriented. Green spectrum: Back of capillary, vertically oriented. A previous calculation of the Homo-Lumo gap in [19] from the position of the absorption edge gap yielded

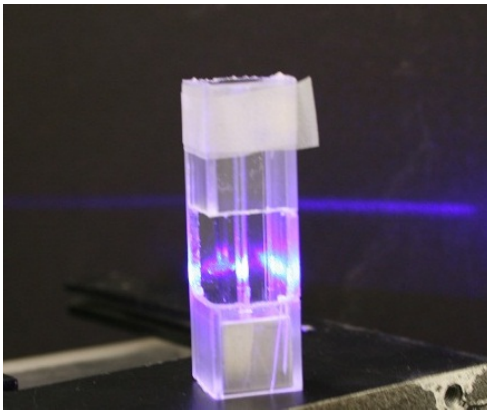

Figure 4.6: Sample holder for single crystal fluorescence measurements. Glass capillary in aluminum cube, inset in a plastic cuvette with holes peerced in sidepanels, illuminated with Ar-Ion Laser at 457 nm

a value of 2.07 eV which can be confirmed by the position of the falling edge of the excitation spectrum at about 600 nm in Figure 4.7.

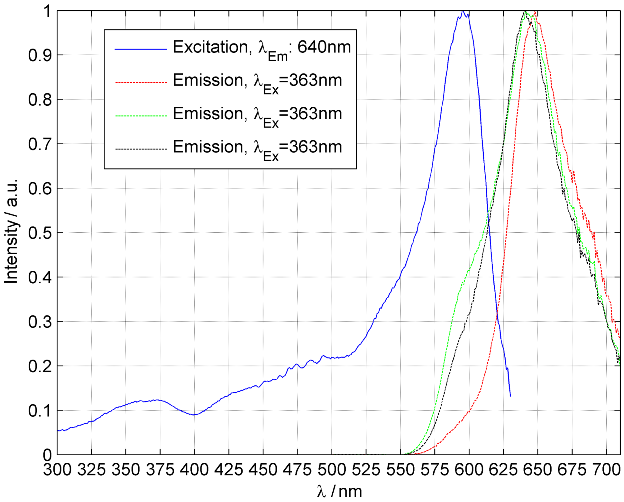

Figure 4.7: Emission and excitation of a RCN single crystal obtained in a Shimadzu RF3501. Emission taken at different positions of the crystal.

The shape of the emission in Figure 4.7 indicates three transitions, forming the main part of the emission, and a fourth for the tail.

Again MATLAB was used to fit a sum of three and four Gaussians (Equation 2.4) respectively. Fit results for three emission spectra to three gaussians are shown Figure 4.8. The peak positions are constant within 6 nm but the compliance of fit and measured data is not very good. The average positions are: 601 nm, 641 nm, 669 nm, respectively.

Figure 4.9 shows fits to four Gaussians, thus improving the fit quality by an additional transition located at about 615 nm. All three fits are of good quality, and although, the shape of the emission is different it is worthwhile to note a compliance of the peak positions within the three fits. Best fit quality was obtained with the first two peaks located within 2 nm while the positions of peak number three and four are shifted by 6 nm. The average positions are: 597 nm, 614 nm, 641 nm and 672 nm, respectively.

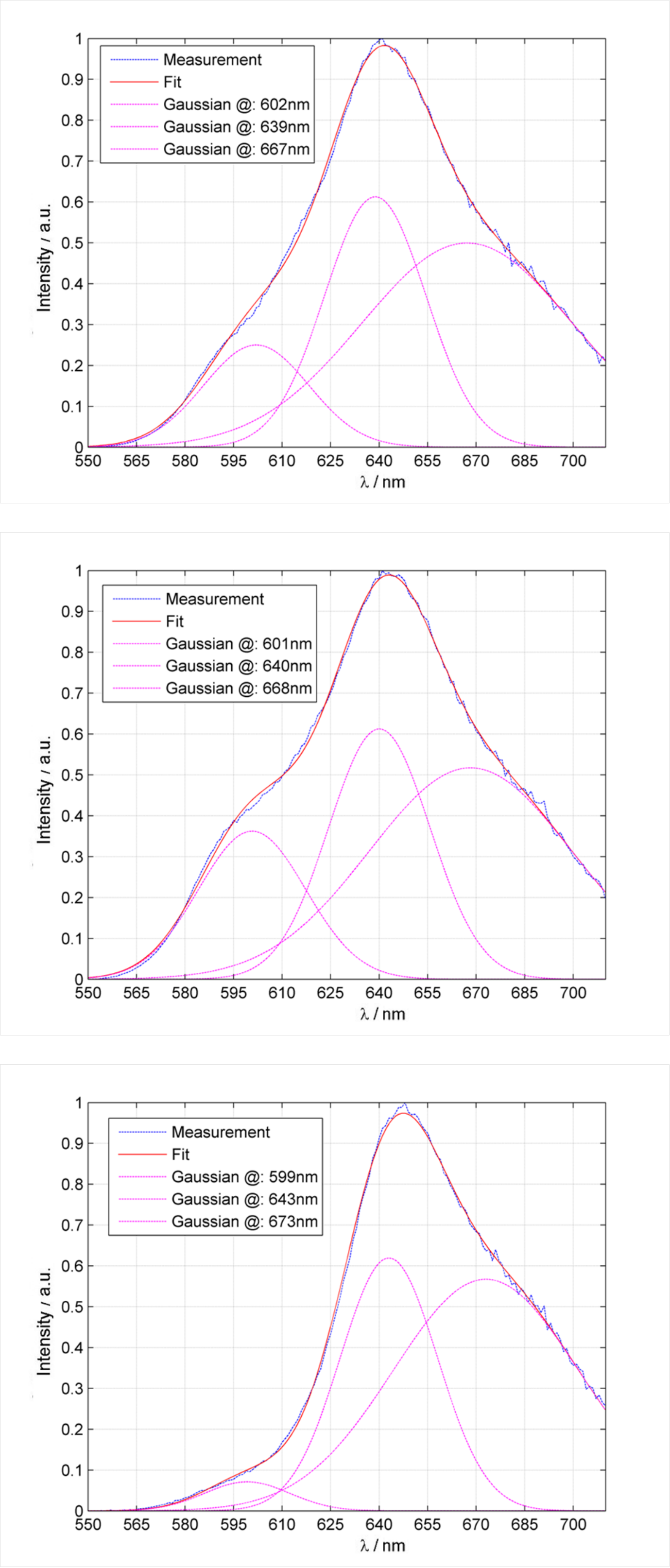

Figure 4.8: Red line: Emission of a Rubicene single crystal was fitted through three Gaussians. Black line: Same spectra as in Figure 4.7. Dotted lines: Three Gaussians used for the fit.

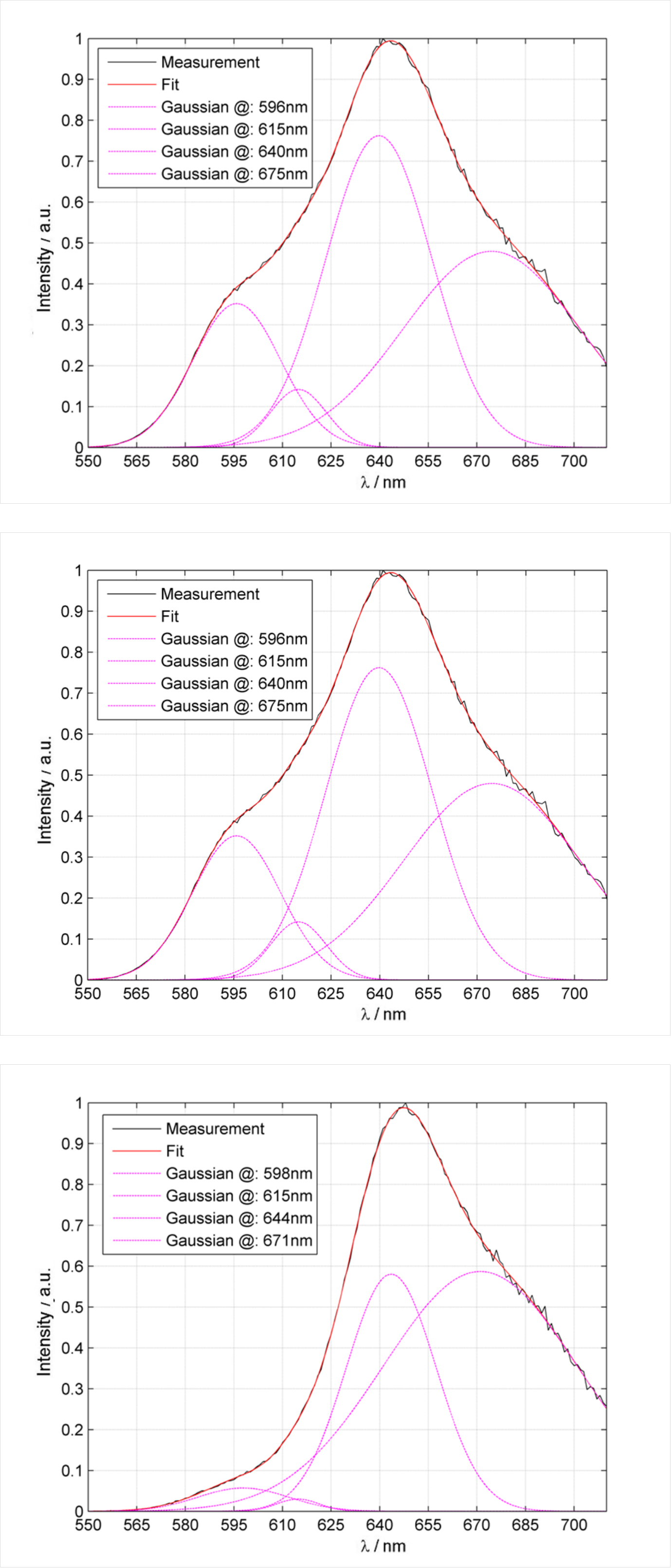

Figure 4.9: Red line: Emission of a Rubicene single crystal was fitted through four Gaussians. Black line: Same spectra as in 4.7. Dotted lines: Four Gaussians used for the fit.

An important observation about the crystal's fluorescence is the change of shape of the emission depending on the spatial position of excitation and detection. A possible reason is self-absorption of light emitted by material. Assessment of this can be done by looking at the overlap of emission and absorption (or excitation). The excitation spectrum in Figure 4.7 overlaps with the crystal's emission. One emission-peak overlaps completely, thus being the $0 \rightarrow 0$ transition, that is the radiative transition from the zeroth vibrational level of the first exited state to the zeroth vibrational level of the groundstate. Also, a part of the second emission characteristic overlaps, the $0 \rightarrow 1$ transition. Since there is finite absorption at the emission wavelength a fraction of the emission intensity gets re-absorbed within the crystal. The emission fits shown in 4.9 support our reasoning. While the position of each peak stays about constant - they vary only a few nanometers - the amplitudes of the first two Gaussians increase. The first one changes more significantly than the second one, thus being in line with a higher self-absorption of the first transition.

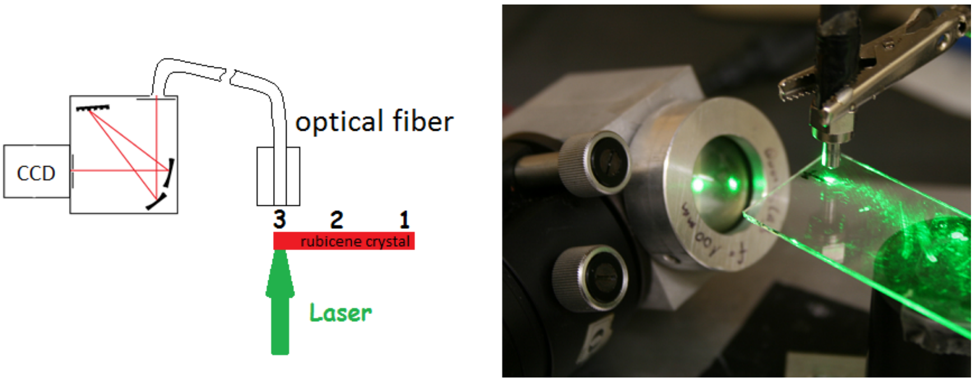

Figure 4.10: Setup for the detection of a rubicene crystal's fluorescence spectrum by means of an optical fiber. Excitation with a 532 nm diode laser. Schematic drawing on the left indicates positions of the optical fiber for detection.

To further investigate the effect of self-absorption, laser light was focused on one end of a Rubicene crystal. The optical fiber for detection with the MS125 CCD Spectrometer was moved along the crystal's long axis. Figure 4.10 shows a picture of the experimental setup for the illumination of the crystal and the detection via an optical fiber. Intensity calibration of the CCD- spectrometer MS125 was performed by means of a tungsten-ribbon lamp Osram WI17/G. Spectra were recorded at three positions: Above the excitation spot, in between both ends, and at the opposite end. The measurements in Figure 4.11 comply with the previously stated theory of self-absorption. The intensity decreases when the fiber is moved further away from the excitation and the peak moves to a higher wavelength due to a longer lightpath in the organic crystal. A longer path is equivalent to more absorption according to Equation 2.1. In conclusion, the measurements support that the peak shift in RCN single crystals occurs due to self-absorption within the crystal.

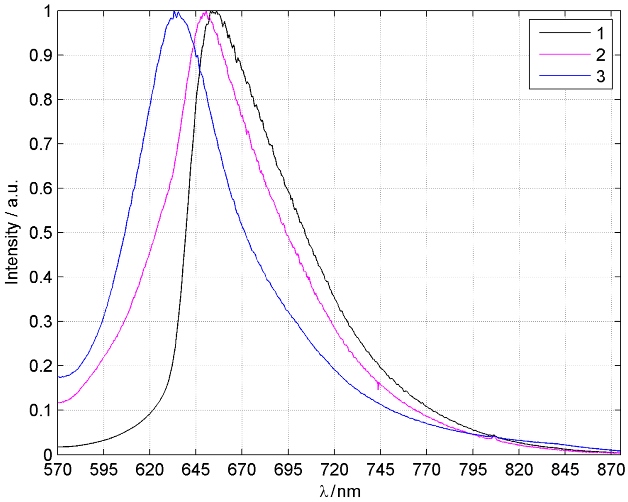

Figure 4.11: Self-absorption measurement of RCN crystal by CCD equipped Spectrometer MS125.

4.1.3 Thin Film

Emission and excitation spectra of a Rubicene-thin film on glass substrate were measured with the Shimadzu RF-5301. The glass substrate was affixed on one side of a built-in cuvette holder, turned to yield an incident angle of about 40 °. The emission intensity of the film is very weak due to the structure, ie. the film is not homogeneous but pronounced island formation can be observed as described in Section 3.3. Another reason for the weak intensity detected is the small film-thickness (about 30 nm). The measurements were recorded through cut-off filters, because of the weak fluorescence intensity and a superimposed background. We used a 550 nm cut-off filter during the emission measurement and the excitation was recorded through a 610 nm cut-off filter, thus avoiding direct scattering of the excitation into the entry slit of the emission monochromator. Figure 4.12 shows emission and excitation of the thin film recorded under measurement conditions, as mentioned above. The data, especially above 650 nm, is very noisy, partly due to the weak emission intensity and also due to a low detector sensitivity of our measurement device at high wavelengths. Rough determination of the location of the two pronounced peaks yields 590 nm and 680 nm. The emission spectrum is therefore red-shifted compared to the emission from rubicene in solution but the thin film still emits at longer wavelengths than the Rubicene single crystals.

The measured spectrum was fitted to a sum of four Gaussians in order to determine the transition energies more precisely. Figure 4.13 shows a comparison of the fit result to the measured data. Although the fit function seem to approximate the emission spectrum reasonable, especially the peak position at 679 nm does not appear to be proper aligned because it is located at nearly the same energy as the peak at 678 nm. The reason for this is the high noise at high wavelengths, making a proper determination of the peak location impossible. The other peak positions are depicted in Figure 4.13.

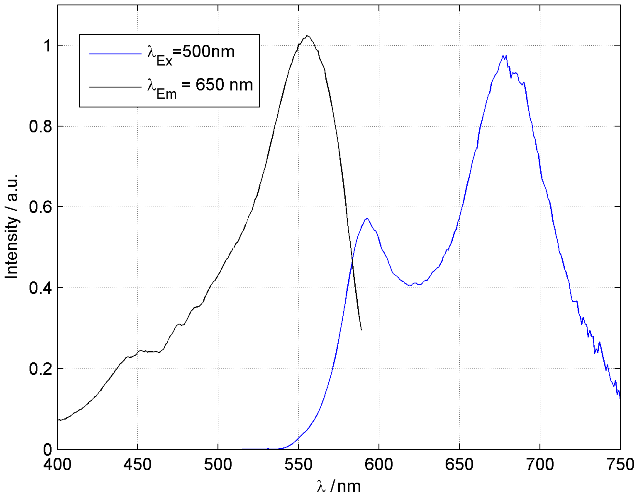

Figure 4.12: Emission spectrum of Rubicene thin film on glass substrate recorded through 530 nm cut-off filter and excitation spectrum recorded through 610 nm cut-off filter on Shimadzu RF-5301 Photofluorometer.

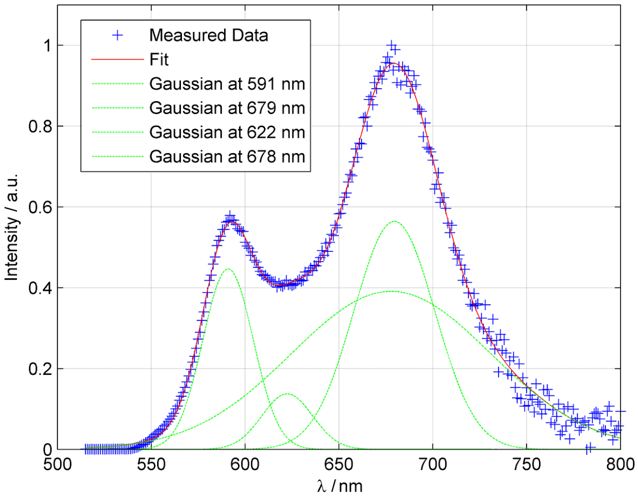

Figure 4.13: Fit results of an emission spectrum of Rubicene thin film on glass substrate recorded through 530 nm cut-off filter on Shimadzu RF-5301 Photofluorometer. The fit is a sum of four Gaussians located at the positions indicated in the legend.

Figure 4.14 presents the transmission through a Rubicene film on glass-substrate. The specimen was measured in a Shimadzu UV1800 spectrometer with medium scan velocity and 1 nm slit width. From both, transmission and excitation spectra, the absorption edge location is approximately at 575 nm, yielding a bandgap of 2.16 eV, which lies in between the values obtained for solution (2.25 eV) and single crystal (2.07 eV).

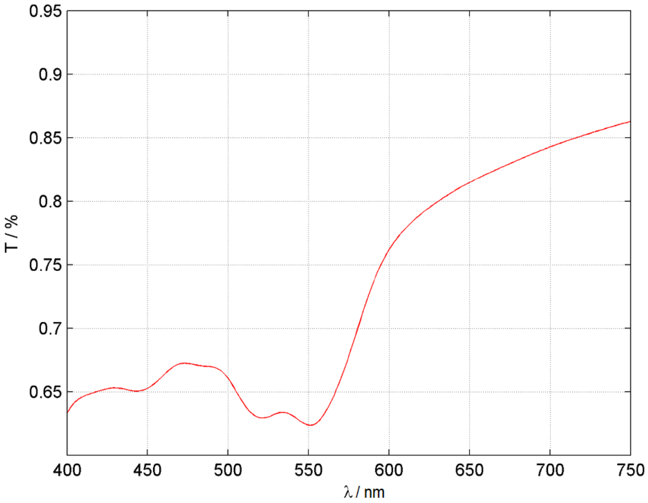

Figure 4.14: Transmission of Rubicene thin film on glass substrate recorded on a Shimadzu UV1800

4.2 Lifetime

Fluorescence lifetime measurements were performed with an ISS K2 fluorometer, operating in the frequency domain as described in Section 2.5. Both, solution and single crystal lifetimes were determined.

4.2.1 Experimental Setup

The measurement device is an ISS Greg 200 with an ISS K2 software upgrade. A schematic view of the measurement setup is depicted in Figure 4.15. Light for sample-excitation is emitted from a laser and reflected by prisms through a scrambler to depolarize the previously linear polarized light.

The unpolarized light travels through a Glan-Thomson polarizer and linearly polarized light continues to the Pockels cell where the amplitude modulation takes place. The Pockels cell is an electro-optic modulator; light modulation is realized on virtue of the Pockels effect. The birefringence of a crystal is proportional to an applied electric field, therefore, a voltage-dependent speed-difference of the ordinary part and the extra-ordinary part of the initially linear polarized light is induced. This results in the appearance of a fraction of light with perpendicular polarization direction. A DC-base voltage is applied superimposed by an AC voltage, ie. an amplified signal from a high-frequency synthesizer. Convenient operating conditions of the Pockels cell are a DC- Voltage of 300 V and an amplitude of the amplified signal from a frequency synthesizer in the range of 50 V to 25 V. The DC Voltage as well as the lightpath through the pockels cell is chosen in such a way that the fraction of modulated light compared to cw-light exceeds m=0.1 at ν =2 MHz. A new high-frequency amplifier was installed in order to obtain a measurement range from 0.1 MHz to 250 MHz.

The excitation light gets reflected by a mirror and passes again through the Pockels cell to increase the Pockels effect. The Glan-Thomson polarizer filters the modulated direction of polarization and the modulated light continues through a monochromator (1300 l/mm) to a beam splitter. The reflected part gets detected by a photomultiplier tube (PMT), type: Hamamatsu R955, to monitor the excitation signal. The other part excites the sample or gets scattered from a reference liquid. The reference is used to define an origin, ie. a zero point for the phase, and to scale the modulation appropriately. The phase ϕ used in the experimental results is a subtraction of the reference phase ϕ_{ref} from the sample phase ϕ_s while the modulation m is $\frac{m_s}{m_{ref}}$. We used Glycogen in 18Ω-water as a reference-scattering solution. Light emitted by the sample passes through a cut-off filter and is collected by a PMT. The filter is used to hinder laser stray light from reaching the detector. It is also possible to insert polarization filters into the paths of the excitation light and the emitted light. There are two frequency synthesizers, Master and Slave phase locked and with a difference of 80 Hz (cross-correlation frequency). Output signals from the PMTs are fed into an ADC and data processing is performed by means of FFT.

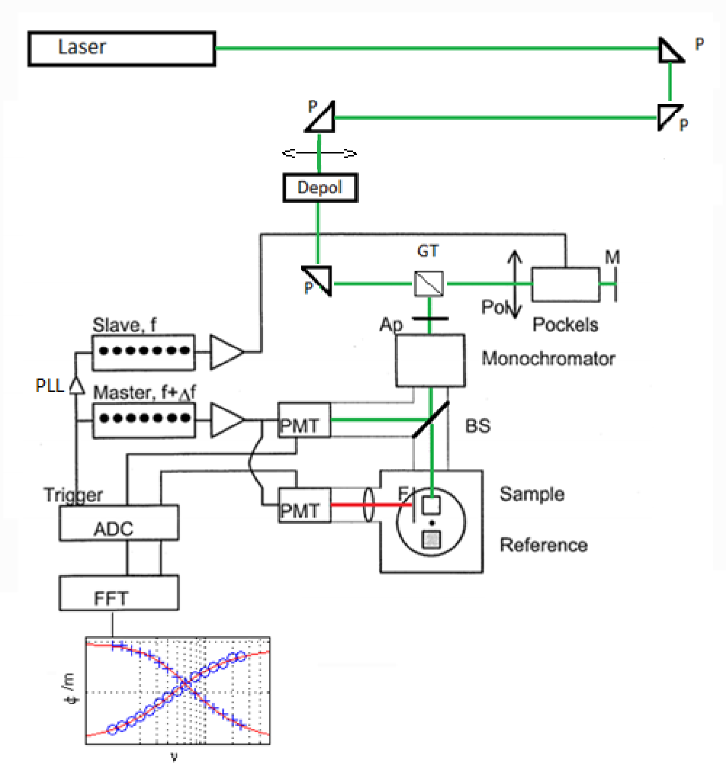

Figure 4.15: Setup of phase-fluorometry measurement for lifetime detection. Green indicates the path of the excitation-light; red is the path of the emitted/ scattered light. Ap... Aperture, ADC... Analog to digital converter, BS... Beamsplitter, F... Filter to eliminate stray light, FFT... data processing by fast fourier transform, M... Mirror, P... Prisma, Master... frequency synthesizer: f, Slave... phase locked to master: $f + \Delta f$, PLL... Phase locked loop, PMT... photomultiplier tube, Pol... Polarizer, Laser... Argon- Ion laser, Pockels... Pockels cell, Depol... Depolarizer, GT... Glan-Thomson Beamsplitter.

4.2.2 Solution

The fluorescence lifetime of Rubicene dissolved in Toluene was measured our setup. Two solutions with different concentrations, $c_1 = 0.05\,g/l$ and $c_2 = 0.002\,g/l$ were prepared. In Figure 4.17 phase and modulation of c_2 are shown. The scattering solution, glycogen in water, as well as the sample solution were measured in 10 mm pathlength-Quartz cuvettes, shown in Figure 4.16 at the left. Starting from a high concentration of glycogen, the concentration was lowered until the DC signal of sample and reference were within 5%. The excitation wavelength was 360 nm and the emission was collected through a 530 nm cut-off filter.

Both solutions yielded the same fluorescence lifetime within limits of uncertainty. A simple single exponential model is suitable and yields $\tau_\phi = 5.8\,ns \pm 0.08ns$ and $\tau_m = 5.9\,ns \pm 0.03ns$. The depicted uncertainty is the standard deviation of the lifetimes obtained from the evaluation of the fit-model.

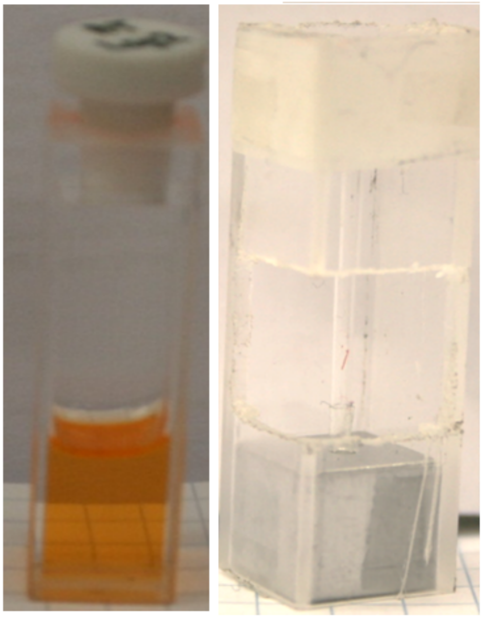

Figure 4.16: Sample holders - quartz cuvette (10 mm pathlength) with Rubicene solution and self-designed holder for single crystal and reference liquids.

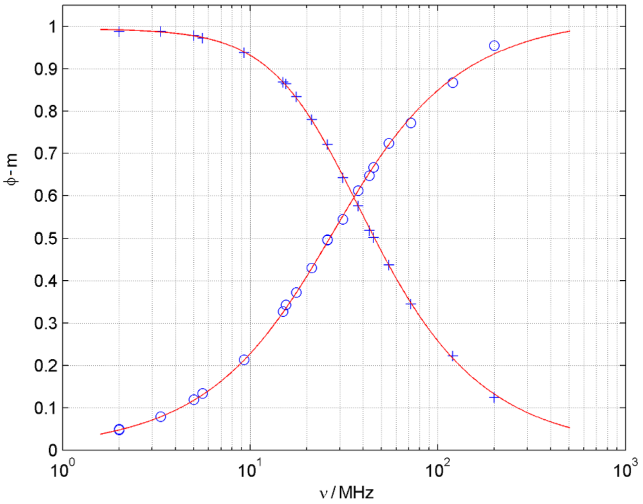

Figure 4.17: Phase $\phi/90$ and modulation m over modulation frequency ν. Single-exponential fitting yields: $\tau_\phi = 5.8\,ns$ and $\tau_m = 5.9\,ns$.

4.2.3 Crystal

Lifetime of Rubicene single crystals were determined using a self-designed sample holder shown in Figure 4.16 at the right. The crystal sticks to the inner wall of a glass-capillary (diameter: 2mm) by means of adhesion. The glass capillary is inset in a 1cm^3 aluminium cube which, in turn, is fitted in a plastic cuvette with holes in the side-panels. In order to obtain significant

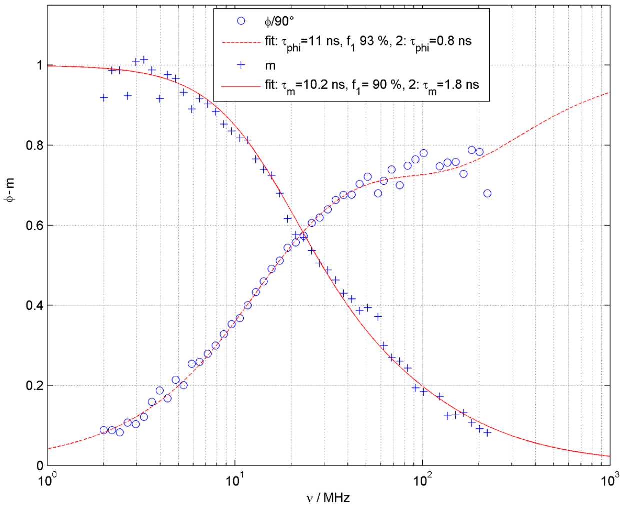

Figure 4.18: Phase $\phi/90$ and modulation m over modulation frequency ν. Double-exponential fit results are depicted in the legend. Measurement with more datapoints to enhance accuracy.

data it is important for the emission to come from a region of similar homogeneity and spatial dimensions as the scattered light from the reference liquid. Therefore, the scattering solution was stored in the same holder thus confining the glycogen-water solution to a region of similar size as the sample crystal. Figure 4.18 shows phase and modulation of a rubicene crystal excited at 457 nm. The fluorescence decay does not obey a simple single exponential decay law. A least-square fit of a double exponential model results in a large fraction ($f_1 \approx 93\%$) of a species decaying at $\tau_1 \approx 10$ ns and a species decaying at $\tau_2 = 1 - 2$ ns. Fit results of both measured variables, phase and modulation, are shown in the legend of Figure 4.18.

Uncertainty of datapoints and fit in this case is higher compared to the measurement of the rubicene solution; device bandwidth limitations of the setup are one reason. Since one fraction of excited states decays fast, at about $\tau_2 \approx 1$ ns, high modulation frequencies above 100 MHz are necessary. Dicker [28] suggests an accessible data range of $0.5ns < \tau < 200ns$ for a frequency range of $2\,MHz < \nu < 250\,MHz$ on the basis of a sufficiently high variation of phase and modulation respectively. However, to distinguish the lifetime τ_2 from τ_1 frequencies above 100 MHz are more significant, because there the data differs greatly from a single exponential decay with τ_2. However, above 100 MHz dephasing of the emission compared to excitation is already substantial due to the longer lifetime τ_2, and therefore the emission intensity shrinks. Since also the amplitude of the amplified synthesizer signal decreases with increasing frequency, the modulated fraction of excitation light declines and a severe decrease of the system resolution follows.

The geometries of the sample and reference holder, respectively are tested within this thesis. In contrast to measurements of solutions the light is not emitted from exact the same region as the scattered light. Within the preparations prior to the measurement, the size of the illuminated region of the sample holder was adjusted through varying the position of a lens in the path of the excitation light. Varying the illuminated region alters the modulation m of the reference and of the sample but not in the same way. Therefore, the measurement procedure was to initially set the lens position to get a modulation of $m \approx 1$. At the same time neutral (gray) filters were used an further we adjusted the glycogen concentration in order to get a cw-light intensity of both, sample and solution that is within ±10%. Changes of the detected light intensities during the measurement seemed unavoidable due to turning of sample- and reference-holder, despite our efforts to obtain stable measurement conditions.

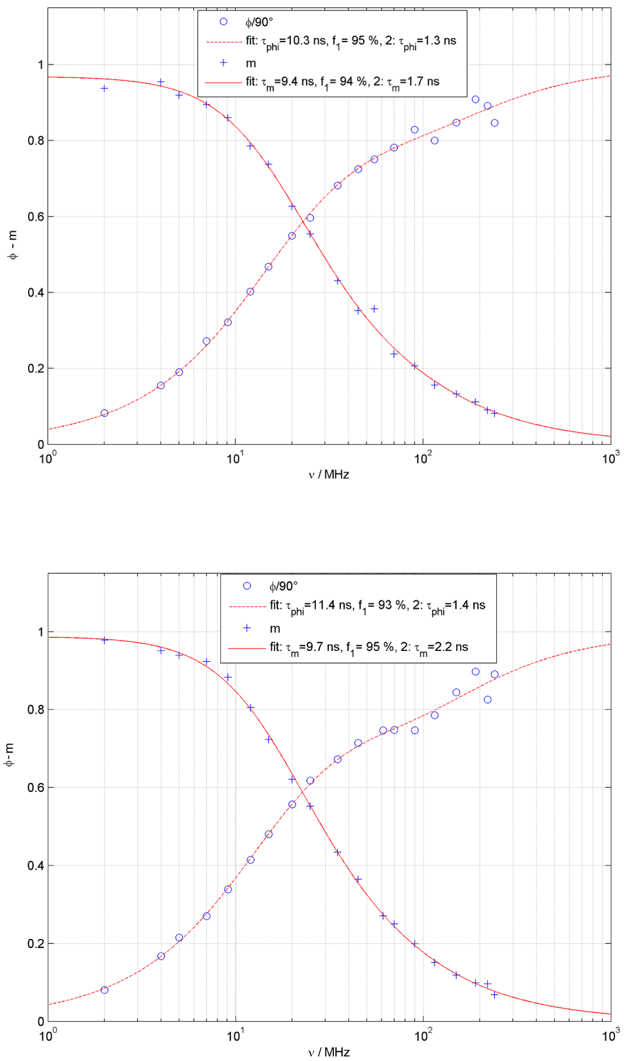

Figure 4.19: Phase $\phi/90$ and modulation m over modulation frequency ν. Double-exponential fit results are depicted in the legend. Fluorescence detection of parallel/ perpendicular polarization with respect to long crystal axes.

The bi-exponential decay behaviour of Rubicene single crystals seems rather exotic. Therefore, further investigations were made to explain its origin. Since the molecule is birefringent and we found a difference in emission intensity for both polarization directions a connection to the appearance of two lifetimes is expected. Hence, lifetime measurements with polarization filters in the emission lightpath were carried out. Figure 4.19 shows results of two measurements of the polarization perpendicular and parallel to the long crystal axes. However, no significant changes of the decay behavior between the measurements were observed. In both cases a short decay time ($\tau_2 = 1\,\mathrm{ns}$) and a longer decay time ($\tau_1 \approx 10\,\mathrm{ns}$, $f_1 = 93\%$) appears.

4.2.4 Discussion

We compare our results of the fluorescence lifetime decay to Transient Absorption (TA) measurements done by Burdelt et al. on Tetracene in solution, thin film and single crystals [44]. They found a single exponential decay behavior of the solution (τ_f=4.2 ns), similar to the decay behavior of Rubicene. They reason, that the fluorescence decays completely due to intersystem crossing to the T_1 state. They observed a bi-exponential fluorescence decay behavior of single-crystal tetracene with a short part ($\tau = 80\,\mathrm{ps}$) coming from rapid exciton-exciton fission and a longer part (τ=5-10 μs) due to delayed fluorescence. Therefore, Tetracene and Rubicene single crystal both exhibit bi-exponential fluorescence decays however, the measured decay times differ significantly.

4.3 Quantum Yield

4.3.1 Measurement

We determined the quantum yield (ϕ_f) of Rubicene in Toluene by means of measuring absorptivity and luminescence Intensity for two concentrations of the solution as well as for two different excitation wavelengths (λ_{Ex}). The procedure is described in detail in a review by Wuerth et al [30], where the quantum yield is calculated with Equation 2.13 by measuring the absorbance and the fluorescence emission of the sample and of a reference, with known quantum yield. Additionally we changed the formula according to Section 2.6 by using the slopes of integrated photon flux, calculated from the emission intensity depending on the fraction of absorbed photons, calculated from the absorbance.

Two ϕ_f-standard solutions were used, Rhodamine B (RHB) in Ethanol and Rhodamine 6G (RH6G) in Ethanol. RH6G is commonly used standard with a quantum yield of 0.94 [45]. Kubin et al determined ϕ_f of RHB to be 0.65 at 25°C [46] while Karstens and Kobs measured ϕ_f for RHB at various temperature yielding $\phi_f \approx 0.55$ at 25°C [47]. Ten minutes prior to the measurements Argon was bubbled through the solutions in order to exhaust the solutions from oxygen. Then the quantum yield of Rubicene and RHB was calculated using RH6G as the standard in Equation 2.15.

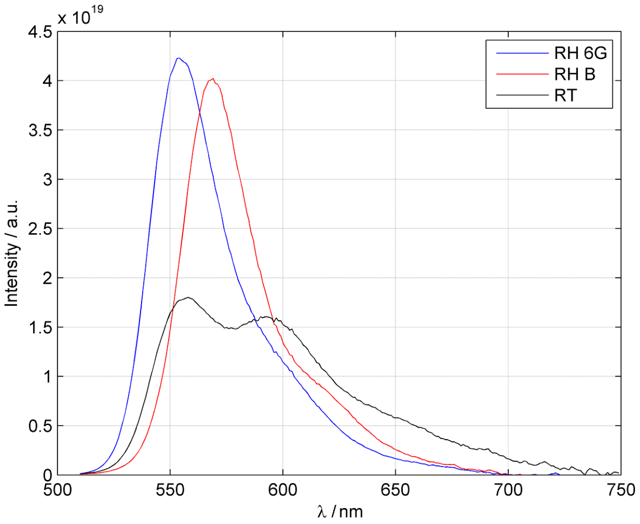

Figure 4.20: Intensity corrected fluorescence emission recorded at $\lambda_{Ex} = 500\,nm$; Highest concentrations of Rhodamine 6G, Rhodamine B, both in Ethanol and Rubicene in Toluene respectively.

Two solutions with different concentrations of three luminophores were prepared with absorbances well below 0.1 in order to avoid self-absorption and to make sure the excitation beam passes through the whole width of the cuvette with our fluorophores with negligible intensity gradient. Figure 4.20 shows emission spectra recorded on the Shimadzu RF-3501. The three solutions emit in similar spectral regions and the measured intensities are on the same order of magnitude as well, hence the standards are well suited. The measurements were performed with excitation at λ_{Ex}=488 nm, medium scan velocity and slit sizes of 3 nm for both excitation slit and emission slit. We also conducted QY-measurements with λ_{Ex}=500 nm, which made a decrease of the excitation slit to 1.5 nm necessary because of a higher absorbance and, thus, a higher emission intensity of the Rhodamines at 500 nm compared to 488 nm.

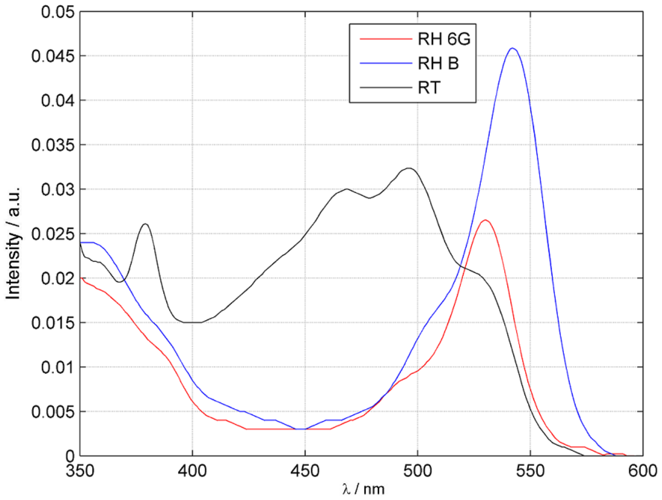

Figure 4.21: Absorbances measured on Shimadzu UV1800 of Rhodamine 6G, Rhodamine B and Rubicene in solution respectively. Lower concentration in Table 4.1 used. The background from Toluene and Ethanol is subtracted for further calculations.

Absorbance spectra of three solutions are shown Figure 4.21, measured on the Shimadzu UV1800 with a slit width of 1 nm. The calculations were performed with corrected absorbance values, ie. the solvent-absorbances were subtracted from all measured absorbances of the fluorophores.

Table 4.1: Concentration in g/l and solvent of Rubicene , Rhodamine 6G (RH 6G), Rhodamine B (RH B) in solution used for quantum yield measurements.

Fluorophore	Rubicene	RH 6G	RH B	Rubicene	RH 6G	RH B
Concentration	$2\,10^{-3}$	$0.8\,10^{-4}$	$1.2\,10^{-4}$	$1.2\ 10^{-3}$	$0.5\,10^{-4}$	$0.7\,10^{-4}$
Solvent	Toluene	Ethanol	Ethanol	Toluene	Ethanol	Ethanol

We measured emission spectra of our solutions with concentrations according to Table 4.1, performed an intensity correction and converted the intensity to a unit proportional to the number of emitted photons. Then the integration over the whole emission region, ie. from 500 nm to 750 nm, was performed yielding a quantity proportional to the integrated spectral fluorescence photon flux F. F is plotted in dependence of the fraction of absorbed photons f, calculated by Equation 2.14 from the corrected absorbance, in Figure 4.22. Using the procedure and formula from Section 2.6 the quantum yield was calculated from the slope of a straight line, fitted to two measured concentrations as well as the origin of all three solutions. Fit results are depicted in the legend of Figure 4.22. For both excitation wavelengths RH6G was used as the standard with a fixed quantum yield of 0.94. The value mentioned in the literature of about 0.6 for our second standard, RHB are close to the obtained value of $\phi_{f,RHB}$ =0.62 and $\phi_{f,RHB}$ =0.59

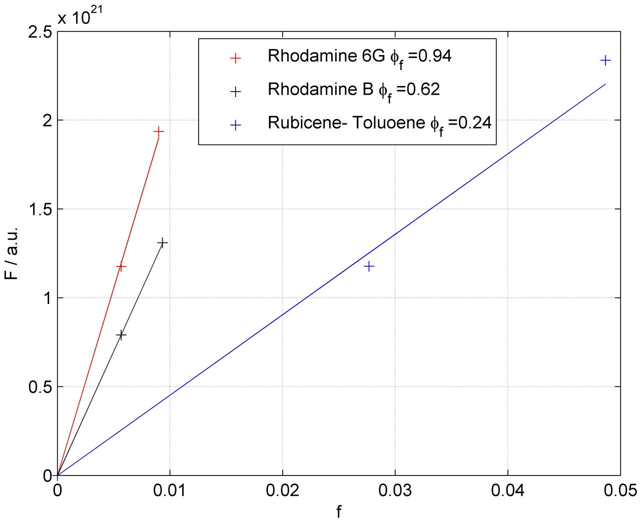

(a) $\lambda_{EX} = 488\,\mathrm{nm}$

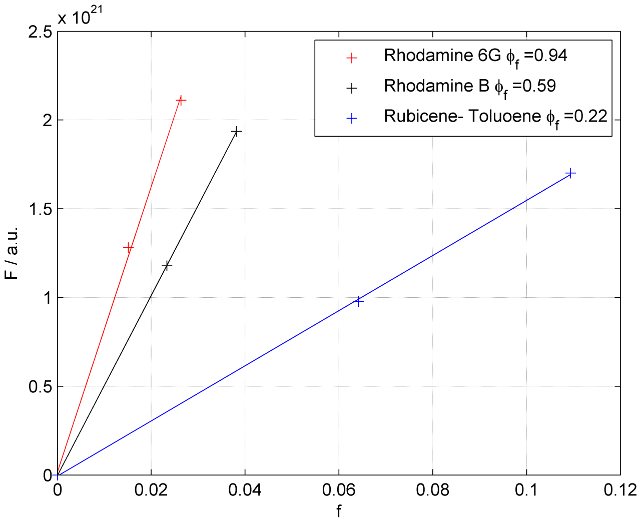

(b) $\lambda_{EX} = 500\,\mathrm{nm}$

Figure 4.22: Integrated spectral fluorescence photon flux F in dependence of fraction of absorbed photons f for three solution, each measured at two different concentrations and two excitation wavelengths. Fits of straight lines are shown as well.

respectively. Therefore the obtained quantum yields of $\phi_{f,RT}$=0.22 and $\phi_{f,RT}$=0.24, respectively, for Rubicene in Toluene seem reasonable.

4.3.2 Uncertainty

The obtained quantum yield values of Rubicene seem reliable as outlined above. Nevertheless, some sources for measurement uncertainties remain and need to be discussed. The indirect measurement method of using a standard solution with known QY and a fluorescence spectrometer relies to an high extend on an identical geometry, hence, the excited region in sample and reference must be the same. Additionally, self-absorption effects need to be ruled out by using concentrations of the luminophores with absorbances well below 0.1.

The spectral sensitivity of the detector must be in good agreement with the sample's emission spectrum. Organic semiconductors exhibit broad spectral emission regions, making this hard to achieve. The sensitivity of the used spectrometer is shown in Figure 4.23 and is compared to the intensity-correction emission in Figure 4.20. One notes a rather low sensitivity above 670 nm thus yielding an additional uncertainty for Rubicene due to higher noise in this region, while our Rhodamines emit at sufficiently low wavelengths to be in good agreement with the detectors sensitivity.

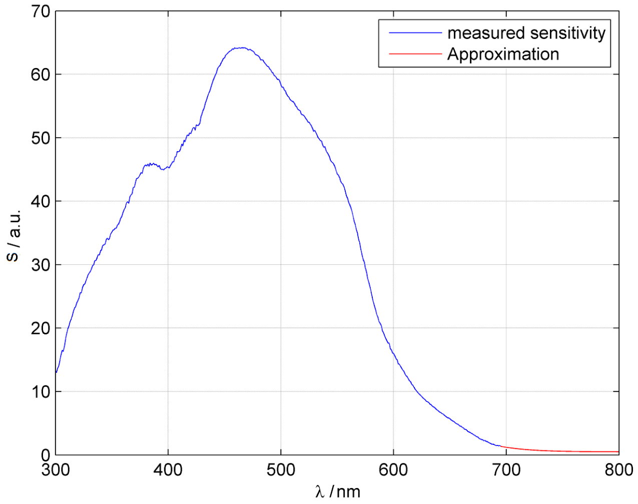

Figure 4.23: Spectral Sensivity S of the spectrometer Shimadzu RF3501, used for recording emission intensities in QY-measurements.

4.3.3 Discussion

A previous measurement of ϕ_f was performed by Schmidt and yielded $\phi_f = 0.21$ for Rubicene in Toluene [48], thus being in line with our measurement results. Toluene is an aromatic solvent, that may influence the luminescence of Rubicene therefore, luminescence quantum yield measurements with another non-aromatic solvent are interesting for future experiments. Apart from fluorescence, other transition processes are contributing significantly to the excited state decay. Comparison with Tetracene is reasonable because the backbone of Rubicene consists of three phenyl rings (anthracene), and both molecules exhibit a planar geometry. Also, compared to Tetracene with $\phi_f = 0.16$ [49] the quantum yield of Rubicene is on a similar order of magnitude.

Transitions between singlet and triplet states are forbidden, due to the spin-flip involved in such transitions. Previously mentioned by Groff et al. is the possibility to observe splitting of a singlet exciton into two triplet excitons, ie. singlet fission: $S_1 \rightarrow 2T_1$ in Tetracene [50]. Two triplets may recombine further to: $2T_1 \rightarrow S_0 + S_1$ yielding delayed fluorescence from the S_1 state.

Burdett et al. reasoned that in Tetracene the S_1 state is located energetically above the T_1 state, in particular: $\mathrm{E}(S_1) \approx 2\mathrm{E}(T_1)$ [44]. Hence, transitions from singlet to triplet manifold are likely, where a singlet fissions into two triplets, but also the transition $2T_1 \rightarrow S_1$, ie. delayed fluorescence can take place. Burdett et al. find a single-exponential fluorescence decay of tetracene in solution (τ=4.2 ns) similar to our experimental result for Rubicene in solution (τ=6 ns) [44]. They find that the triplet state is produced in solution and can be observed when measured at long delay times in transient absorption (TA) experiments, once interfering singlet excited state absorption features have decayed away. Similar excited state dynamics might be the reason for the weak fluorescence quantum yield of Rubicene and for the bi-exponential fluorescence decay behavior of the single crystal. TA experiments on Rubicene might yield further insights into the excited state transitions.

4.4 High Pressure

Experiments under high-pressure conditions provide a powerful tool to investigate optoelectronic properties of solids. Upon application of high pressures structural and optical properties of a material change, providing evidence for changes on the molecular level. Organic crystals are an ideal class of materials for such experiments because of their weak intermolecular forces, that manifest themselves, for example in low-temperature melting points. Thus application of pressure induces significant changes in the crystal structure and further in the electronic and vibrational levels. Among other techniques observation by means of Photoluminescence measurements is used to measure these changes and support the fundamental understanding of organic solids.

We investigated Photoluminescence properties of Rubicene single-crystals under high pressure conditions up to approximately 40 kbar using a diamond anvil cell (DAC). In the DAC a sample is contained within a metal gasket between the parallel culets of two diamond anvils. Upon pushing the two diamonds together the sample is subjected to high pressures. The DAC is an important tool to investigate the electronic structure of materials or phase transitions via XRD or fluorescence measurements among other experimental techniques.

4.4.1 Preparation

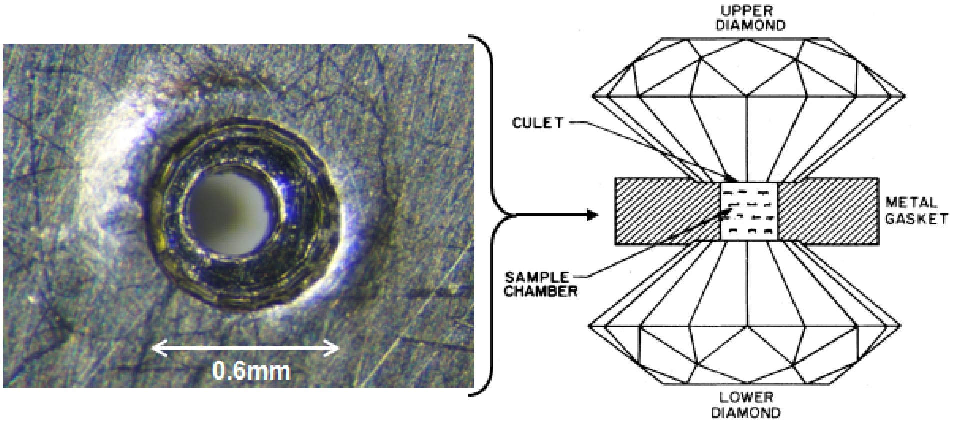

Figure 4.24: Diamond anvil high-pressure cell (DAC). Right: Metal gasket with sample chamber between diamond anvils [51]; Left: Stainless steal gasket; Thickness: 0.2 mm, indented to half its thickness, drilled sample hole: 200 μm.

Diamond Anvil Cell

Figure 4.24 shows the sample chamber in the metal gasket squeezed between two diamond culets and a picture of a pre-indented stainless steel gasket. The metal gasket holds the sample in place and separates the diamond anvils to prevent them from destruction if force is applied to the diamonds. The sample floats in a hydrostatic pressure-transmitting medium in order to avoid large pressure gradients that will occur if a sample is squeezed directly between the diamond culets. The gasket material must be a hard metal to withstand high pressure from the anvils and to prevent the sample-hole from excessive deformation. As the desired pressure increases a harder material is necessary, commonly stainless steel, Inconel or Rhenium are used. Four essential points to consider during preparations for safe and well defined operation conditions of the DAC are:

1. Metal Gasket
2. Pressure Calibration
3. Pressure Transmitting Medium
4. Loading

Metal Gasket

The maximum pressure that can be reached with a material depends on the gasket thickness, as well as the hole diameter and the size of the diamond culets. In gasket selection we follow the guidelines presented by Dunstan and Spain, who write in their review about theory and usage of DACs: For example, a DAC with 0.6 mm culets and a 200 μm sample-hole in a middle-hard stainless steel gasket, with a thickness of 0.1 mm can be used up to a maximum pressure level of 10 GPa while a gasket thickness of 40 μm under the same conditions can be used up to a pressure of 50 GPa [52, 53]. The maximum stated pressure values are where a transition from a stable (thin-gasket) to an unstable (thick-gasket) operational regime of the gasket appears. In the stable region, that is at sufficiently low pressure and low gasket-thickness, the metal near the sample-hole extrudes inwards. Increasing the thickness for constant (high) pressure leads eventually to an unstable region. There, the metal extrudes outwards, the sample-hole gets larger and asymmetries are being enlarged, which may cause the gasket to fail and subsequently break a diamond. Therefore, the gasket is indented before the sample hole is drilled to reduce its thickness and to provide additional support for the diamond anvils. Upon pre-indention by squeezing the gasket between diamond anvils the individual culet-form is pressed into the metal as shown in Figure 4.24. Additionally, decreasing the sample hole-diameter extends the stable regime and the pressure can be increased further.

Pressure Calibration

In-situ pressure calibration is performed by means of the Ruby fluorescence method. The red shift of the fluorescence from a Ruby crystal is known and by measuring the R1-emission line-shift, the pressure in the DAC can be determined. We used a formula by Mao et al. [54], initially found by Piermarini et al.:

$$P = \frac{A}{B}[(1 + \frac{\lambda - \lambda_0}{\lambda_0})^B - 1] \tag{4.1}$$

With the R1 line at atmospheric pressure: λ_0=694.14 nm; constants A=19.04$\cdot 10^3$ kbar and B=7.665. The formula yields approximately a straight line and is valid up to 800 kbar.

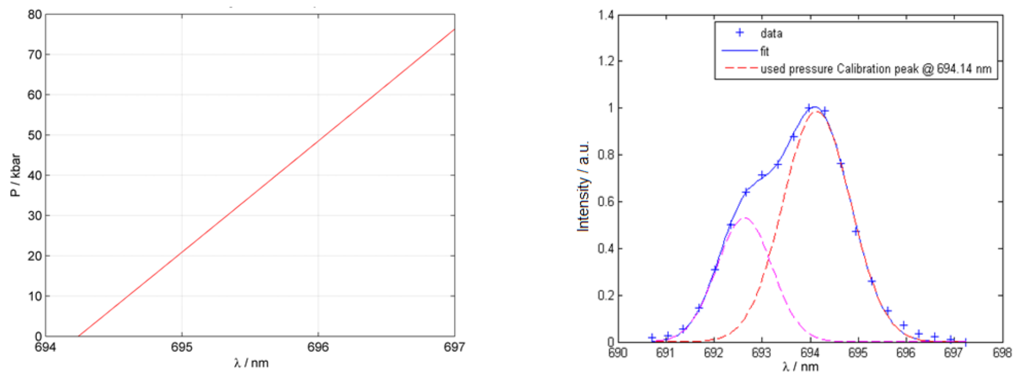

(a) (b)

Figure 4.25: (a) Peak-shift of the fluorescence R_1 line emitted by a Ruby crystal; (b) R_1 and R_2 emission recorded during a high pressure measurement in the DAC and fitted to a sum of two Gaussians.

Figure 4.25 (a) shows an evaluation of Equation 4.1 for the peak-shift of the Ruby R1 line within the accessible pressure range in our experiments. One notes the rather small shift (less than 3 nm up to 70 kbar) compared to the width of a Rubicene crystal's emission spectrum. Figure 4.25 (b) shows the emission R_1 and R_2 lines recorded during a high-pressure measurement. Both lines were fit to a sum of two Gaussians with a fixed distance in order to increase the resolution of the peak-position. The resolution of our CCD-spectrometer with a 600 1/mm grating was 0.3 nm, corresponding to an uncertainty of 8 kbar which was improved to about 5 kbar by fitting.

Pressure Transmitting Medium

Maintaining hydrostatic conditions in the DAC relies on the pressure transmitting medium. Upon application of pressure in the DAC different media remain hydrostatic up to distinctive maximum pressure values. Placing tiny Ruby chips at various places within the DAC and observing the lineshape at increasingly higher pressures is a method for testing the occurrence of non-hydrostatic effects. A pressure gradient is accompanied by broadening the emission lines and an increased distance of the Ruby emission lines (R_1 and R_2). Klotz et al. determined the hydrostatic limits of various pressure transmitting media by means of this method [55] and found for methanol:ethanol (4:1) a limit of 10.5GPa, while Silicon oil stays hydrostatic at least up to 12 GPa. Higher pressures can be obtained by loading the DAC, e.g. with He, which remains hydrostatic up to at least 23 GPa. Non-hydrostatic effects in water are not observed until 5 GPa [56].

Loading

The sample needs to fit into the gasket hole, and should not be in direct contact with the walls of the sample compartment. Otherwise, due to the deformation of the sample chamber the sample will be wedged, thus, inducing an unintended pressure gradient.

In order to place both, sample and Ruby crystal into the sample chamber a self-made instrument was used, ie. an eyelash glued to the tip of a toothpick and a small needle. Methanol:ethanol in a 4:1 ratio was loaded by drop casting and the cell was closed immediately afterwards to keep the volatile medium in the gasket.

Experimental Setup

A self-designed setup was built for high pressure Photoluminescence experiments with a Rubicene single crystal. The schematic view and a picture of the setup are shown in Figure 4.26. The DAC is mounted on an aluminium stage with a hole in its center to make the diamond windows accessible from both sides of the cell. Below the stage is a small incandescent light bulb shining light through both diamonds and the sample chamber. The beam of a diode laser (532 nm and 4.75 mW) is shined on the lower diamond and excites the Rubicene crystal. The light, either emitted by the crystal or transmitted through it, is then collected by an optical fiber that passes the light further into a CCD spectrometer (type: MS125, grating: 600 l/mm, λ_{blaze}=400 nm). During all measurements the CCD-chip of the spectrometer was cooled to −25 °C and an intensity calibration was performed by using the emission from an Osram WI 17/G tungsten-ribbon lamp.

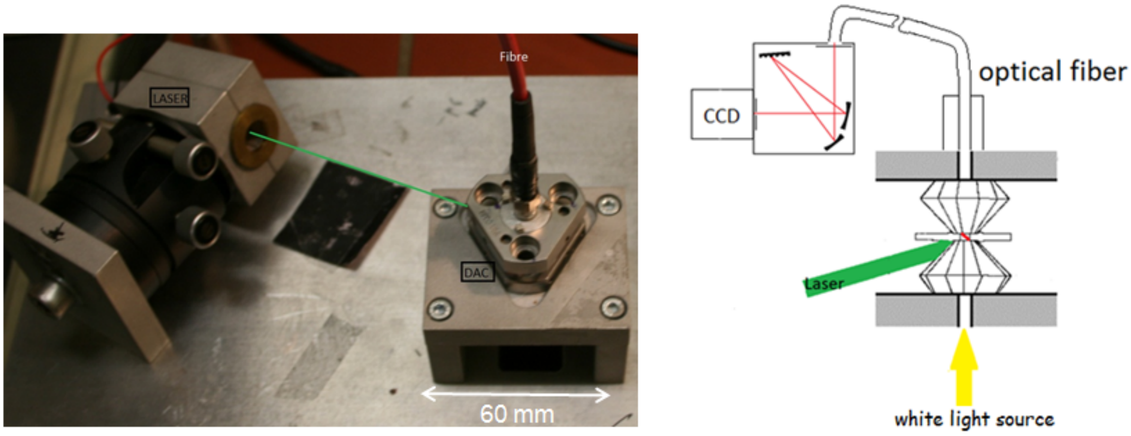

Figure 4.26: Setup for detection of emission from Rubicene crystals and transmission through the crystals. Right: Schematic view; Left: Picture of the realization with 532 nm diode laser and CCD spectrometer MS125.

The pressure was increased by tightening allen cap screws, that press the upper and the lower part of the DAC together. We waited one minute for the sample to equilibrate prior to each measurement. The stability of the conditions within the cell was tested by keeping it at a constant pressure for one hour and measuring the Ruby spectrum every 15 minutes, yielding no significant decrease in pressure.

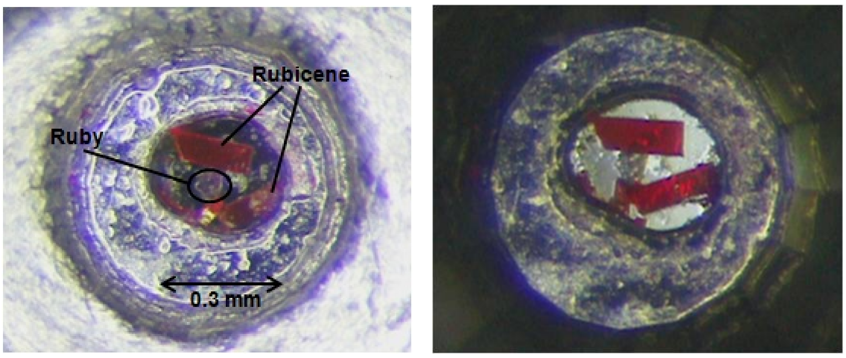

(a) Atmospheric pressure (b) 6 kbar

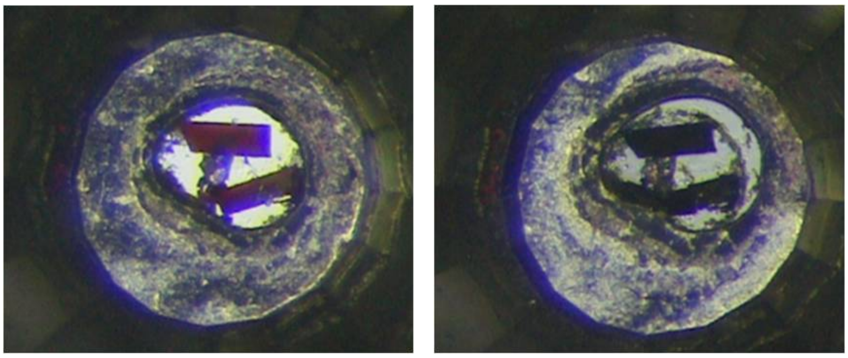

(c) 14 kbar (d) 46 kbar

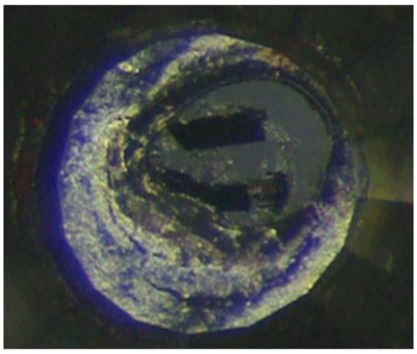

(e) 46 kbar

Figure 4.27: Pictures of Rubicene crystals in DAC taken at white LED illumination from above in binocular. (b) - (e) were taken through the upper diamond window with additional light from below while (a) is a picture of the open cell prior to the experiment at atmospheric pressure. Uncertainty: $\Delta \mathrm{p} = 5\,\mathrm{kbar}$.

4.4.2 Measurement Results

Measurements of the emission from a Rubicene single-crystal as well as of the transmission through the crystal were performed in the explained setup. After loading the cell, the pressure was increased up to the point, where a significant expansion of the sample hole started to occur.

Figure 4.27 shows a series of pictures taken through the upper diamond window in a binocular; Ruby and Rubicene crystals are indicated in the first picture of the open cell. The stated pressure values are meant to be applied additionally to atmospheric pressure.

The width of the sample-hole was initially about 0.3 mm, as indicated in picture (a). As the pressure was increased the hole was deformed and started to expand drastically above 40 kbar. At 46 kbar the experiment was aborted because the initial asymmetry was enhanced and the gasket-edge threatened to disappear in the upper right of picture (e).

Looking at the Rubicene crystal as the pressure is being increased, one notes a change of color, from strong red fluorescent at atmospheric pressure to a deeper red, but less intense color at 6 kbar and at pressure values exceeding 14 kbar the crystal exhibits neither fluorescence nor transmittance of visible light.

Emission

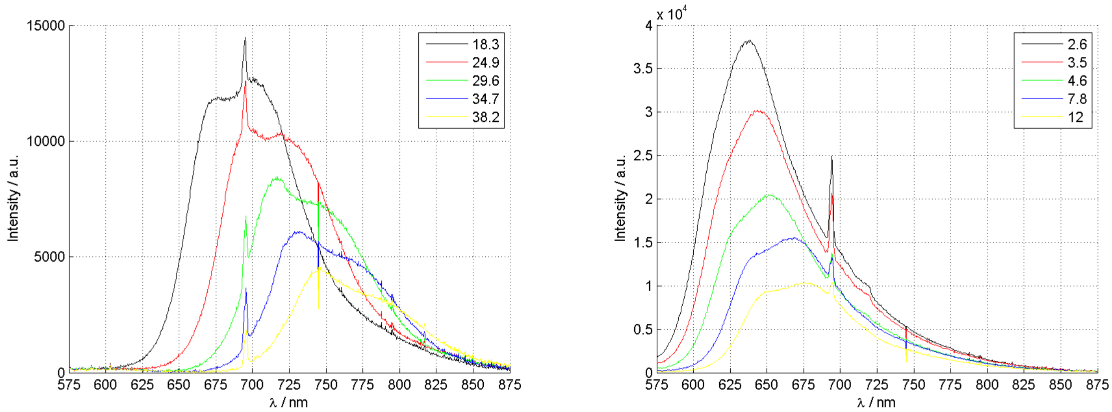

Figure 4.28: Emission spectra of Rubicene crystal and Ruby crystal in DAC at various, increasing pressure values. Values in the legend denote applied pressure p in kbar, Δp=5 kbar; Intensity correction performed.

Fluorescence spectra from Rubicene in the DAC at increasingly higher pressures are shown in Figure 4.28. For this measurement series a smaller fraction of Ruby was used in order to yield only a small part of Ruby-emission, superimposed on the Rubicene crystal's spectrum. Otherwise, a large Ruby peak induces additional uncertainty in the determination of the Rubicene's transition position via the Gaussian peak-fit method. In Figure 4.28 a large red-shift of the crystal's fluorescence is observed as well as a pronounced intensity decrease. The intensity decrease is additionally enhanced by a change in measurement geometry when the diamonds squeeze the crystals, which is also supported by the declining Ruby-peak at 694 nm. However, due to the extend of the intensity decay and since it was observed in several measurement series we consider the intensity decrease to be a consequence of pressure application on the Rubicene crystals. The change of shape of the emission is caused by self-absorption processes, resulting from the compression of the sample chamber as the pressure is being increased.

Several series of high-pressure fluorescence experiments have been performed with different Rubicene crystals yielding a red-shift and an intensity-decrease. Apart from measurements at increasing pressure levels, the fluorescence emission was recorded as the pressure was decreased from its maximum value as well. The transition-peak positions, measured as the pressure is increased, coincide with the transition-peak positions as the pressure is being decreased and hence no irreversible change was induced in the Rubicene crystals.

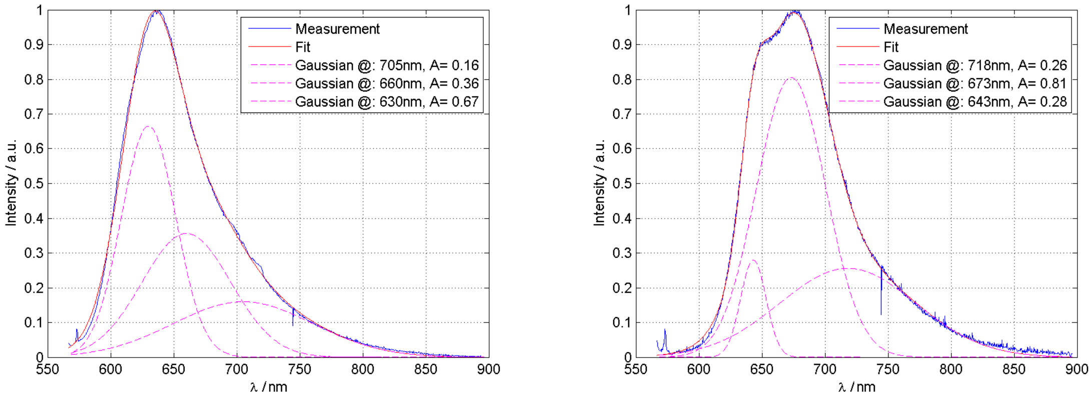

(a) 3 kbar

(b) 12 kbar

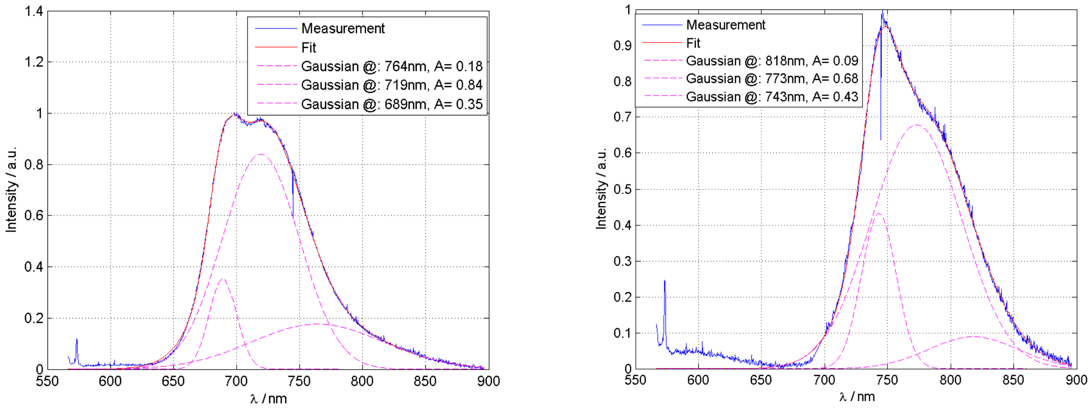

(c) 25 kbar

(d) 37 kbar

Figure 4.29: Normalized Rubicene crystal emission in DAC for various pressures; Fit of data to a sum of three Gaussians with the depicted positions in the legends. The distance between peaks are fixed throughout all pressures. Data points in the vicinity of 3 nm around the Ruby emission-peak have been ignored in the fit-algorithm and consequently are not plotted.

The red-shift of the crystal's emission was quantified by fitting it to a sum of three Gaussians as described in Section 4.1.2. Figure 4.29 shows emission spectra and fit results for various representative pressure values. Distances, in terms of wavelengths, between the three Gaussians are set to a fixed value, since additional fitting with variation of all three peak positions individually, implied that the emission structure does not change significantly. Fixed peak-distances within the fit algorithm yielded more reliable peak positions for emission data at all pressures. A variation in the shape is explained by a change of peak amplitudes and further the appearance of different emission spectra-shapes are consequences of self-absorption effects, as previously mentioned.

Figure 4.30 shows a plot of the FWHMs, determined from Gaussian peak fits, in dependence of applied pressure. The first two transitions (red and green) show a slightly increasing width with pressure. The width of the broad peak at longer λ (blue) is constant up to 25 kbar, while above 25 kbar a part of this transition is shifted to wavelengths exceeding the adjusted measurement range of the CCD spectrometer. Additionally, the emission intensity at high-pressure levels is low, hence the peak fit is hard to accomplish and causes the deviations above 25 kbar. This additional uncertainty of the blue peak (highest λ) was also a reason for using constant peak distances in the fit-algorithm.

Comparing the normalized emission spectra in Figure 4.28 visualizes, that the overall width of the Rubicene crystal's emission stays constant, signaling hydrostatic conditions in the cell.

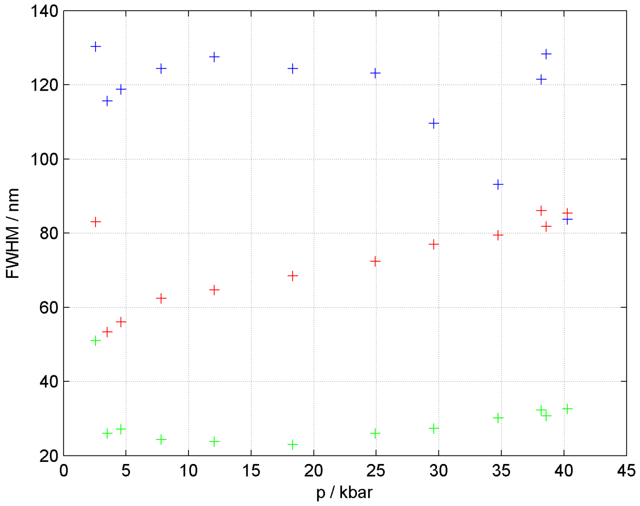

Figure 4.30: Full width at half maximum of Gaussians fitted to the Rubicene crystal's emission spectrum with respect to applied pressure in DAC. FWHM of lowest wavelength Gaussian: green , Second Gaussian: red , highest wavelength Gaussian: blue.

Results for the fitted peak-positions are plotted in dependence of applied pressure in Figure 4.31. Overall, the emission wavelengths shift by 120 nm, or converted to an energy scale a shift of 0.3 eV to 0.4 eV is observed. Straight lines describe the data sufficiently and linear fitting yields slopes of 7.5 meV/kbar, 8 meV/kbar and 9 meV/kbar for the first, second and third peak, respectively.

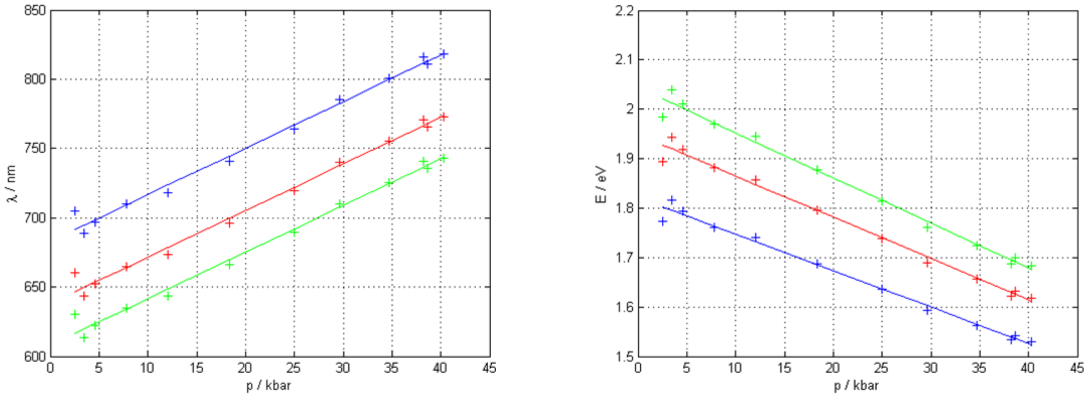

(a)

(b)

Figure 4.31: Fit of straight lines to the peak positions in dependence of applied pressure. (a) illustrates the peak positions on a wavelength scale, while (b) is on an energy scale. Slopes of fitted lines: k_1=-7.5 meV/ kbar, k_2=-8 meV/ kbar, k_3=-9 meV/ kbar.

Absorption

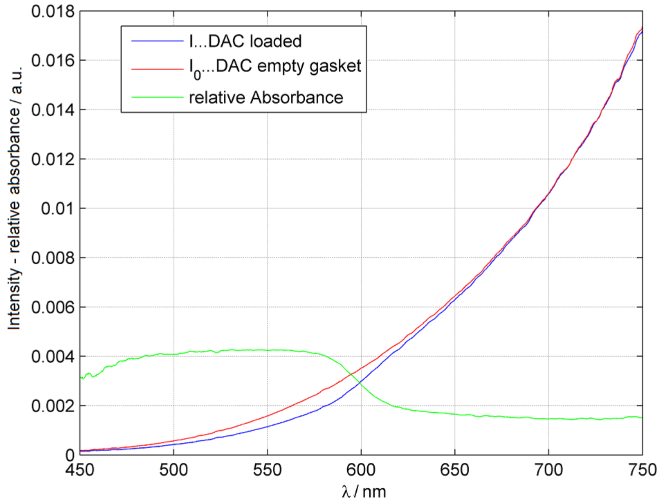

Figure 4.32: Transmitted intensities through DAC with empty gasket I_0 and loaded DAC I, while no pressure was applied. Relative absorbance, scaled by factor of 1/50 for comparison with the intensities.

Relative absorbance spectra were obtained by measuring the transmitted intensity of a small light bulb through the diamond cell with Rubicene crystals (I) and with an empty gasket (I_0). The absorbance a is then calculated as a=-log($\frac{I}{I_0}$). The spectra were recorded within the same setup as used for the emission measurements and at the same pressure levels by using a second spectrometer (Ocean Optics, 600 l/ mm). Depicted in Figure 4.32 is the transmitted intensity

(I) for one specific pressure as well as the reference intensity (I_0) and the relative absorbance scaled by a factor of 1/50 to compare it with the intensities.

The fraction of light absorbed by the Rubicene crystal is small compared to the transmitted intensity of the bulb, since the diamond windows are not fully covered by the crystals. Nevertheless, a sufficiently high fraction of the light intensity was absorbed for determining the position of the absorption edge.

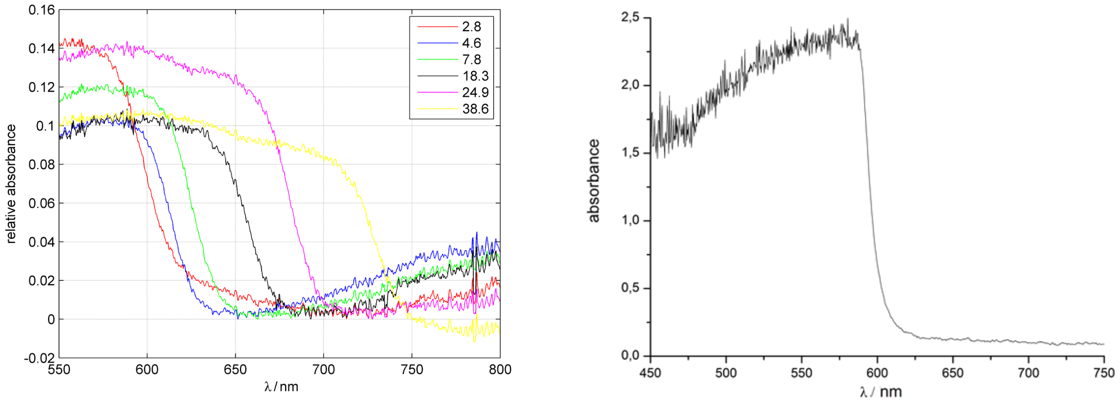

(a)

(b)

Figure 4.33: (a) High pressure measurement of relative absorbance of Rubicene crystals in DAC, pressures in kbar.(b) is the transmission through a Rubicene crystal in atmospheric conditions for comparison from [19].

Figure 4.33 (a) shows relative absorbance measurements for various pressure values, compared to the absorbance of a Rubicene crystal, measured under atmospheric conditions. One notes a red-shift of the absorption edge as the pressure is being increased similar to the effect observed in fluorescence measurements. The absorption edge at zero applied pressure is located at about 600 nm corresponding to a bandgap of 2.07 eV. In order to quantify the red-shift, the absorption edge was plotted in Figure 4.34. A substantial red-shift from 600 nm to about 730 nm was observed, that is 130 nm or 0.3 eV. A fit of a straight line yields a slope of 8 meV /kbar, thus being in good agreement with the fluorescence emission red-shift observed at high pressure. The maximum values of absorbances are not compared because the sample-chamber is being deformed as the pressure increases thus imposing a decrease of absorbance.

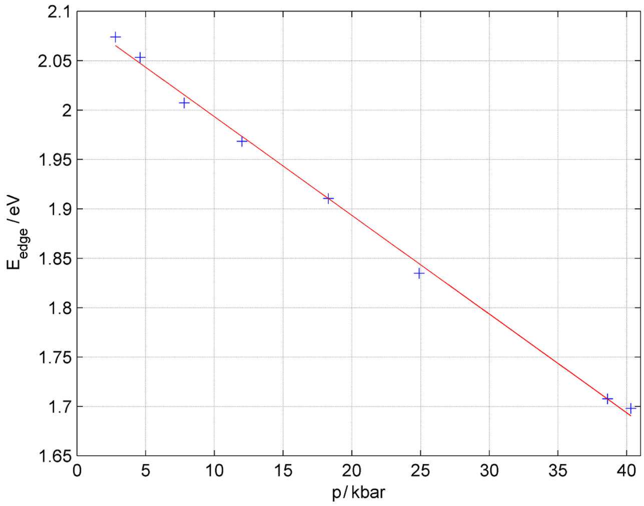

Figure 4.34: Absorption-edge positions of a Rubicene crystal with respect to applied pressure in DAC. Fit of straight line in red with slope of k=-10 meV/ kbar.

4.4.3 Discussion

We attempt an interpretation of the Photoluminescence red-shift in Rubicene crystals at high pressures. As the pressure is increased, the intermolecular distances decrease since the Van der Waals forces between individual molecules are much weaker (10-100 meV) than the covalent bonds within the molecules ($\approx$ eV). As the molecules move further together the overlap of the excitonic wave-functions gets larger, which results in a higher degree of delocalization. This is similar to Section 2.1, where we outlined, that a higher conjugation length in oligo-acenes yields a decrease of the bandgap, while the increase of exciton-delocalization upon application of high pressures yields a smaller bandgap and a larger bandwidth. Higher delocalization of excitons is accompanied by less exciton binding energy (EBE). Less EBE is, in turn, equivalent to a higher energetic distance between the exciton levels, but overall the bandgap decrease outweighs the increase of EBE, hence the transition $S_0 \rightarrow S_1$ shifts to lower energies.

Comparing the emission- and absorption-shift supports the reasoning above. The shift of the absorption edge corresponds to a shift of the bandgap while the energetic shift of the first emission maximum (the $S_1 \rightarrow S_0$-transition) corresponds to the shift of excitonic levels, thus including a decrease of the EBE. Therefore a larger red-shift of the absorption is expected. Indeed, the measured red-shift of absorbance (10 meV /kbar) is larger than the red-shift of the first emission maximum (9 meV /kbar) but only by 1 meV /kbar, which can also be due to uncertainty.

Another observed effect, the intensity-decay can be explained by means of a higher degree of exciton-delocalization. The reduction of the EBE is accompanied by an increase of the electron-hole distances within the semiconductor which, in turn, results in a reduced probability for Singlet recombination. Hence, the quantum yield declines yielding less emission intensity at constant excitation intensity.

Our reasoning is motivated by theoretical calculations of high pressure luminescence properties conducted by Puschnig et. al. [21]. They find, by solving the Bethe-Salpeter equation, a decrease of the excitonic binding energy and a decrease of the energetic position of the imaginary part of the dielectric function (equivalent to the absorption) by variation of pressure from 0 GPa to 10 GPa.

Our results are in good agreement with high pressure measurements of Tetracene and Anthracene crystals. As previously mentioned these two oligo-acenes have similar structural properties, since the core of Rubicene is basically an Anthracene molecule with two phenyls attached on the side via a 5-membered ring; Tetracene has one more phenylring and all three organic semiconductors are planar. The molecules crystallize in Herringbone structures, Anthracene and Rubicene with monoclinic unit cells, while the unit cell of Tetracene is triclinic [57].

Dreger et al. conducted high pressure luminescence experiments on Anthracene up to 8 kbar and found an emission red-shift of 0.5 eV or 6.25 meV/kbar [56]. Additionally they reasoned, that among the effects occurring due to non-hydrostacity is also an extensive broadening of vibrational peaks. In our measurements a weak broadening appeared, which could be due to small deviations from hydrostacity throughout the sample compartment.

Tetracene single-crystals under pressures up to 37 kbar have been investigated by Mizuno et al. [58] who found a red-shift of 0.37 eV or 12.3 eV/kbar. However, they did not observe a linear pressure shift, since at approximately 10 kbar a discontinuity appeared, which they assigned to be caused by a phase transition. One notices, that the red-shift of Rubicene is in between the values for Tetracene and Anthracene and no discontinuity appears in the data, hence a phase transition caused by high-pressure up to 4 kbar is unlikely.

5 Single Crystal Laser

This section is denoted to the construction of an organic optically pumped laser with Rubicene single crystals. Rubicene crystals are birefringent with refractive indices of $n_\perp = 1.84$ and $n_\parallel = 2.95$ for vertical and parallel polarized light respectively, with respect to the long crystal axis. Hence, Equation 2.22 yields surface reflectivities of R= 9% and 24%. Plane parallel resonators are built by transferring DBRs to the surfaces of the single crystals in order to enhance the surface reflectivities for building a single crystal resonator.

5.1 DBR

Properties of dielectric mirrors can be adjusted by choosing suitable materials and layer properties, ie. refractive indices, layer thickness and number of layers. A large difference of refractive indices between subsequent layers is desirable since it yields high reflectivities at each interface and subsequently the maximum value of reflectance is high. Once suitable materials are chosen, increasing the number of bi-layers also increases the reflectance and yields sharper edges of the reflectance band around the wavelength of peak-reflectance λ, as described in Section 2.9.

For building a single-crystal resonator we used two different types of DBRs, made of seven, respectively eleven, alternating layers of ZnS ($n_H = 2.32$) and MgF_2 ($n_L = 1.38$) with ZnS as the first and as the last layer.

A novel technique was used to coat Rubicene single crystals with dielectric mirrors: First dielectric layers were thermally evaporated on a NaCl-single crystal substrate ([100] surface) to build a DBR as depicted in Figure 5.1. The NaCl crystal together with the DBR was split, a fraction was placed in water and the mirror detaches from the NaCl substrate. Subsequently the DBR can be caught by a glass substrate or by a Rubicene crystal. This technique avoids the exposure of the organic crystal to high temperatures, occurring during the process of thermal evaporation.

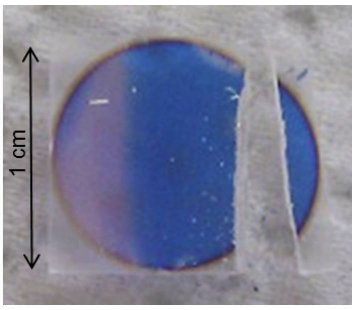

Figure 5.1: Splitted DBR on NaCl-single crystal substrate.

Transmission spectra were recorded on a Shimadzu UV1800 for both series of DBRs on NaCl, shown in Figure 5.2 (a). The transmission maxima are at around 50-60% because the spectra were not corrected for light scattering by the NaCl substrate and one can assume a constant scaling factor to correct for scattering. Clearly, the 11-layer DBR shows a significantly lower transmission minimum (below 2%) than the 7-layer DBR (below 3%). The emission spectrum

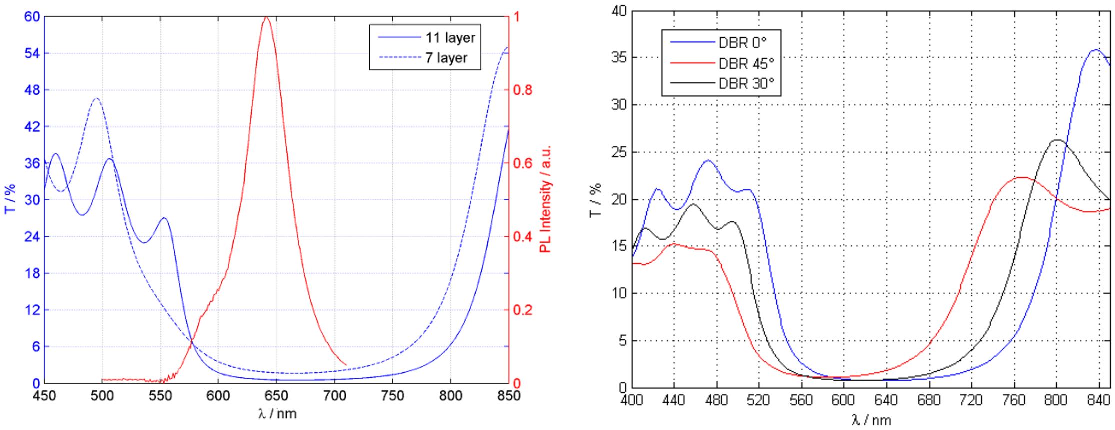

(a)

(b)

Figure 5.2: (a) Transmission spectra measured for two DBRs on NaCl with 7 and 11 layers compared to the Rubicene crystal's emission. (b) Shift of reflectance band with increasing incident angle of light.

of a Rubicene crystal is shown in Figure 5.2 (a) for comparison to the reflectance band of our DBRs. The crystal's emissive transitions are located within the high reflectance band in order to give rise to resonance between the crystal surfaces.

The excitation-laser beam needs to be transmitted through the DBRs to reach the Rubicene. Therefore, the reflectance band should start at wavelengths higher than the excitation (λ_{Ex} = 532 nm) which is better satisfied for the 11-layer DBR than for the 7-layer DBR. For light that is directed onto the DBR with a non-zero incident angle, the reflectance band shifts to lower λ compared to light with perpendicular incidence. Figure 5.2 (b) shows a transmission spectrum of a 7-layer DBR for increasing angles of incidence, recorded with a Perkin Elmer λ9 spectrometer. The reflectance band shifts about 40 nm, for an incident angle of 45°.

Transmission or reflectance spectra with Rubicene as the incident medium provide information to quantify the influence of an additional interface between crystal and DBR and to study the behavior for light within the cavity, that is not perpendicularly reflected by the DBRs. We used a MATLAB-package to simulate the reflectance spectra, rather than performing measurements. The software from Sophocles uses the transfer matrix method and is described in detail in [59].

In Figure 5.3 one notes the large blue-shift occurring in the reflectance band when the light beam passes through Rubicene before being reflected at a certain angle from the DBR. Results from three simulations are shown with air and Rubicene as the incident media, whereas for Rubicene results for two refractive indices are shown, one for the perpendicular polarization direction and one for parallel polarization. Comparing the figures for Rubicene ($n_{\perp}$=1.84) and air shows that the reflectance spectrum behaves similarly but with an enhanced dependence on the incident angle for Rubicene. At about 65 ° in air the reflectance band has shifted to the same wavelengths as at an indent angle of 30 ° in Rubicene. In contrast, for Rubicene with parallel polarization ($n_{\|}$=2.95) the shift is drastically enhanced and at an incident angle exceeding 30 ° light gets reflected in the whole visible region. The difference of the refractive index between the first medium (Rubicene or air) and the first DBR-layer made of ZnS (n=2.32) is the reason for the observed shift of the reflectance band. According to Snells law the angle α of a light ray incident on an interface between two media changes from α in the first medium to β in the second medium: $n_1\, sin(\alpha) = n_2\, sin(\beta)$. Therefore, taking air as the first medium and Rubicene ($n_\perp$=1.84) as the second medium the incident angle in air: α= 30 ° yields an angle of β = 66 ° in Rubicene, thus explaining the enhanced angular dependence when changing the incident medium from air to Rubicene in Figure 5.3.

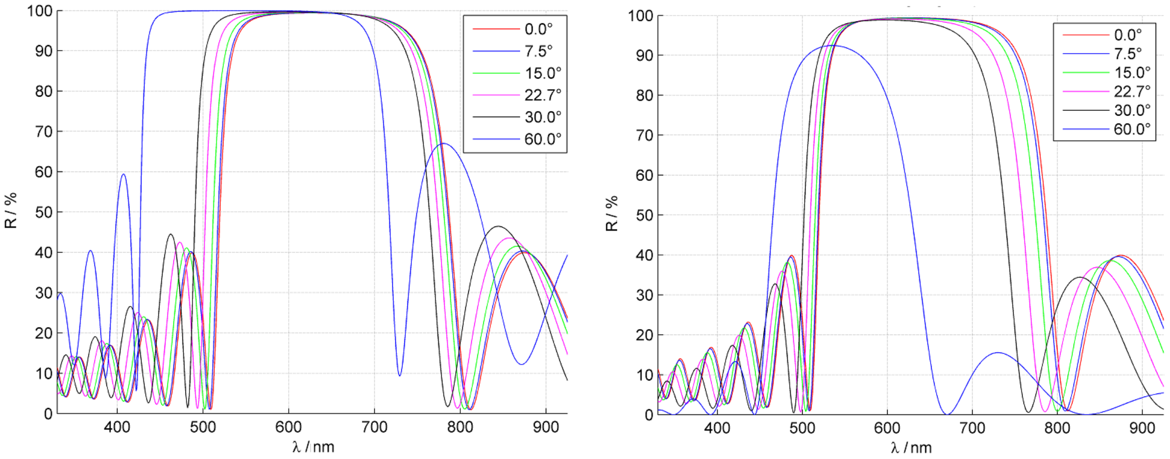

(a) air, TE

(b) air, TM

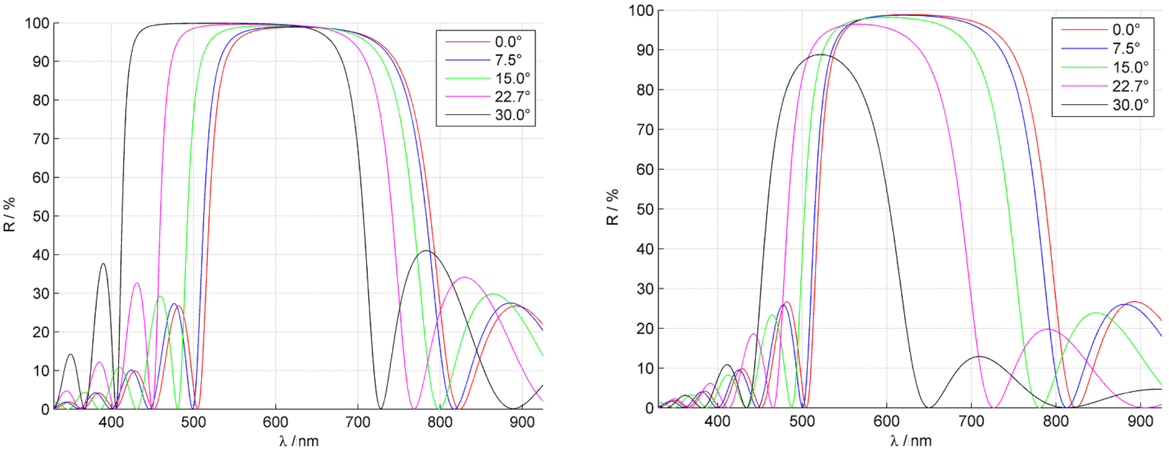

(c) Rubicene (n=1.84), TE

(d) Rubicene (n=1.84), TM

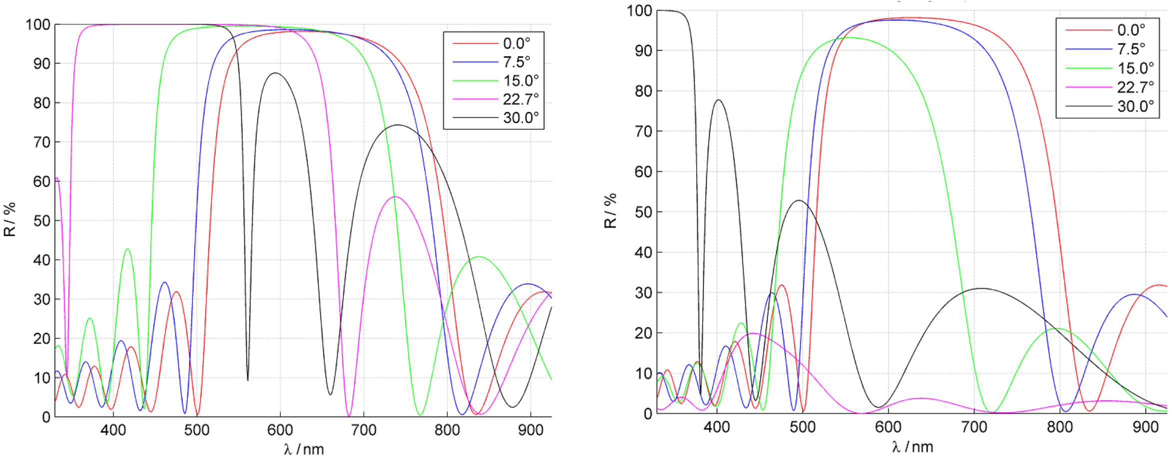

(e) Rubicene (n=2.95), TE

(f) Rubicene (n=2.95), TM

Figure 5.3: Simulated reflectance of a DBR for peak-reflectance at λ=626 nm, consisting of 11 layers ZnS and MgF_2 for various angles of incidence. (a) & (b): The light beam passes the interface to DBR from air (n≈1), from Rubicene ($n_\perp$=1.84): (c) & (d) or from Rubicene ($n_\parallel$=2.95): (e) & (f). Reflectance spectra on the right (a,c,e) are for transverse electric (TE) polarization; depicted on the left (b,d,f) are the reflectance spectra for transverse magnetic (TM) polarization.

5.2 Single Crystal Resonator

The quality factor is a suitable measure to quantify the quality of an optical cavity as described in Section 2.8. Prior to the calculation of the Q-factor, the reflectance of the DBR needs to be determined. The reflectance of a DBR, attached to a Rubicene crystal, where the light ray is incident on the crystal is smaller than the reflectance of the DBR by itself.

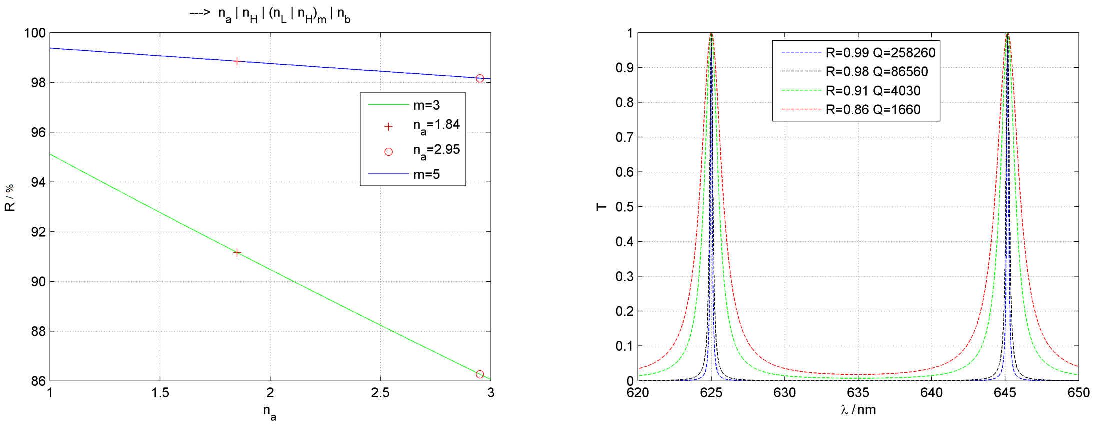

(a) (b)

Figure 5.4: (a) Simulated peak-reflectance of DBR in dependence of the refractive index n_a of the first medium, where the DBR structure is made of alternating layers of ZnS(n_H) and MgF$_2$(n_L) followed by a glass substrate (n_b), as shown schematically above the plot. Indicated with red markers are the measured Rubicene refractive indices. (b) Transmittance through plane-parallel resonators for four values of reflectance, as indicated with red markers in (a). The legend depicts the reflectances and the Q-factor for the shown wavelength region. Resonator thickness: 10 μm.

In order to estimate the influence of a Rubicene crystal instead of air as the first medium adjacent to DBR mirrors simulations of the reflectance band for a range of refractive indices n_a were performed with the same MATLAB-based algorithm as has been used in Section 5.1. Figure 5.4 (a) shows the values of peak reflectance for the simulated reflectance band in dependence of n_a, where the two measured values for both polarization directions in Rubicene are depicted with red markers. As the refractive index of the first medium increases from $n \approx 1$ for air, the overall reflectance decreases linear. This behavior is also explained by Equation 2.22 that predicts a decrease of reflectance from an interface between two dielectric layers when the difference of the refractive index between both layers decreases. The reflectance is shown in Figure 5.4 (a) for a 7-layer DBR (m=3) and for an 11-layer DBR (m=5). Apart from observing an increase in the reflectance, a declining dependence on the refractive index n_a is observed.

Figure 5.4 (b) illustrates the transmittance through a cavity for the reflectances shown in Figure 5.4 (a). The quality factor Q is calculated by Equation 2.21 and depicted in Figure 5.4 (b) for all four transmittance curves. One notes that Q is higher for light, incident with perpendicular polarization (n_a=1.84) compared to light, incident with parallel polarization with respect to the long Rubicene crystal's axes. All simulated reflectances are accompanied by high Q-factors providing sufficient feedback to enhance stimulated emission, resulting in resonance features or gain narrowing in an optically active medium.

5.3 Experimental

Single crystal resonators were built by placing a Rubicene crystal between two DBRs, where the lower DBR is on a glass substrate and the upper mirror is directly placed on top of the Rubicene crystal. The fabrication of a resonator is explained in this section, starting from DBR mirrors evaporated on NaCl-substrate, as shown in Figure 5.1.

The mirrors on NaCl-crystals are broken apart to get fragments with a few millimeter side-length, so they are better to process in the following steps and also, their sizes are on the same order of magnitude as the lengths of our Rubicene single crystals.

Then a fractioned NaCl-substrate with DBR is placed into a Petri dish, such that the DBR mirror is at the same height as the water surface and the NaCl substrate swims below it. Once the water has dissolved the connection between mirror and NaCl-crystal, the crystal sinks to the bottom of the dish and the DBR stays floating on top because of the surface tension.

A glass slide is inserted into the water below the mirror and pulled out, leaving the DBR on top of it. The lower mirror for the single crystal resonator is ready after drying for 15 minutes. Figure 5.5 shows pictures of a piece of DBR on glass substrate in reflection and in transmission. A Rubicene single crystal is placed directly onto the lower mirror so that it lies flat on it.

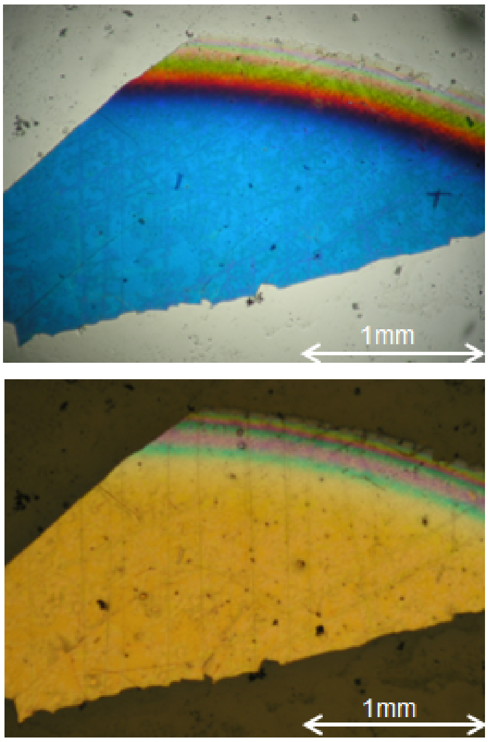

Figure 5.5: DBR mirror on glass-substrate in transmission on top and reflexion on bottom.

The upper mirror is placed on top of it by first dipping a piece of DBR on NaCl-substrate into water and then directly putting the DBR on top of the crystal, while it is still kept in place by a tweezer. After some moments (aprox. 1 min) the humidity has dissolved the connection between NaCl and DBR and the substrate can be lifted. The DBR stays then on top of the crystal and the resonator is finished.

Alternatively, a piece of the lower mirror on the glass substrate can be peeled off with a pinpoint and directly put on top of a Rubicene single crystal. In general this method yielded flat upper mirrors in contrast to the more uneven upper mirrors transferred by the first method. However, it worked only if parts of the lower mirror did not stick sufficiently to the glass substrate.

Figure 5.6 shows a single crystal resonator, recorded in our binocular and illuminated by white light LEDs. The shown resonator was constructed by placing the upper mirror directly on top of the crystal, that is using the second method, mentioned above. The upper mirror is flat on top of the crystal's surface. In contrast, fabrication by means of transferring a wet DBR onto

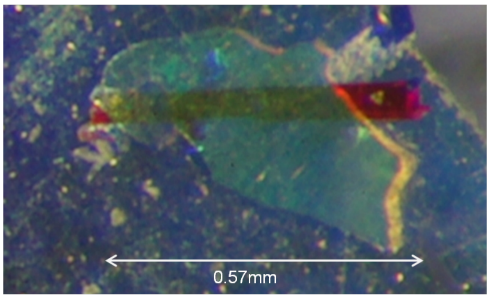

Figure 5.6: Rubicene single crystal between two 7-layer DBRs on glass substrate in binocular.

a Rubicene crystal yields a curved DBR-shape that is in not entirely flat since the wet and overhanging parts of the mirror are bent down.

5.4 Resonance

5.4.1 Measurement Geometry 1

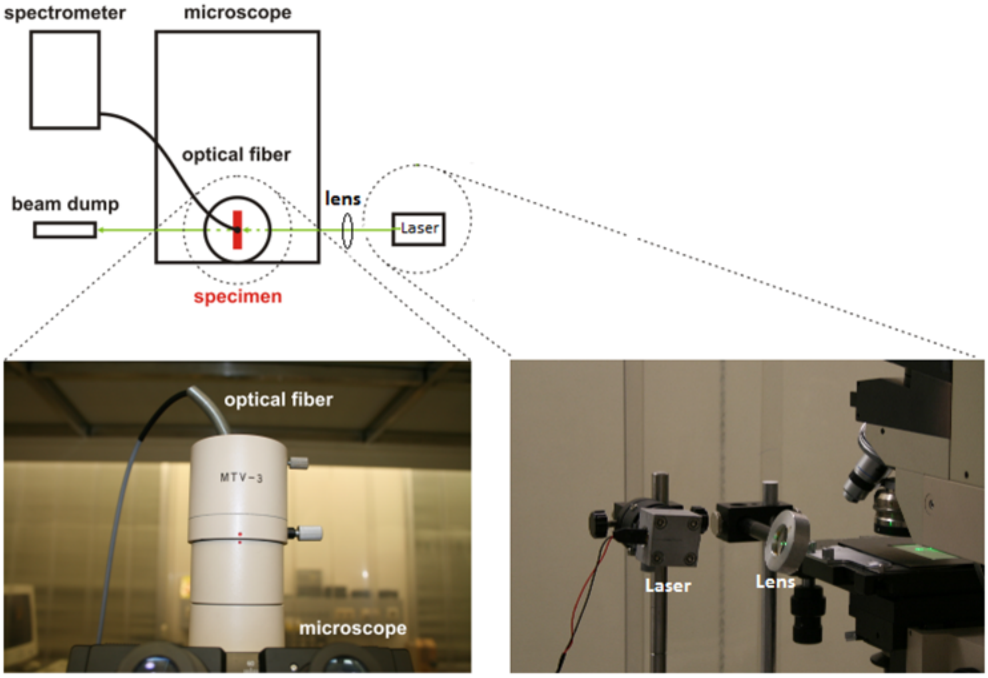

Figure 5.7: Detection setup for recording the emission spectrum from Rubicene single crystal resonators in an optical microscope, with excitation by diode laser (532 nm, 4.75mW) [19].

Single crystal resonators were illuminated by a focused cw-diode laser (532 nm) and resonance characteristics were observed, superimposed on the Rubicene crystal's emission spectrum. Figure 5.7 shows a picture of the experimental setup for detecting the resonator's emission spectra. The beam of our laser diode is focused on a part of the resonator. Light emitted from the resonator passes through the optical path in an optical microscope further into a fiber, attached to a CCD–spectrometer (Oriel MS125, 600 l/mm). Apertures in the microscope are used to measure light emitted from only a particular region of the resonator and prevent light emitted by other regions from reaching the fiber.

The first series of experiments were carried out with resonators, equipped with 7-layer DBRs while later the same experiments were repeated with 11-layer DBRs. Although the 11-layer DBRs have a higher reflectance and thus are supposed to yield a higher Q-factor of the cavity, no significant change between resonators equipped with either types of DBRs were observed. Therefore, only results obtained with 7-layer DBRs are shown in this section.

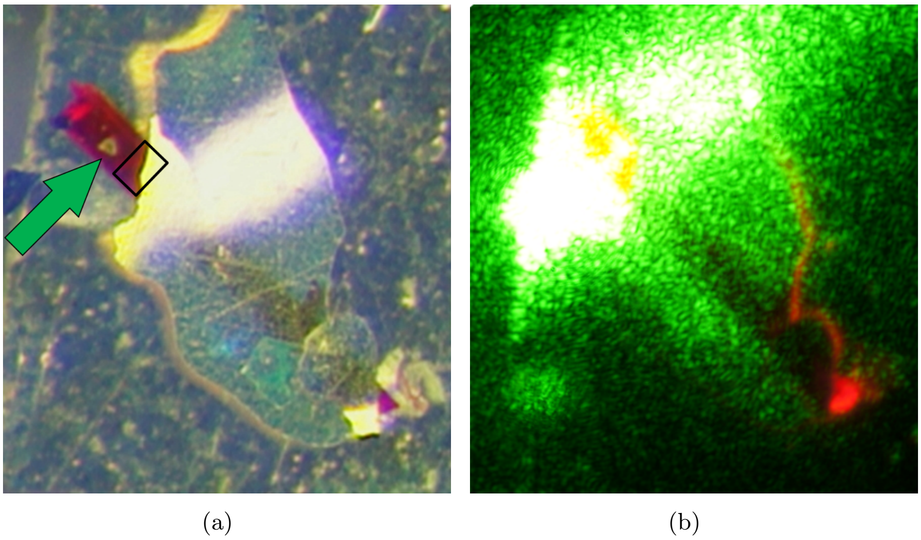
(a)

(b)

Figure 5.8: Pictures of single-crystal resonators in binocular. (a) Illumination from above with white LEDs; the green arrow indicates the incident laser beam and the rectangular indicates an area where resonance characteristics are detected. (b) Excitation with diode laser as indicated in (a).

Figure 5.8 illustrates the geometry of excitation and emission-detection within the microscope. The green arrow indicates the incident laser beam, that is focused on an uncovered part of the crystal. In contrast, when a part of the resonator covered by a DBR was illuminated a large fraction of the excitation beam was reflected due to a shift of the reflectance band to lower wavelengths, as described in Section 5.1. Figure 5.8 (b) shows a resonator in our binocular, optically excited as described above. Red luminescence from the crystal is observed, where no DBR covers the upper crystal-surface, while barely any light escapes from the covered part and no typical pattern for resonance in fabry perot interferometers is observed.

The emission spectrum of a Rubicene crystal resonator is shown in Figure 5.9. Resonance peaks are superimposed on the normal crystal's emission spectrum. These characteristics are particularly distinct around 640 nm and the distance between the peaks increases at higher wavelenghts. Resonance characteristics are observed only when the microscope's apertures are adjusted to regions of the resonator indicated in Figure 5.8 (b). Once light from another part of the crystal or a significant larger region is detected the resonance characteristics vanish and the normal emission spectrum of a Rubicene crystal can be observed.

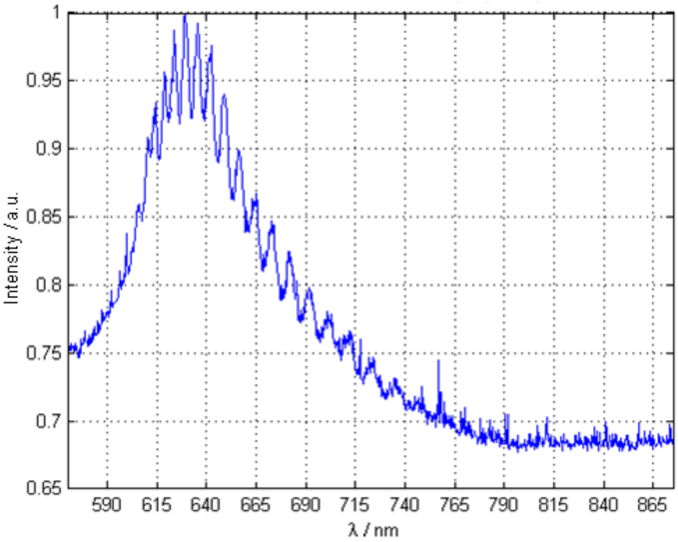

Figure 5.9: Emission spectrum of Rubicene single crystal resonator, excited with 532 nm. Detection in microscope focused on the region indicated with a black rectangular in Figure 5.8.

Discussion

Resonance characteristics in our experiments performed with four different crystal resonators could be detected with restrictions on the spatial position of excitation and detection. The excitation beam was always focused on an uncovered part of the crystal and for detection light from small regions around the edges of the upper mirrors was used while other settings did not yield a detection of resonance. We are analyzing the positions of the observed resonance characteristics (peaks) and try to find indications of their origin. The lack of self-absorption in the emission spectrum, with oscillations superimposed, speaks against resonance occurring between the DBRs however, we made observations that strongly suggest the opposite.

The resonator thickness is calculated from the distance of resonance peaks and is measured, for comparison, by the depth of focus in an optical microscope. The application of a polarization filter revealed, that resonance occurs for perpendicular polarized light with respect to the long crystal axes, only. Therefore the effective refractive index is $n = 1.84$ for resonance of light within the crystal, as measured before for light with a wavelength of 640 nm. From the peak distances in the vicinity of 640 nm a thickness of 16.2 μm is calculated. Additionally the z-axis of an optical microscope with a magnification of 200 x was calibrated by turning the z-adjustment screw a specific angle to focus on the top-surface as well as on the bottom-surface of a glass substrate. The calibration factor was calculated by dividing the actual thickness of the glass substrate, measured with a μm-screw, by the scale-parts of the z-axis adjustment screw. Subsequently the width of the Rubicene crystal resonator was measured by focusing on the upper DBR as well as on the lower mirror, yielding d=22 μm, ie. additional 6 μm compared to the value determined by the resonance peaks. Since we focused on the upper edge of the upper DBR mirror its thickness of approx. 1 μm can be subtracted. Additionally, the remaining difference can be explained by the measurement uncertainty of the thickness measured by the depth-of-focus-method, and the uncertainty regarding the determination of n.

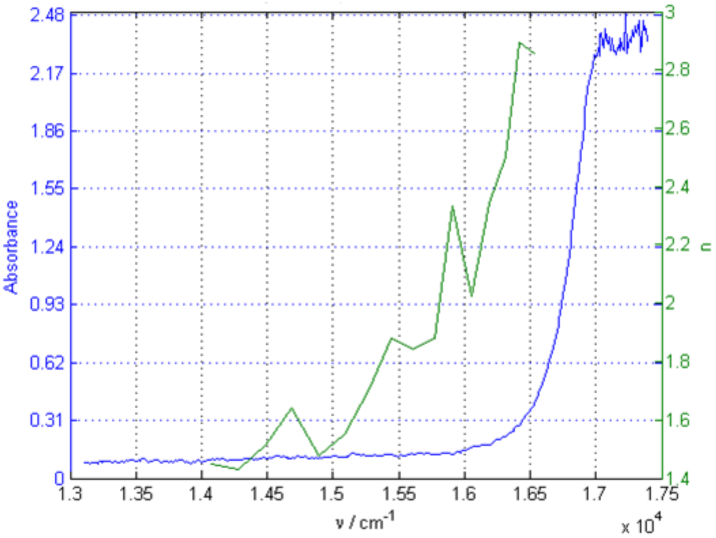

Figure 5.10: Dispersion of the refractive index n in Rubicene single crystal, calculated by the peak position of observed resonances from the resonator. Additionally, the absorbance of a Rubicene single crystal is shown.

Another observation suggesting that the oscillations arise within the Rubicene crystal is the dispersion of the refractive index. The behavior of the refractive index n in dependence of wavelength, ie. the dispersion of n, should be similar to the imaginary part of the dielectric function in the vicinity of the band edge which, in turn, has the same behavior as the absorption [60]. Again the resonance condition ($z\lambda = 2nd$) is used to calculate n for the distances between two adjacent peaks with a resonator thickness of $d = 16\mu$m. Figure 5.10 compares the values of n obtained by this method to the absorbance of a Rubicene crystal. Both curves coincide and thus the dispersion of the refractive index provides important evidence that the resonance arises within the crystal.

In conclusion, our first resonator experiments showed oscillations in the crystal's emission spectrum rather than gain narrowing, that is observed for other organic laser active materials, mentioned in Section 2.9. However, such oscillations are also observed in other crystal-resonators. Ichikawa et. al., for instance used the high reflecting surfaces of P6T crystal slaps as resonators, where oscillations as shown in Figure 5.11 are observed upon pulsed excitation . They assigned the observed resonance characteristics to be laser oscillations since they observed a clear intensity-threshold behavior at about 800 μJ/cm^{-2}.

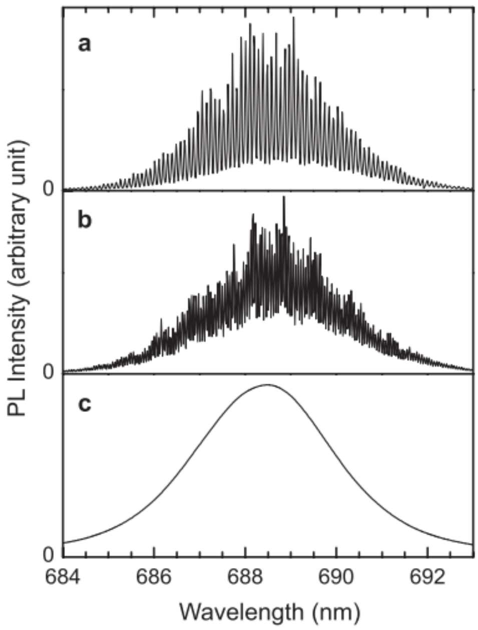

Figure 5.11: Laser-induced light emission spectra of three P6T crystals at an incident laser fluence of $1\,\mathrm{mJ/cm^{-2}}$. (a) resonator lengths: 0.560 mm, (b) resonator lengths: 1.03 mm, (c) insufficient quality of crystal faces for resonance.[34]

5.4.2 Measurement Geometry 2

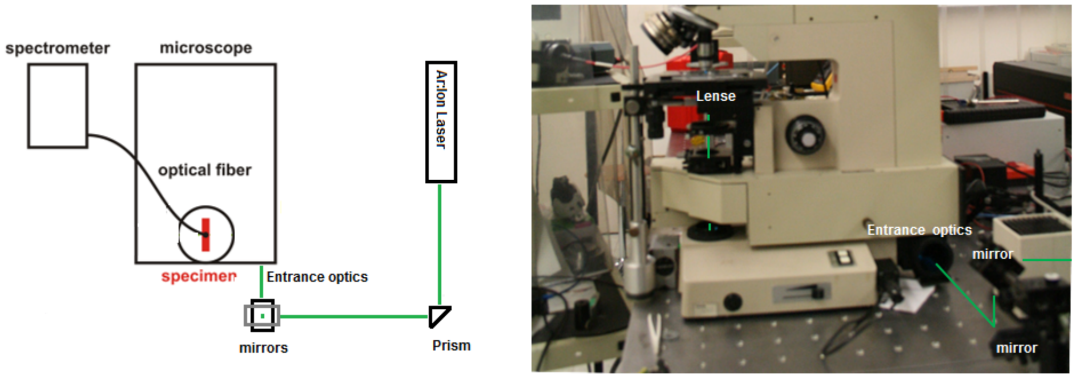

Figure 5.12: Detection setup for recording the emission spectrum from Rubicene single crystal resonators in an optical microscope, with excitation by an Ar:Ion laser (Innova 300, coherent).

We extend the series of single crystal resonator experiments by using an Ar:Ion Laser (Coherent Innova 300), with adjustable emission intensity and additional excitation wavelengths. A lower excitation wavelength is preferable since 532 nm is partly reflected by the DBR in the setup previously used, and there is a minimum angle of incidence for the laser beam due to the microscope optics (compare Figure 5.7). A different measurement geometry is used, where the excitation laser beam is focused perpendicular onto a resonator from below, as depicted in Figure 5.12. Light emission from the Rubicene crystal is detected with the CCD spectrometer passing a 530 nm cut-off filter, that is put into the optical path of the microscope to block the excitation laser beam.

The power level of the Ar:Ion laser was adjusted and the emission spectra from resonators were recorded with the CCD spectrometer. The emission spectra are depicted in Figure 5.13 (a) for various intensities of the laser and $\lambda_{Ex} = 457\,nm$. Depicted intensities are measured internally at the laser output, while the actual excitation intensity incident on the crystal is lower.

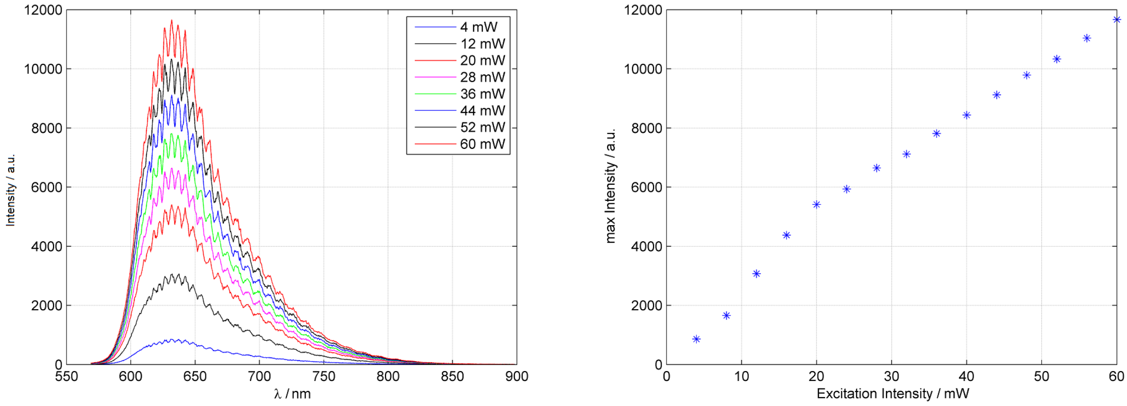

(a) (b)

Figure 5.13: (a) Emission spectra of a Rubicene crystal resonator for various excitation intensities. (b) Maximum emission intensity of crystal resonators as a function of the excitation intensity.

As the excitation intensity increases, the shape of the emission spectrum does not change at all, rather it stays completely the same. Figure 5.13 (b) shows the maximum emission intensities as a function of the excitation intensity. The intensity increases linearly with excitation power and does not show a threshold behavior as it would be expected when stimulated emission occurs.

The same calculations as in Section 5.4.1 are used to confirm the origin of the resonance to be the crystals. The Resonator thickness was calculated by using the distances of resonance characteristics around 650 nm: d = 19 μm, and the value was compared to the thickness estimated by the depth of focus in the optical microscope: d = 17 μm. The dispersion of the refractive index n shows also an identical behavior compared to the dispersion of n calculated by the resonances observed in the first resonator experiments, thus the resonance arises again within the Rubicene crystals.

In conclusion, the excitation via a laser through the lower DBR in transmission and the excitation laser coming from the side incident on the upper DBR of a Rubicene resonator showed similar resonance features. We could assign them to arise in the Rubicene crystal due to comparisons of the refractive index dispersion and absorption measurements. However, no gain narrowing or threshold behavior was observed when the excitation intensity was increased up to the level of destruction of Rubicene crystals.

Further investigations with the second setup revealed that the DBRs were not necessary to observe resonance characteristics. Rather, the surface- reflectivity of Rubicene crystals is sufficient for resonance to occur and the enhancement of the reflectivity by transferring dielectric mirrors onto the surfaces did not work appropriately.

5.4.3 Empty Resonator

Investigations in Section 5.4.1 and Section 5.4.2 revealed that the dielectric mirrors on both sides of a Rubicene crystal do not enhance the reflectivities as we expected. For a standing wave to occur in a plane-parallel resonator it is crucial to avoid any tilt between the mirrors. The width of a Rubicene crystal is small hence it is difficult to yield parallel DBRs and once a resonator was built the parallelism can not be verified, other than by the occurrence of resonance.

A simpler way to produce plane-parallel resonators is to transfer dielectric mirrors onto a glass slide (d = 150 μm), as shown in Figure 5.14 (a). The DBRs were transfered onto the glass slide with the same method as for the Rubicene crystal resonators.

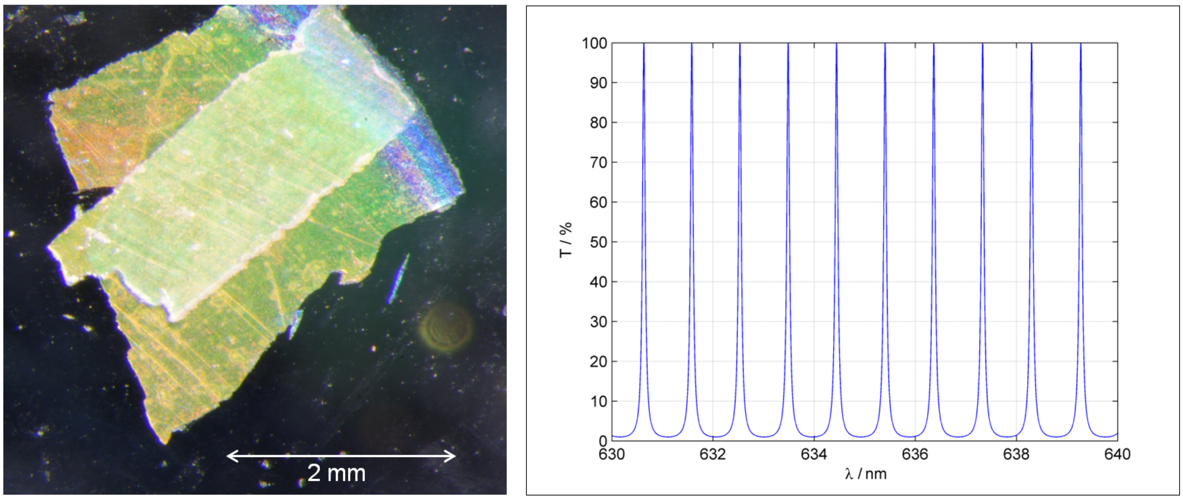

(a) (b)

Figure 5.14: (a) Glass slide with DBRs on both sides. (b) Transmission through a plane-parallel resonator with a thickness of d = 150 μm, a refractive index of $n \approx 1.5$ and a reflectivity of R = 90 %, calculated by Equation 2.19.

Upon illumination with a high pressure Xe-lamp, ie. a broad band light source, standing waves are building up between the mirrors for the resonance wavelengths. Figure 5.14 (b) shows a transmission spectrum of the glass slide resonator, calculated by the Airy formula, where the distance between transmission maxima is approximately 1 nm.

A grating with more lines than in the previous measurements with the CCD-spectrometer (2400 l/mm) was used in the setup, shown in Figure 5.12 with an Xe-lamp (100 W), to record the transmission through glass slide resonators. Figure 5.15 (a) depicts the transmitted intensity with the microscope optics, focused on an uncovered part of the glass slide. The reflectance is sufficiently high for resonance, even without mirrors on the surfaces of the glass slide. The transmission through a part of the glass slide, where both sides are coated with DBR mirrors,

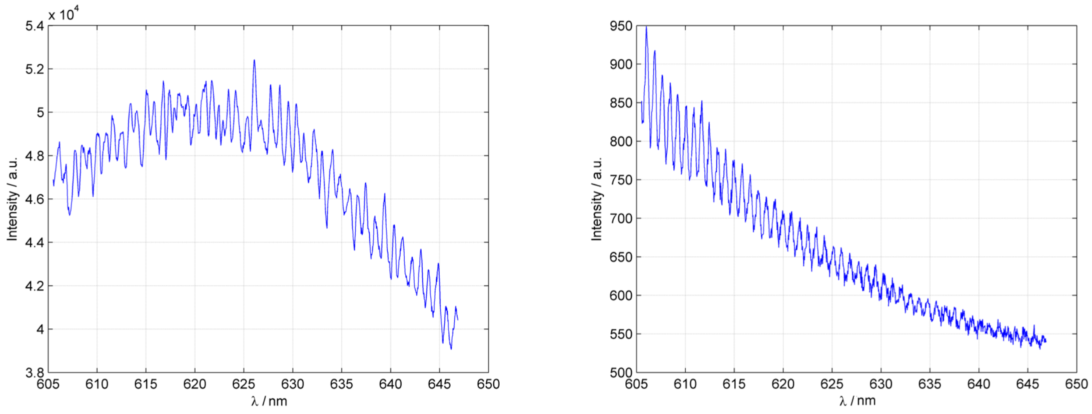

(a) (b)

Figure 5.15: Spectral transmitted part of the intensity of a Xe-lamp through (a) a glass slide and (b) a glass slide covered with DBRs on both sides.

is shown in Figure 5.15 (b). Since the free spectral range between resonance peaks does not increase significantly, the quality of the cavity is not enhanced either.

Additionally, the transmitted intensity through a Rubicene crystal was recorded under the same conditions. The spectrum, depicted in Figure 5.16 shows the resonance peaks, that arise due to reflections on the interface between Rubicene and air. The surface reflectivity is about 9 %, nevertheless, the peaks are highly developed.

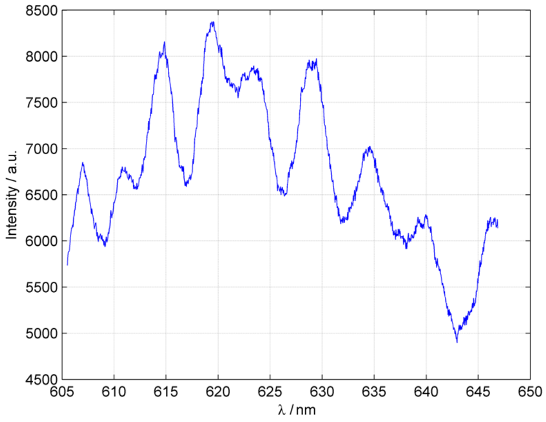

Figure 5.16: Transmitted intensity of white light from a Xe lamp through a Rubicene single crystal on a glass slide.

The measurement setup for resonance characteristics is not a problem since it worked well for the Rubicene crystal and a tilt between DBRs can be excluded in the glass slide system. We took a transmission spectrum for a single DBR, transferred to a glass slide in order to confirm, that the system of dielectric layers still has the same properties as on the NaCl-substrate. The spectrum is shown in Figure 5.17 and illustrates that the transmission for the 11-layer DBR is still below 5 % in the spectral region we are interested in.

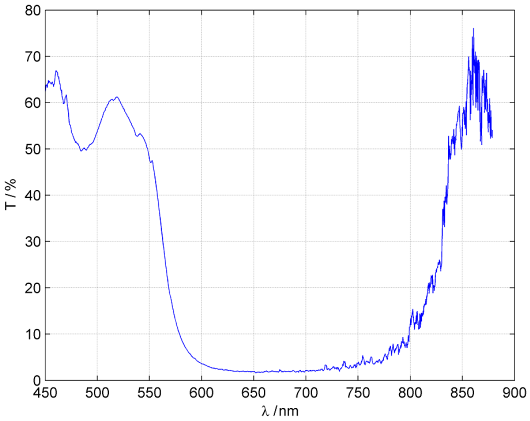

Figure 5.17: Transmitted intensity of white light from a Xe lamp through a DBR on a glass slide.

The results, thus far, show no significant change in the reflectance properties, when a dielectric mirror is transferred from NaCl- crystals to glass-substrates. In the following we discuss reasons why resonance was not observed in a plane-parallel cavity with our DBRs. Figure 5.18 shows a DBR on a glass slide in an optical microscope illuminated in transmission and in reflection respectively. There are some cracks and defects in the surface, that appear during the transfer process and additional stains are visible on the surface. Due to these surface irregularities a standing wave can not build up between two DBRs and hence the feedback in Rubicene-single crystal resonators was not sufficient to obtain a significant contribution of stimulated emission to the spectrum.

The contact between DBRs and the surfaces of the medium between them can not be established satisfyingly homogeneous. Gaps between medium and DBR change the length of the resonator locally, hence, the resonance wavelengths are changed too in this regions.

In addition, the coherence length of the light we used to observe resonance characteristics in our plane-parallel cavities is a crucial parameter. White light sources have coherence lengths in the range of 1 μm, as mentioned in [61] and in Table 2.1. The glass slide system has a resonator length of $d = 150\,\mu$m while the width of Rubicene crystals is $d \approx 20\,\mu$m. The transmission experiments did not yield the expected enhancement of resonance characteristics between DBR mirrors because the coherence length of the used Xe-arc lamp is much shorter than the resonator lengths. The resonance peaks we observed with the Rubicene crystal, shown in Figure 5.16 are much more pronounced than the peaks observed with the glass slide system, Figure 5.15. Since the resonance length of the crystal is about ten times smaller than the width of the glass slide, this observation confirms our theory of insufficient coherence length.

The coherence length of the Rubicene crystal's luminescence is unknown. However, the broad spectral width of the luminescence and similar resonance characteristics compared to our experiments in transmission of white light suggest that it might about μm. For this reason a clear

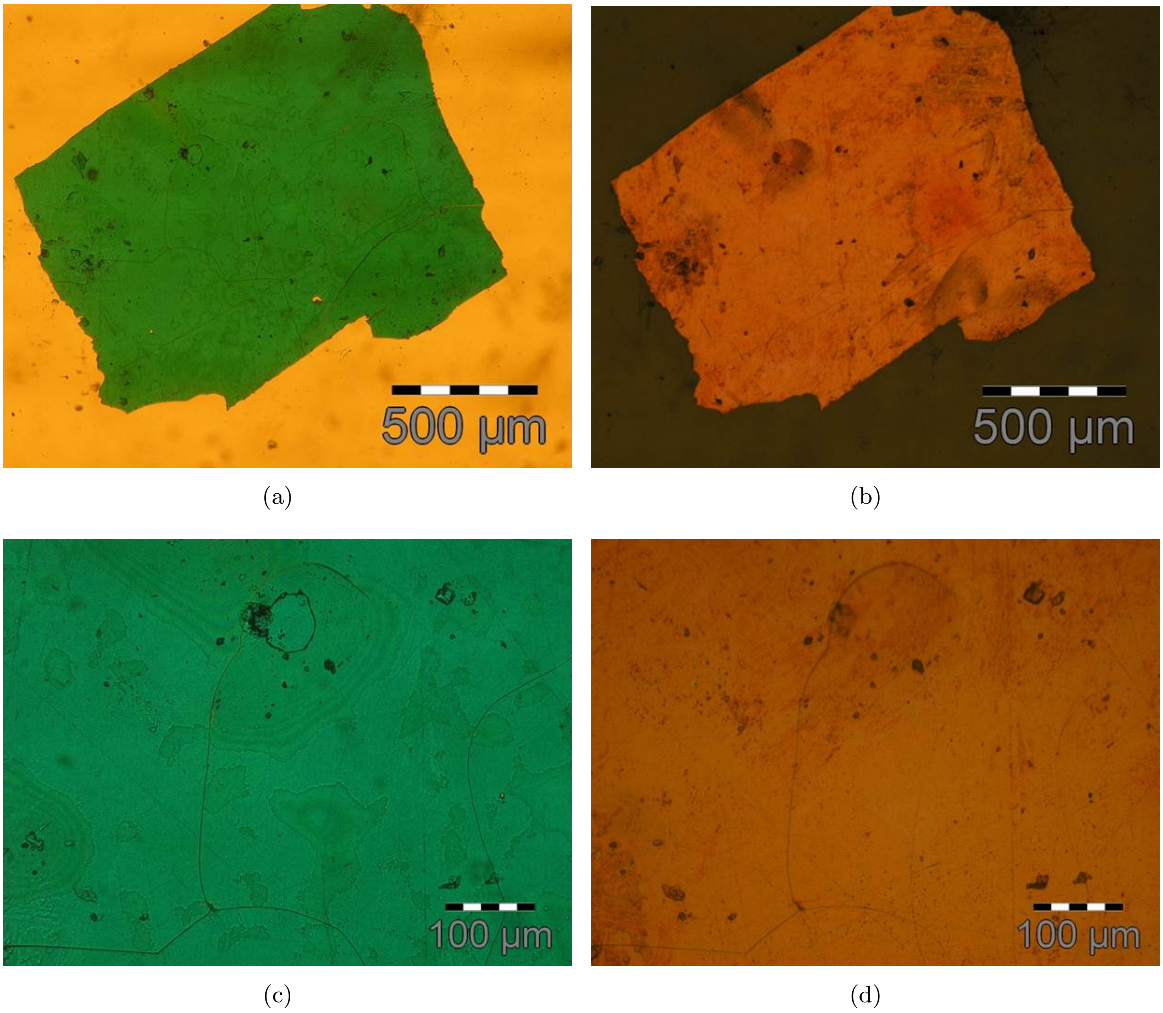

(a) (b) (c) (d)

Figure 5.18: Pictures of a DBR mirror, transfered to a glass substrate taken in an optical microscope. Pictures to the left are in transmission while the right ones are observed in reflection of white light illumination.

statement can not be made regarding the functionality of the resonators constructed through the transfer of DBRs from NaCl.

6 Conclusion and Outlook

Photophysical properties of Rubicene in solution, thin film and as single crystals were investigated to obtain a better understanding of the electronic structure in view of possible optoelectronic applications.

Upon optical excitation red emission of Rubicene was observed, where the spectral position of the radiative transitions are red-shifted from the solution to the solid form of Rubicene. The position of the maximum intensity is at 560 nm for the solution, at 680 nm for the thin film and at 630 nm for the Rubicene crystals respectively. Gaussian functions were fitted to the spectra in order to obtain the positions of all radiative transitions in Rubicene.

The quantum yield of Rubicene in solution was determined by an indirect method. Two fluorescence standards (Rhodamine 6G and Rhodamine B) were used and the measurement result for the quantum yield is $\phi_f = 0.2$.

The luminescence lifetime of Rubicene was measured in the frequency domain. For Rubicene in solution a single exponential luminescence decay was observed with $\tau = 6\,\text{ns}$. Dividing this value by the quantum yield gives the radiative decay time: $\tau_f = 30\,\text{ns}$. In contrast, Rubicene single crystals exhibit a bi-exponential decay behaviour with a short and a long lifetime on the ns-scale.

The fluorescence of Rubicene crystals under high pressure conditions was measured in a diamond anvil cell. Increasing the pressure up to 40 kbar results in a large red- shift (0.3eV) of Photoluminescence and Absorption as well as a decline of luminescence intensity. The luminescence shifts measured for Tetracene and Anthracene are of a similar order of magnitude and arise from increased intermolecular interactions as well as an increase of exciton delocalization as predicted by theoretical calculations. Similar to this calculation done for oligo-acenes the experimentally obtained red-shift of luminescence and absorption may be confirmed by a theoretical model for Rubicene.

In addition to fluorescence and absorption spectra photo-induced absorption spectra or transient absorption spectra are yet to be performed with Rubicene. Such measurements are necessary to gain further information about the decay mechanisms and excited state dynamics in Rubicene crystals or in a homogeneous polycrystalline layer. Further insights into triplet absorption and decay mechanism are important for optoelectronic applications and also the stimulated emission transitions can be identified.

We attempted to build Rubicene single crystal resonators by transferring dielectric mirrors onto the crystal's surfaces. A novel technique was used to transfer the DBR mirrors from NaCl-crystals to a glass substrate and onto the surface of an Rubicene crystal. The DBR was detached from the NaCl-crystal substrate by means of dissolving the NaCl crystal in water. Resonance within the Rubicene crystal upon optical excitation with a laser beam was observed, but no indication of the occurrence of stimulated emission was detected. The mirrors and the single crystal resonators were intensively studied, but the crystals' surface reflectivity could not be sufficiently enhanced by the DBRs which we assign to insufficient quality of the DBR surfaces after the transfer process. In addition the coherence lengths of the light sources used to study the quality of our resonators is low and could be the reason why we were not able to observe enhanced resonance characteristics with DBRs.

Direct deposition of DBRs onto the surfaces of Rubicene crystals is another possibility to build a working high-quality single crystal resonator. Already demonstrated for Tetracene crystals is the deposition of SiO_x / TiO_x systems by means of electron beam deposition [62]. In contrast to thermal evaporation techniques degradation due to high temperatures is prevented by this technique.

Apart from a plane-parallel resonator structure it is also conceivable to build a DFB cavity with Rubicene crystals. DFB lasers consist of a grating embossed on a thin film or an organic crystal, where the diffracted modes propagate along the film. The first order is emitted along the propagation direction while the second order diffraction is emitted perpendicularly to the surface. Therefore, the beam gets amplified in a higher length compared to a vertical cavity as we used in our resonator designs and high gain can be reached that comes along with a reduced laser threshold [6]. With Rubicene crystals a DFB design may be realized by imprinting a grating into a crystal's surface, where the crystal may be softed first in Toluene vapor prior to imprinting the grating.

Bibliography

[1] Robert F. Service. Outlook brightens for plastic solar cells. *Science*, 332(6027):293, 2011.

[2] Nir Tessler. Lasers based on semiconducting organic materials. *Advanced Materials*, 11(5):363–370, 1999.

[3] G. Kranzelbinder and G. Leising. Organic solid-state lasers. *Reports On Progress In Physics*, 63(5):729–762, May 2000.

[4] M. D. McGehee and A. J. Heeger. Semiconducting (conjugated) polymers as materials for solid-state lasers. *Advanced Materials*, 12(22):1655–1668, 2000.

[5] U Scherf, S Riechel, U Lemmer, and R.F Mahrt. Conjugated polymers: lasing and stimulated emission. *Current Opinion in Solid State and Materials Science*, 5:143 – 154, 2001.

[6] I. D. W. Samuel and G. A. Turnbull. Organic semiconductor lasers. *Chemical Reviews*, 107(4):1272–1295, 2007.

[7] Sebastien Chenais and Sebastien Forget. Recent advances in solid-state organic lasers. *Polymer International*, 61(3):390–406, 2012.

[8] J Hecht. Photonic frontiers: Organic semiconductor lasers- the pump is the challenge. *LaserFocusWorld*, 2008.

[9] N. Tessler, G. J. Denton, and R. H. Friend. Lasing from conjugated-polymer microcavities. *Nature*, 382(6593):695–697, August 1996.

[10] Christian Gaertner. *Organic Laser Diode.* PhD thesis, Universität Karlsruhe, 2008.

[11] R. W. I. de Boer, T. M. Klapwijk, and A. F. Morpurgo. Field-effect transistors on tetracene single crystals. *Applied Physics Letters*, 83(21):4345–4347, 2003.

[12] Hajime Sakata and Hideki Takeuchi. Diode-pumped polymeric dye lasers operating at a pump power level of 10 mw. *Applied Physics Letters*, 92(11):113310, 2008.

[13] E. Zojer, M. Knupfer, Z. Shuai, J. L. Bredas, J. Fink, and G. Leising. The quasi-band-structure description of conjugated oligomers. *Journal of Physics-condensed Matter*, 12(8):1753–1768, February 2000.

[14] D. Fichou. *Handbook of oligo- and polythiophenes.* Wiley-VCH, 1999.

[15] Jürgen Fabian and Horst Hartmann. Structure and properties of alpha cyclo[n]thiophenes as potential electronic materials - a theoretical study. *Journal of Physical Organic Chemistry*, 20(8):554–567, 2007.

[16] Landolt-Börnstein. *Numerical Data and Functional Relationships in Science and Technology, Group 3.* Springer-Verlag, 1985.

[17] D. J. NORRIS, M. NIRMAL, C. B. MURRAY, A. SACRA, and M. G. BAWENDI. Size-dependent optical spectroscopy of ii-vi semiconductor nanocrystallites (quantum dots) rid f-4022-2010. *Zeitschrift Fur Physik D-atoms Molecules and Clusters*, 26(1-4):355–357, May 1993.

[18] Rebecca C. Somers, Moungi G. Bawendi, and Daniel G. Nocera. Cdse nanocrystal based chem-/bio- sensors. *Chem. Soc. Rev.*, 36(4):579–591, 2007.

[19] Andreas Hirzer. Physics and photophysics of the organic semiconductor rubicene. Master's thesis, Tu Graz, 2010.

[20] Robert Hull, editor. *Properties of Crystalline Silicon.* INSPEC, 1999.

[21] Peter Puschnig and Claudia Ambrosch-Draxl. Excitons in organic semiconductors. *Comptes Rendus Physique*, 10(6):504–513, July 2009.

[22] M. Pope and C.E. Swenberg. *Electronic processes in organic crystals and polymers.* Monographs on the physics and chemistry of materials. Oxford University Press, 1999.

[23] E.A. Silinsh. *Organic Molecular Crystals.* Springer-Verlag, Berlin, 1980.

[24] J. R. Lakowicz. *Principles of Fluorescence Spectroscopy 3rd edition.* Springer, 2010.

[25] H. J. Eichler J. Eichler. *Laser Bauformen, Strahlführung, Anwendungen.* Springer, 2010.

[26] G. Brooker. *Modern classical optics.* Oxford University Press, 2003.

[27] G.W.F. Drake. *Atomic, Molecular, & Optical Physics Handbook, Chaps. 19 and 57.* 1996.

[28] Gerald Dicker. Photophysics of conjugated polymers and inorganic nanoparticles. Master's thesis, 1999.

[29] Glenn A. Crosby and James N. Demas. Measurement of photoluminescence quantum yields. review. *J. Phys. Chem.*, 75(8):991–1024, April 1971.

[30] Christian Wuerth, Markus Grabolle, Jutta Pauli, Monika Spieles, and Ute Resch-Genger. Comparison of methods and achievable uncertainties for the relative and absolute measurement of photoluminescence quantum yields. *Anal. Chem.*, 83(9):3431–3439, April 2011.

[31] S. Hooker and C. Webb. *Laser Physics.* Oxford master series in physics: Atomic, optical, and laser physics. Oxford University Press, 2010.

[32] G. A. Turnbull I. D. W. Samuel. Organic semiconductor lasers. *Chem. Rev.*, 2007.

[33] N. Deepak Kumar, Jayant D. Bhawalkar, Paras N. Prasad, Frank E. Karasz, and B. Hu. Solid-state tunable cavity lasing in a poly(para-phenylene vinylene) derivative alternating block co-polymer. *Applied Physics Letters*, 71(8):999–1001, 1997.

[34] M. Ichikawa, R. Hibino, M. Inoue, T. Haritani, S. Hotta, K. Araki, T. Koyama, and Y. Taniguchi. Laser oscillation in monolithic molecular single crystals. *Advanced Materials*, 17(17):2073–2077, 2005.

[35] Weijie Xie, Feng Li, Huan Wang, Zengqi Xie, Fangzhong Shen, Yuguang Ma, Wu Lu, Dingke Zhang, and Dongge Ma. Stimulated emission from distyrylbenzene derivative crystals grown by vapor deposition. *Appl. Opt.*, 46(20):4431–4433, Jul 2007.

[36] Abeles1950. Investigations on the propagation of sinusoidal electromagnetic waves in stratified media. application to thin films. *Ann. Phys.(Paris)*, 1950.

[37] S.E. Burns, G. Denton, N. Tessler, M.A. Stevens, F. Cacialli, and R.H. Friend. High finesse organic microcavities. *Optical Materials*, 9:18 – 24, 1998. Materials, Physics and Devices For Molecular Electronics and Photonics.

[38] Pompilio Del Carro, Andrea Camposeo, Luana Persano, Silvia Tavazzi, Marcello Campione, Antonio Papagni, Luisa Raimondo, Leonardo Silvestri, Peter Spearman, Roberto Cingolani, and Dario Pisignano. Monolithic vertical microcavities based on tetracene single crystals. *Applied Physics Letters*, 92(6):063301, 2008.

[39] C. Karnutsch, C. Gyrtner, V. Haug, U. Lemmer, T. Farrell, B. S. Nehls, U. Scherf, J. Wang, T. Weimann, G. Heliotis, C. Pflumm, J. C. deMello, and D. D. C. Bradley. Low threshold blue conjugated polymer lasers with first- and second-order distributed feedback. *Applied Physics Letters*, 89(20):201108, 2006.

[40] Takeshi Yamao, Takeshi Inoue, Yuki Okuda, Takashi Ishibashi, Shu Hotta, and Naoto Tsutsumi. Gain-narrowed emissions from oligomer crystals assisted by interference exposure. *Synthetic Metals*, 159:889 – 892, 2009. International Symposium on Control of Super-Hierarchical Structures and Innovative Functions of Next-Generation Conjugated Polymers, Oct 21-23 2008, Hyogo, Japan.

[41] T. Fließbach. *Statistische Physik: Lehrbuch zur Theoretischen Physik IV*. Fließbach, Torsten: Lehrbuch zur theoretischen Physik. Spektrum Akademischer Verlag, 2010.

[42] Kihyun Kim, Min Ki Kim, Han Saem Kang, Mi Yeon Cho, Jinsoo Joo, Ju Hee Kim, Kyung Hwan Kim, Chang Seop Hong, and Dong Hoon Choi. New growth method of rubrene single crystal for organic field-effect transistor. *Synthetic Metals*, 157:481 – 484, 2007.

[43] R. Hibino, M. Nagawa, S. Hotta, M. Ichikawa, T. Koyama, and Y. Taniguchi. Emission gain-narrowing from melt-recrystallized organic semiconductor. *Advanced Materials*, 14(2):119–+, January 2002.

[44] J. J. Burdett, A. M. Muller, D. Gosztola, and C. J. Bardeen. Excited state dynamics in solid and monomeric tetracene: The roles of superradiance and exciton fission. *Journal of Chemical Physics*, 133(14):44506–44506, October 2010.

[45] M. Fischer and J. Georges. Fluorescence quantum yield of rhodamine 6g in ethanol as a function of concentration using thermal lens spectrometry. *Chemical Physics Letters*, 260(1-2):115–118, September 1996.

[46] R.F. Kubin and A.N. Fletcher. Fluorescence quantum yields of some rhodamine dyes. *Journal of Luminescence*, 27(4):455–462, December 1982.

[47] T. Karstens and K. Kobs. Rhodamine b and rhodamine 101 as reference substances for fluorescence quantum yield measurements. *J. Phys. Chem.*, 84(14):1871–1872, July 1980.

[48] R. SCHMIDT. Determination of the phosphorescence quantum yield of singlet molecular-oxygen (1-delta-g) by means of a radiometer and an infrared luminescence spectrometer. *Chemical Physics Letters*, 151(4-5):369–374, October 1988.

[49] C. Burgdorff, T. Kircher, and H.-G. Löhmannsröben. Photophysical properties of tetracene derivatives in solution. *Spectrochimica Acta Part A: Molecular Spectroscopy*, 44(11):1137 – 1141, 1988.

[50] R. P. GROFF, G. P. AVAKIAN, and MERRIFIE.RE. Coexistence of exciton fission and fusion in tetracene crystals. *Physical Review B-solid State*, 1(2):815–&, 1970.

[51] A. JAYARAMAN. Diamond anvil cell and high-pressure physical investigations. *Reviews of Modern Physics*, 55(1):65–108, 1983.

[52] D. J. DUNSTAN and I. L. SPAIN. The technology of diamond anvil high-pressure cells .1. principles, design and construction. *Journal of Physics E-scientific Instruments*, 22(11):913–923, November 1989.

[53] I. L. SPAIN and D. J. DUNSTAN. The technology of diamond anvil high-pressure cells .2. operation and use. *Journal of Physics E-scientific Instruments*, 22(11):923–933, November 1989.

[54] H. K. MAO, J. XU, and P. M. BELL. Calibration of the ruby pressure gauge to 800-kbar under quasi-hydrostatic conditions. *Journal of Geophysical Research-solid Earth and Planets*, 91(B5):4673–4676, April 1986.

[55] S. Klotz, J. . C. Chervin, P. Munsch, and G. Le Marchand. Hydrostatic limits of 11 pressure transmitting media. *Journal of Physics D-applied Physics*, 42(7):075413, April 2009.

[56] Z. A. Dreger, E. Balasubramaniam, Y. M. Gupta, and A. G. Joly. High-pressure effects on the electronic structure of anthracene single crystals: Role of nonhydrostaticity. *The Journal of Physical Chemistry A*, 113(8):1489–1496, 2009.

[57] M. Oehzelt, A. Aichholzer, R. Resel, G. Heimel, E. Venuti, and R. G. Della Valle. Crystal structure of oligoacenes under high pressure. *Phys. Rev. B*, 74:104103, Sep 2006.

[58] Ken ichi Mizuno, Atsuo Matsui, and Gilbert J. Sloan. Exciton-phonon interaction in tetracene single crystals under pressure. *Chemical Physics*, 131:423 – 433, 1989.

[59] Sophocles J. Orfanidis. Electromagnetic waves and antennas. ECE Department, Rutgers University.

[60] G. Leising. Anisotropy of the optical constants of pure and metallic polyacetylene. *Phys. Rev. B*, 38:10313–10322, Nov 1988.

[61] A.F. Fercher, C.K. Hitzenberger, M. Sticker, E. Moreno-Barriuso, R. Leitgeb, W. Drexler, and H. Sattmann. A thermal light source technique for optical coherence tomography. *Optics Communications*, 185:57 – 64, 2000.

[62] Pompilio Del Carro, Andrea Camposeo, Luana Persano, Silvia Tavazzi, Marcello Campione, Antonio Papagni, Luisa Raimondo, Leonardo Silvestri, Peter Spearman, Roberto Cingolani, and Dario Pisignano. Monolithic vertical microcavities based on tetracene single crystals. *Applied Physics Letters*, 92(6):063301, February 2008.